Skyrmions and Antiskyrmions in Spin-Orbit Modified Double Exchange Models

DEEPAK SINGH KATHYAT

A thesis submitted for the partial fulfillment of
the degree of Doctor of Philosophy

Department of Physical Sciences

Indian Institute of Science Education and Research Mohali
Knowledge city, Sector 81, SAS Nagar, Manauli PO, Mohali 140306, Punjab, India.

July, 2021

Declaration

The work presented in this thesis has been carried out by me under the guidance of Dr. Sanjeev Kumar at the Indian Institute of Science Education and Research Mohali. This work has not been submitted in part or in full for a degree, a diploma, or a fellowship to any other university or institute. Whenever contributions of others are involved, every effort is made to indicate this clearly, with due acknowledgement of collaborative research and discussions. This thesis is a bona fide record of original work done by me and all sources listed within have been detailed in the bibliography.

Deepak Singh Kathyat

(PH13003)

In my capacity as the supervisor of the candidate's thesis work, I certify that the above statements by the candidate are true to the best of my knowledge.

Dr. Sanjeev Kumar

(Supervisor)

Acknowledgements

First of all, I wish to show my deepest gratitude to my thesis supervisor Dr Sanjeev Kumar. His steadfast encouragement, especially the way he pulled me out through tough times is inexpressible. The work ethic I learned from him will remain to be the most valuable lesson throughout my life.

I am also thankful to my doctoral committee members Dr Abhishek Chaudhuri and Dr Yogesh Singh, for providing their time for the valuable discussions. I thank all the other faculty members, computing staff members, administrative staff members and rest of the IISER Mohali community for providing helping hands in the direct or indirect way during the period of my PhD.

I specially thank Dr Rajyavardhan Ray who helped alot and had valuable discussions with me during initial years of my PhD.

I feel privileged to be part of a very supportive research group which includes: Kanika Pasrija, Swagatam Nayak, Arnob Mukherjee, Ayushi Singhania and Abhinay Vardhan.

I like to mention my friends from whom I got precious assistance: Shubhendu Shekhar Khali, Jaskaran Singh, Mayank Srivastava, Ashiwini Balodhi, Rakesh Sharma, Sandeep Rana, Sudhanshu Shekhar Chaurasia, Ankit Singh, Avinash Singh, Anirban Ghosh, Ramu Kumar Yadav, Rajneesh Perhate, Satyam Srivastava, Priyanka Madhu, Aman Suhag and Gokul Upadhyay.

I would like to acknowledge some of my old friends: Shailesh Dhasmana, Karunava Sil, Amandeep Singh, Gagandeep Singh, Prasanta Kumbhakar, Avijit Dewasi, Gavendra Pandey, Mayank Saxena.

"Some people deserve more than just a Thank you". This sentence seems to be true when it comes to writing a 'Thank you note' in favour of the family members. Still, I thank my parents.

"कर्मणये वाधिकारस्ते मां फलेषु कदाचन ।
मां कर्मफलहेतुर्भू: मांते संङगोस्त्वकर्मणि" ।।

"karmany evadhikaras te
ma phalesu kadachana
ma karma-phala-hetur bhur
ma te sango 'stv akarmani"

"श्री कृष्ण भगवान ने अर्जुन से कहा: आप को अपने निर्धारित कर्तव्य का पालन करने का अधिकार है, लेकिन आप कभी कर्म फल की इच्छा से कर्म मत करो (कर्म फल देने का अधिकार सिर्फ ईश्वर को है)। कर्म फल की अपेक्षा से आप कभी कर्म मत करें, न ही आप की कभी कर्म न करने में प्रवृर्ति हो (आप की हमेशा कर्म करने में प्रवृर्ति हो) ।।"

"Sri Krishna said to Arjuna: You have a right to perform your prescribed duty, but you are not entitled to the fruits of action. Never consider yourself the cause of the results of your activities, and never be attached to not doing your duty."

(Bhagwat Gita: Chapter Two verse 47)

Contents

Abstract **3**

List of Publications **5**

1 Introduction **7**
1.1 Electronics and limitations . . . 8
1.2 Spintronics . . . 8
1.2.1 Magnetic Skyrmions and Antiskyrmions . . . 10
1.3 Existing Theories for Skyrmions formation . . . 12
1.4 Spin-Orbit Interaction . . . 15
1.4.1 Dresselhaus spin orbit coupling . . . 16
1.4.2 Rashba spin orbit coupling . . . 16
1.5 Kondo Lattice Model . . . 17
1.5.1 Double Exchange Mechanism . . . 20
1.6 Overview of Thesis . . . 21
Bibliography . . . 23

2 Model and Methods **29**
2.1 Introduction - Kondo Lattice Model . . . 30
2.2 Rashba Dresselhaus Spin Orbit Coupling . . . 31
2.3 Rashba Dresselhaus Kondo Lattice Model . . . 33
2.3.1 Tight Binding Term . . . 34
2.3.2 Rashba SOC Term . . . 35
2.3.3 Dresselhaus SOC Term . . . 37
2.3.4 Kondo Term . . . 38
2.4 Rashba Dresselhaus Double Exchange Model . . . 40
2.5 Effective Spin Model . . . 42
2.6 Kubo-Greenwood Formalism . . . 44
2.6.1 Current density operators . . . 45
2.7 Methods . . . 47
2.7.1 Classical Monte Carlo . . . 48
2.7.2 Steps to implement Metropolis Algorithm . . . 50
2.7.3 Hybrid Monte Carlo . . . 51
2.7.4 Bott Index . . . 52

3 Study of microscopic magnetic Hamiltonian for exotic spin textures in metals **57**
3.1 Introduction . . . 58
3.2 Derivation of the spin Hamiltonian . . . 59
3.3 Comparison with the exact electronic model . . . 61
3.4 Distribution of coupling constants . . . 62
3.5 Magnetic phases of the new spin Hamiltonian . . . 64
3.6 Finite size effects . . . 70
3.7 Conclusion . . . 72

4 Electronic mechanism for nanoscale skyrmions and topological metals **77**
4.1 Introduction . . . 78
4.2 Skyrmions in the RDE model . . . 79
4.3 Origin and stability of sparse and packed skyrmions . . . 82
4.4 Bott index and topological metalicity . . . 89
4.5 Emergent gauge fields and Landau levels . . . 93
4.6 Importance of consistent treatment . . . 95
4.7 Conclusion . . . 96

5 Antiskyrmions and Bloch skyrmions in Dresselhaus double exchange metals **103**
5.1 Introduction . . . 104
5.2 Spin-fermion model and hybrid Monte Carlo results . . . 105
5.3 Origin and stability of sparse and packed antiskyrmions . . . 108
5.4 Thermal stability of antiskyrmions . . . 112
5.5 Origin and stability of Bloch skyrmions . . . 113
5.6 Conclusion . . . 114
Bibliography . . . 117

6 Summary and Outlook **119**

Abstract

It has been understood that the conventional electronics based devices will not be able to meet the ever increasing requirements for data storage and processing of the modern world. Among others, the idea of utilizing the spin degree of freedom associated with electrons has been considered as a potential alternative. This has given rise to a new research field, popularly known as spintronics, wherein electron's spin is used as the carrier of information for device functionalities. While it is not easy to detect and utilize spin of a single electron in materials containing a large number of them, certain magnetic configurations show a desired stability and possible control via external electric or magnetic field. Therefore, search for magnetic materials supporting certain stable magnetic textures has become a key theme of research in recent years. Topologically protected magnetic textures, such as skyrmions and antiskyrmions, are of special importance due to their stability. Such textures have been discovered in chiral magnets and in thin films of a variety of magnetic metals.

The fundamental physics associated with formation of magnetic skyrmions has fascinated researchers since the discovery of these topological textures. The current approach to understand these intriguing textures is via spin models consisting of Dzyaloshinskii-Moriya (DM) interactions or frustrating long range interactions. In this thesis, we present a microscopic mechanism for skyrmion and antiskyrmion formation in metals that emerges from electronic itinerancy. We derive and study a microscopic spin Hamiltonian on a lattice for double exchange metals modified by the Rashba and Dresselhaus spin-orbit coupling (SOC). In our model, anisotropic interactions of the Dzyaloshinskii-Moriya (DM) and pseudo dipolar form emerge naturally in addition to the standard isotropic term. We present phase diagram of the effective spin Hamiltonian which has very interesting ground states like classical spin liquid state using large scale Monte Carlo simulations. We show that in the presence of Zeeman field the mechanism we propose not only provides an accurate microscopic understanding of the existence of skyrmions, but also explains key features in small angle neutron scattering (SANS) and Lorentz transmission electron microscopy (LTEM) data on thin films of MnSi-type B20 metals and transition metals and their alloys. We identify hexagonal and square lattice arrangements of skyrmions in two different regimes of the parameter space. Sparse skyrmions emerge at finite temperatures as excitations of the ferromagnetic phase. Further, the skyrmion states are characterized as topological metals via explicit calculations of Bott index and Hall conductivity. Local density of states (LDOS)

display characteristic oscillations arising from a combination of confinement effect and gauge-field induced Landau level physics. These unique features serve as testable predictions for the presence of the new mechanism of skyrmion formation in real materials. The discovery of a new mechanism based on two celebrated physics concepts not only fills a major conceptual void in the current understanding of skyrmions and antiskyrmions in metals, but also opens a new route for tuning the size, density and stability of skyrmions in magnetic metals. We also emphasize the importance of a consistent treatment of spin-orbit coupling for calculating electronic properties of metals hosting unconventional magnetic textures such as skyrmions.

Finally, we provide a clear understanding of how Neel-type skyrmions, Bloch-type skyrmions and the corresponding antiskyrmions are related with one another within a simple lattice model. We also emphasize the role played by electron itineracy in deciding the type of skyrmion textures in a metal. These features are completely missed in a spin-only model written without reference to a starting microscopic model.

List of Publications

The thesis is based on the following works:

1. **D. S. Kathyat**, A. Mukherjee, and S. Kumar, "Microscopic magnetic Hamiltonian for exotic spin textures in metals", PHYSICAL REVIEW B **102**, 075106 (2020). *(*Chapter-3)
2. **D. S. Kathyat**, A. Mukherjee, and S. Kumar, "Electronic mechanism for nanoscale skyrmions and topological metals", PHYSICAL REVIEW B **103**, 035111 (2021). *(*Chapter-4)
3. **D. S. Kathyat**, A. Mukherjee, and S. Kumar, "Antiskyrmions and Bloch Skyrmions in Magnetic Dresselhaus Metals" (***arXiv:2107.03820, Manuscript submitted***) . *(*Chapter-5)

Other works:

4. A. Mukherjee, **D. S. Kathyat**, and S. Kumar, "Antiferromagnetic skyrmions and skyrmion density wave in Rashba Hund's insulator", PHYSICAL REVIEW B **103**, 134424 (2021).
5. A. Mukherjee, **D. S. Kathyat**, and S. Kumar, "Antiferromagnetic skyrmions in Rashba Hund's insulators on triangular lattice", SCIENTIFIC REPORTS **11**, 9566 (2021).
6. A. Gupta, **D. S. Kathyat**, A. Mukherjee, A. Kumari, Y. Singh, S. Kumar and S. Chakraverty, "Unique Signatures of Rashba Effect in Angle Resolved Magnetoresistance" (***Manuscript Submitted***).
7. A. Mukherjee, **D. S. Kathyat**, and S. Kumar, "Tuning Skyrmions and Antiskyrmions from Ferromagnetic to Antiferromagnetic" (***Manuscript under preparation***).

1

Introduction

A brief introduction to spintronics and importance of unusual spin textures such as skyrmions is presented in this chapter. Interesting aspects and problems related to the magnetism in metallic systems are discussed. Important concepts like spin-orbit interactions and Kondo lattice model, which set up the background before we get into the next few chapters of thesis are discussed in detail. Finally an overview of the thesis is provided.

1.1 Electronics and limitations

Information and communication devices such as computers, smart phones, storage units, etc. have become an essential part of day-to-day life today. The commonly used electronic devices consist of two main parts: semiconductor integrated circuits (e.g., microprocessor and random-access memory) and permanent magnetic data storage devices (hard disk and memory card). The semiconductor integrated circuits (IC) are fabricated using hundreds of millions of electronic components such as resistors, diodes, transistors, and capacitors arranged together in a single chip[1]. All these electronic components make use of the fundamental degree of freedom - the electronic charge. Modern data storage devices, on the other hand, rely on the use of magnetic materials[2]. In microprocessors and random access memories, the information is processed and temporarily stored based on the electric charge of electron using classical bits[3]. The low voltage represents the 0, while the high voltage represents the 1. Increasing the number of transistor-capacitor (memory cell) in the chip will increase the number of bits and consequently its efficiency and capacity. In 1965, Gordon E. Moore stated that the numbers of the transistors in the integrated circuit will double nearly every 2 years. In 2019, the actual size of the transistor placed in commercial microprocessor is about 50 nm with gate length of 20 nm and node of 7 nm[4]. But with the continuous reduction in transistor size, the dimension of the transistor will reach to the atomic size. At this size, both the writing and reading processes will become extremely challenging due to quantum size effect and heat dissipation[5–8]. As a result the progress in the electronic devices will come to the end when the transistor node size reaches to 1 nm. Random access memory (RAM) used in conventional electronics lose information when power (electricity) is cutoff[4]. Also, the capacitors in conventional electronics consume more energy due to charge leakage[4]. To overcome these limitations scientists are working on a promising alternative technology called spintronics.

1.2 Spintronics

Spintronics is an emerging field of research with a potential to revolutionalize data storage and processing technologies. The key idea is to utilize electron's spin, in addition to or instead of its charge, as the carrier of information for device functionalities[9–12]. Spintronics has become an emerging field of condensed matter physics not only because of its potential in developing future technologies but also because one can explore and answer the very fundamental questions on physics of electron spin. Utilizing electron spin in the quantum transport phenomena provides many important implications. The

first spintronic device concept known as spin field effect transistor was originally proposed by Datta-Das in 1990[13]. Since then condensed matter physicists are working on understanding the fundamental physics and novel mechanisms that can be utilized in developing these devices.

Albert Fert and Peter Grunberg were awarded the 2007 Nobel Prize in Physics for the discovery of giant magnetoresistance (GMR)[14–16]. The read heads of magnetic hard drives which is based on this phenomenon is the first commercial application of spintronics technology in computers. 0 bit (spin up) and 1 bit (spin down) are the two magnetic states used in the hard disk drive to store data by encoding them magnetically on circular rotating platters. To write or read these data, disk heads are used.[4]. In the case of reading the disk, the disk heads transform magnetic field stored on platters to electrical current, while the writing process is performed by converting the electrical current into magnetic field. GMR system consists of two magnetic layers separated by a non-magnetic one. GMR as a disk head exhibited a large change in resistance nearly reaching 20% when exposed to a magnetic field change spin. In GMR, the parallel orientation of the two magnetic layers is characterized by an electrical state of low resistance, while the antiparallel orientation in the two magnetic layers is a state of high resistance. The huge changes in resistance of this device can be used to sense the magnetic storage data in the hard drive platters with high efficiency. The success of the giant magnetoresistance encourages the scientists to work on replacing the semiconductor components such as random access memory, microprocessor, and transistors by magnetic random access memory, magnetic microprocessor, and spin-transistor in computer device. Unlike semiconductor random access memory, computer with a magnetic random access memory as spintronics device would always retain its information even when power is suddenly cutoff[17]. Also less energy is needed to switch the spin states from 0 to 1 or vice versa, so spintronics devices use less power. The magnetic random access memory technology still needs improvement, but the work is continuous to fabricate it perfectly. Thus spintronics combines the semiconductor properties based on charge (integrated circuits) and the magnetic properties based on spin (storage hard drive) in a single chip to perform all process in one device. We can conclude that the transfer from conventional electronics to spintronics technology opens the possibilities to construct devices with high storage density, low power consumption, and fast operation and that are cheap and robust.

It is well known that interactions in many particle systems can give rise to emergent quasiparticles whose dynamics can be very different from that of constituent particles. This holds true for magnetic systems as well. New particle-like textures in magnetization can become stable. Such textures may prove very useful in both, insulators and met-

als, for technological applications. Therefore, search for magnetic materials supporting unusual magnetic textures has been a key theme of research in recent years[18? –25]. Presence of such spin textures in metals allows for their control using low currents[26–32]. Furthermore, nontrivial magnetic states in metals are known to dramatically influence the charge transport, which can be utilized in spintronic devices.

Topologically protected magnetic textures, such as skyrmions, are of special importance due to their stability[33]. Skyrmion-based devices have the potential to store and process information in unprecedentedly small spaces. The presence or absence of a skyrmion could serve as a 1 or 0 in a data bit for racetrack memory, and multiple skyrmions could aggregate to form storage devices. Smaller the skyrmions we have, denser is the packing of information. The states of such devices could be modulated by an electric current that drives skyrmions in and out of the devices. The flexibility to design the host and tune the skyrmion properties offers versatility for technological applications[33–39] has motivated the discovery of skyrmions in variety of materials icluding B20 Ferromagnet, Ferromagnetic thin film, Magnetic Multilayer, Multiferroics, van der Waals ferromagnet/heterostructure, SAF-antiferromagnet etc. in recent years[40–53]. Some of them are listed in Table 1.

1.2.1 Magnetic Skyrmions and Antiskyrmions

Magnetic skyrmions, are whirling cylinders of magnetization. Although the term skyrmion was introduced in nuclear physics, the term has spread, and now it describes various physical phenomena in condensed matter, string theory and particle and nuclear physics[54].

Topologically, a magnetic skyrmion is described by an integer, known as topological charge, which is given by:

$$Q = \frac{1}{4\pi} \int d^2 r (\partial_x \mathbf{m} \times \partial_y \mathbf{m}) \cdot \mathbf{m} \tag{1.1}$$

where, $\mathbf{m}$ is a unit vector pointing in the direction of the magnetization. The topological charge describes how many times magnetic moments wrap around a unit sphere upon application of stereographic projection (see Fig. 1.1). Erasing a skyrmion requires globally modifying the system and, as a result, skyrmions possess topological protection.

Table 1: Materials and Thin-Film Heterostructures Hosting Topological Spin Textures				
material	content	transition temperature(K)	spin texture	conductivity
MnSi		30	Bloch Sk	metal
$Fe_{1-x}Co_xSi$	$(0.05 \leq x \leq 0.7)$	2-50	Bloch Sk	semiconductor
FeGe		280	Bloch Sk	metal
$MnSi_{1-x}Ge_x$	$(0 \leq x \leq 0.25)$	30	Bloch Sk	metal
$Co_{10-x/2}Zn_{10-x/2}Mn_x$	$(0 \leq x \leq 6)$	148-462	Bloch Sk	metal
	$x = 6$	160	Bloch Sk	metal
$Co_8Zn_9Mn_3$		325	Bloch Sk meron lattice	metal
$Co_{8-x}Fe_xZn_8Mn_4$	$(0 \leq x \leq 4.5)$	130-300	Bloch Sk	metal
$FeCo_{0.5}Rh_{0.5}Mo_3N$		120	Bloch Sk	metal
EuPtSi		4	Bloch Sk	metal
Cu_2OSeO_3		59	Bloch Sk	insulator
$Mn_{1.4}Pt_{0.9}Pd_{0.1}Sn$		400	anti-Sk	metal
GaV_4S_8		13	Neel Sk	insulator
GaV_4Se_8		17.5	Neel Sk	insulator
$VOSe_2O_5$		7.5	Neel Sk	insulator
Fe/Ir(111)		11	Neel Sk	metal
PdFe/Ir(111)		4.2	Neel Sk	metal
$(Ir/Co/Pt)_{10}$		> 300	Neel Sk	metal
$SrIrO_3/SrRuO_3$		120	Neel Sk	metal
$BaTiO_3/SrRuO_3$		80	Neel Sk	metal
Gd_2PdSi_3		20	Bloch Sk	metal
$Gd_3Ru_4Al_{12}$		19	Bloch Sk	metal

Table 1 Materials and Thin-Film Heterostructures Hosting Topological Spin Textures. The table is adapted from review article[55].

Magnetic skyrmions that were discovered in chiral $B20$ compounds such as MnSi, FeGe are reffered as Bloch- and Neel-type skyrmions. Helicity and polarity are also used to describe skyrmions. Helicity can be defined as the angle of the global rotation around the z-axis that relates various skyrmions to the Neel skyrmion. For the Neel skyrmion, helicity is zero. Polarity describes whether the magnetization points in the positive ($p = 1$) or negative ($p = -1$) z-direction at the center of the skyrmion. For Bloch and Neel skyrmions, the topological charge and polarity are equal ($Q = p$). The difference in helicity distinguishes Bloch and Neel skyrmions from one another. Some magnetic skyrmions can also have opposite topological charge and polarity ($Q = -p$). Such mag-

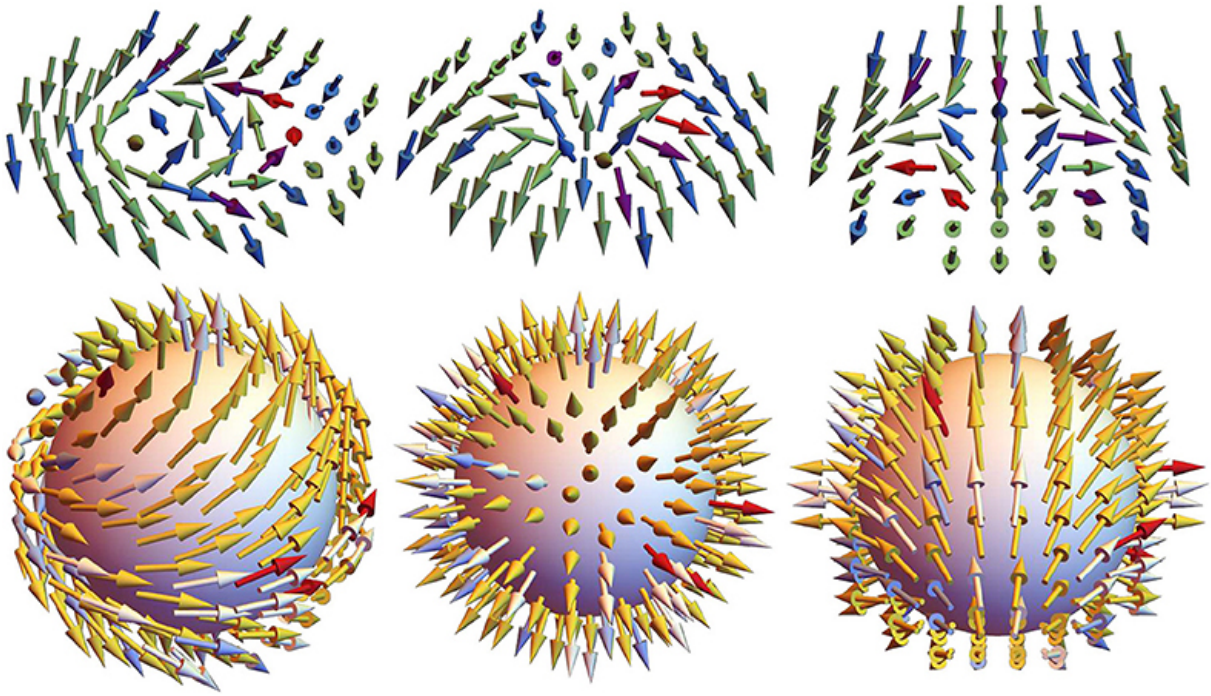

Figure 1.1 (Top and bottom) Bloch (left), Neel (middle) skyrmions and Antiskyrmion (right).

netic textures are known as antiskyrmions. Fig. 1.2 shows some of the skyrmions and antiskyrmions with their respective topological charge and helicity (γ).

1.3 Existing Theories for Skyrmions formation

The key step towards designing or discovering materials with unconventional spin textures is to understand the physics of minimal microscopic models incorporating essential elementary mechanisms[56–58]. The current microscopic understanding of these intriguing magnetic textures in insulators relies on spin models[57,59–62]. Microscopic mechanisms to twist neighbouring spin-moment directions are necessary for the formation of skyrmions and various noncolliner spin textures. Such twisting mechanisms is mainly rooted in the antisymmetric exchange interaction due to spin orbit coupling i.e., Dzyaloshinskii Moriya (DM) interaction, which is present in magnets with noncentrosymmetric crystal lattice structures. Skyrmions have appeared in polar noncentrosymmetric ferromagnet, GaV_4S_8 and in nanolayers with engineered Dzyaloshinskii Moriya interactions. Spin Hamiltonians naturally emerge in insulators as the charge degrees of freedom become inactive and the low energy physics is determined by the spin degrees of freedom. So understanding based on spin only models for insulators is correct. But these models should not be extended for the explanation of emergence of exotic spin textures in metallic systems as the inineracy of electrons is the crucial

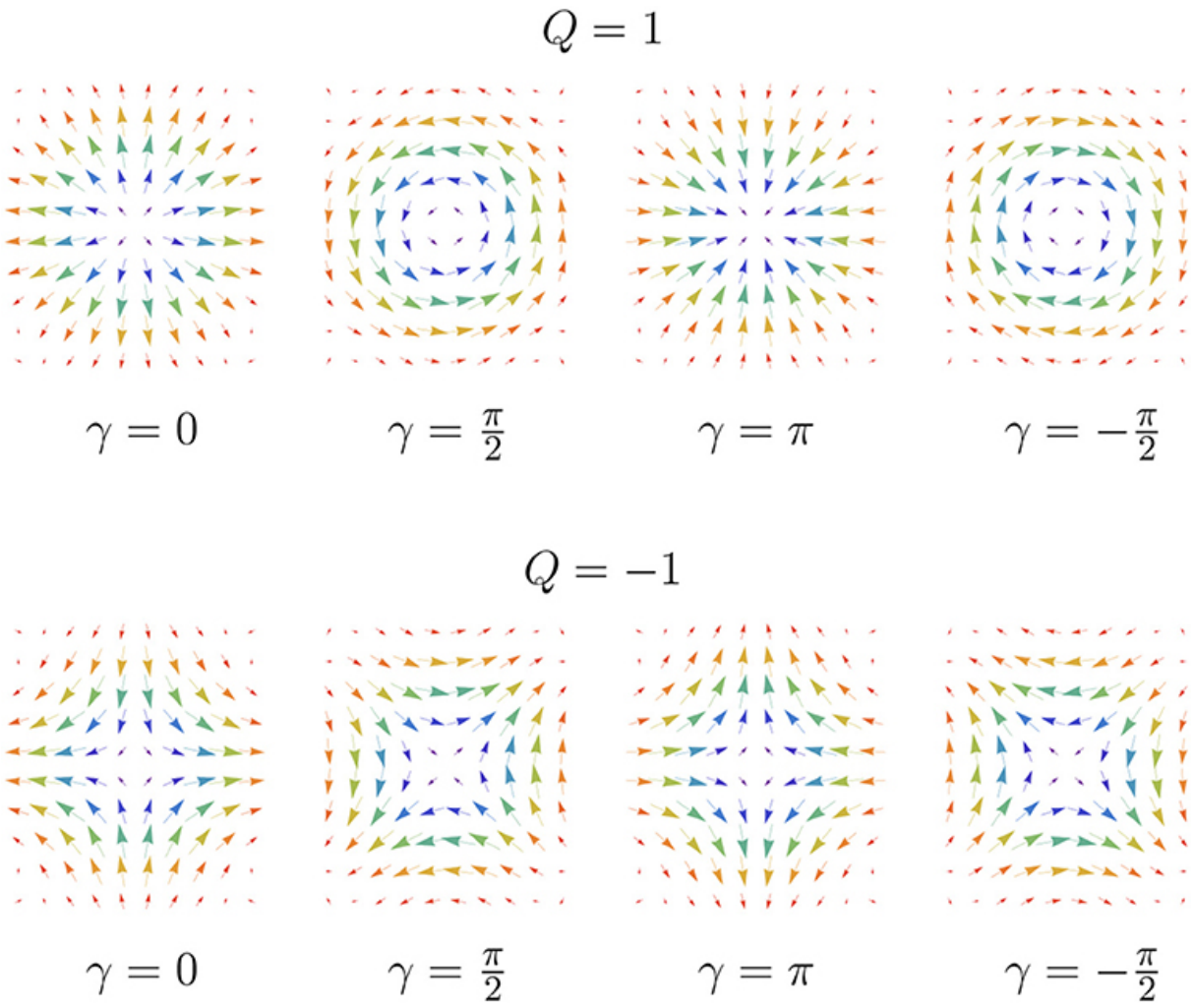

Figure 1.2 Magnetization configuration of skyrmions ($Q = 1$) and antiskyrmions ($Q = -1$) with fixed polarity ($p = 1$) and varying helicity. The length and direction of the arrows represent the in-plane component of **m**, and the color indicates m_z.

---

fecture of those systems that can not be ignored.

As far as metals are concerned skyrmions have discovered in many chiral cubic helimagnet metals including FeGe, MnSi etc. A simplified model for the energy w_0 of a chiral cubic ferromagnet in an applied magnetic field H is

$$w_0(\mathbf{M}) = A(\nabla \cdot \mathbf{M})^2 - \mathbf{M} \cdot \mathbf{H} - D(\mathbf{M} \cdot \nabla \times \mathbf{M}) \tag{1.2}$$

The equation has three energy components, which contribute to the formation of magnetic skyrmions. The first ferromagnetic exchange energy term, with constant A, imposes parallel ordering of the magnetic moments. The second term, which is the interaction with the applied magnetic field, favors magnetization oriented along H. The final Dzyaloshinskii Moriya term induces helical modulations. The model introduces two fundamental parameters: the helix period $L_D = 4\pi A/|D|$ and the saturation field

$H_D = D^2M/(2A)$ that suppresses chiral modulations. At high magnetic fields, minimizing the energy functional $w(\mathbf{M})$ yields isolated skyrmions in the form of weakly repulsive localized states in an otherwise uniformly magnetized state. They arise from a subtle balance of the competing magnetic forces. The antiparallel magnetization at the skyrmion center is energetically unfavorable in the presence of an applied magnetic field, so the skyrmion core gradually shrinks with increasing magnetic field.

On the other hand, long-ranged exchange interactions mediated by itinerant electrons, as represented by Ruderman-Kittel-Kasuya-Yosida (RKKY) interaction leads to magnetic frustration or higher order interactions, resulting in formation of various kinds of noncollinear spin textures such as spin spirals[63–66]. Formation of multiple-q state is further assisted by geometrical frustration such as in triangular or kagome lattices or by the higher-order terms of the long-range interactions among multi sites and multi spin components. As the modulation period is comparable to the length scale of magnetic interactions in this case, the skyrmion size can be consequently as small as a few nanometers. Such interactions result in the topological spin crystals such as in the Fe/Ir interface, MnGe, Gd-based compounds and $SrFeO_3$. The long-range exchange interactions enables the skyrmion formation in the centrosymmetric materials with the absence of DM interaction.

Studies so far on the skyrmions formation and transport in the metals that consist of a subsystem of localized magnetic moments interacting with conduction band are highly inadequate. People have studied these systems using the spin Hamiltonians which include DM interations of the form $\mathbf{D} \cdot \mathbf{S}_i \times \mathbf{S}_j$ between localized spins with direct interactions and easy axis anisotropic terms. And for the transport properties they just have studied the effect of the magnetic ground states on charge carriers[60,62,67]. So, the basic questions that motivates us to look beyond the phenomelogical models and is central theme of this thesis is what happens when the itenerancy of charge carriers is included in the Model?

• *What are the magnetic groundstates induced by the strong correlation of localized spins with charge carriers?*

• *How is the charge transport affected by the magnetic order?*

In next three sections we provide the details some of the important concepts that are foundation of the theoretical work that we are presenting in the thesis.

1.4 Spin-Orbit Interaction

Spin-orbit coupling is a relativistic effect. The electron moving even in the absence of externally applied magnetic field experiences a magnetic field in its rest frame that arise from the Lorentz transformation of the static (external) electric field. This relativistically generated magnetic field, known as spin orbit (SO) field, couples to the electron's magnetic moment[68].

SO coupling in atoms

In atoms, the orbital motion of an electron in the centrally symmetric electric field of an atomic nucleus gives rise to SO coupling effect and lift the degeneracy of the one electron energy level with opposite spins. The SO coupling increases with the atomic number Z of the atom as Z^4. Only this SO coupling is the reason for the Hund's third rule which states that " given Hund's first and second rules, depending on whether the shell of orbitals is more than half filled (+) or less than half filled (-), the orbital and spin angular momentum either align or antialign respectively, so that the total angular momentum is $J = |L \pm S|$ ".

SO coupling in solids

SO coupling can be present in solids in externally applied electric field. It arises from an interaction of the electron spin with the magnetic field that is experienced by the moving electrons in their frame of motion. Suppose an electron moves with velocity $\mathbf{v}$ in an electric field $\mathbf{E}$. Performing Lorentz transformation to its rest frame, the electron experiences a magnetic field,

$$\mathbf{B} = -\frac{1}{c^2}(\mathbf{v} \times \mathbf{E}). \tag{1.3}$$

The magnetic moment of the electron can interact with this field, giving rise to a Zeeman-like term

$$H_{SO} = -\frac{1}{2} g^* \mu_B \mathbf{B} \cdot \sigma. \tag{1.4}$$

Substituting Eq.(1.3) in Eq.(1.4) and using $\mathbf{v} = \mathbf{P}/m^*$ we finally get,

$$H_{SO} = \frac{g^* e\hbar}{4m^{*2}c^2}(\mathbf{P} \times \mathbf{E}) \cdot \sigma \tag{1.5}$$

where, $\lambda = \frac{g^* e\hbar}{4m^{*2}c^2}$ is a material constant describing the strength of coupling.

Existence of internal electric fields is prohibitted in inversion symmetric crystals. SO coupling is present only in crystals which lack the inversion symmetry. Depending on

the origin of assymetry they can be further classify into two types:

1.4.1 Dresselhaus spin orbit coupling

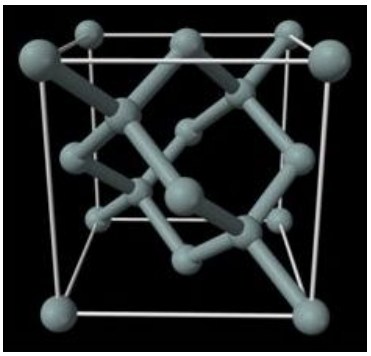

Figure 1.3 Crystal structure with bulk inversion asymmetry.

SOC known as Dresselhaus SOC ocuurs in the crystal structures which lack a center of inversion such as the GaAs or InSb. This inversion asymmetry is known as Bulk inversion asymmetry, beacause of which there occurs a net electric field in certain crystal directions.

The Mathematical form of the Hamiltonian corresponding to the Dresselhaus SOC in 3D is given by[69],

$$H_{DSO}^{3D} = \gamma((P_y^2 - P_z^2)P_x\sigma^x + (P_z^2 - P_x^2)P_y\sigma^y + (P_x^2 - P_y^2)P_z\sigma^z) \tag{1.6}$$

When we make a layer or a thin film of such materials so that the electrons are confined in two dimension, the cubic Dresselhaus SO coupling Eq.(1.6) reduces to the linear Dresselhaus SO coupling,

$$H_{DSO}^{2D} = \beta(P_x\sigma^x - P_y\sigma^y) \tag{1.7}$$

1.4.2 Rashba spin orbit coupling

Experimentally, when a two dimensional electron gas is created at the interface; the structural inversion symmetry breaks along the growth direction. This is done by confining electrons by an approximate triangular potential well V(z)(see Fig. 1.4). If this well is narrow enough electrons will only occupy the lowest eigenstate (bound states) and the movement along the z direction is effectively frozen out so that electrons are only free to move in a two-dimensional plane.

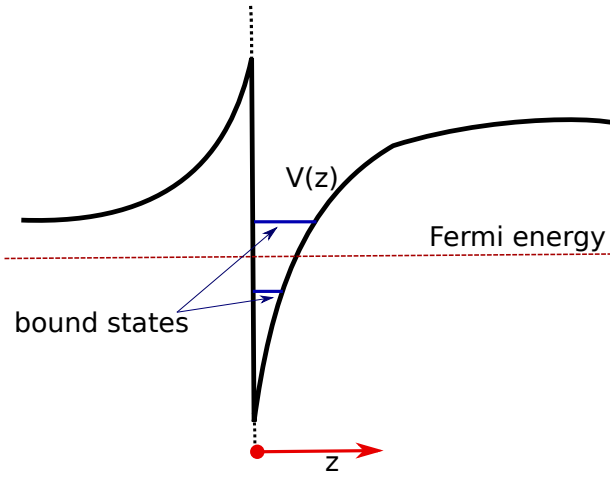

Figure 1.4 An approximate triangular potential well V(z) confining the conduction electrons at the interface (x-y plane).

The assymetry of this potential well not only confines the electrons in a plane but also give rise to so called Rashba spin orbit coupling because of the nonzero potential gradient[69]. From Eq.(1.5) we get,

$$H_{RSO} = \lambda \frac{dV}{dz} \mathbf{P} \cdot (\hat{z} \times \sigma) \tag{1.8}$$

For non uniform dV/dz, $\alpha = \lambda \langle dV/dz \rangle$ is called Rashba parameter which will be non zero only for the assymetric confining potential well. Important point to be noted here is that the strength of the Rashba parameter is directly proportional to the potential drop at the interface. So it can be controlled by an external gate voltage across a heterojucntion containing two-dimensional electron gas. Applying gate voltage modifies the shape of confining potential well and electron occupation, and thus the strength of Rashba parameter. This control on Rashba parameter has lead to proposals for a variety of devices based upon controlling the spin degrees of freedom electrically (rather than with magnetic fields).

Eq.(1.8) can also be written as,

$$H_{RSO} = \alpha(P_y \sigma^x - P_x \sigma^y) \tag{1.9}$$

1.5 Kondo Lattice Model

The Kondo lattice describes the materials in which the interactions are dominated between two distinct varieties of electrons; localized electrons possessed of a magnetic moment, and itinerant electrons[70].

This situation is realised in, at least, the following two classes of materials:

(i) Manganese oxide perovskites, in which there exist a ferromagnetic exchange interaction because of the mixed valency of magnetic ion.

(ii) Rare earth and actinide compounds, also known as heavy fermion materials, in which the f orbitals remain strongly localized and interact with electrons in the conducting d (or hybridized s-d) band.

The model was originaly proposed to explain the effect known as Kondo effect. In 1934 it was observed that for metals like silver, gold doped with impurities like Fe, Mn, the resistivity ρ at low temperature increases with decreasing temperature (T) instead of decreasing as expected from normal metals according to the Landau theory of Fermi liquids as

$$\rho(T) \quad = \quad \rho_o + a\mathrm{T}^2 + b\mathrm{T}^5, \tag{1.10}$$

where, a and b are constants, ρ_o is the residual resistivity due to defects and impurities, T^2 dependence comes from electron-electron scattering whereas T^5 dependence comes from electron-phonon scattering.

In metals with magnetic impurities, the magnetic moments behave like free moments at high temperatures but below a characteristic temperature, known as the Kondo temperature T_K, the conduction electrons begin to form a cloud of opposite spin-polarization around the impurity spin via singlet formation with the localized spin which leads to the impurity spin becoming non-magnetic. This process of magnetic screening of a magnetic impurity by the conduction electrons is known as the Kondo effect. This effect results in a new term in the resistivity which is proportional to -$J_K \ln \mathrm{T}$ where J_K is the exchange coupling between the local moment and the conduction electrons. As $\mathrm{T} \to 0$ for antiferromagnetic interaction ($J_K > 0$), $\rho \propto -\ln \mathrm{T}$ diverges. This leads to the appearance of a resistivity minimum, below which the resistivity increases with decreasing temperature.

The Hamiltonian for Kondo Lattice Model is given by,

$$H \quad = \quad -t \sum_{\langle ij \rangle, \sigma} (c^{\dagger}_{i\sigma} c_{j\sigma} + H.c) + J_K \sum_i \mathbf{S}_i \cdot \mathbf{s}_i. \tag{1.11}$$

which includes hoppings between nearest neighbor sites, coupling between localized spins and itenerant electron spin at each site. J_K denote the strength of Kondo coupling. $\mathbf{s}_i$ is the spin operator for an electron at site i, and $\mathbf{S}_i$ denotes the localized spin at

that site. We will focus more on the regime with ferromagnetic coupling ($J_K < 0$), also called ferromagnetic Kondo lattice model. This arises from an on-site Hund's rule coupling between the localized electron spin and the spin of the the conduction electrons in Hund's metals. Since the localized spins are usually very large ($S = 3/2, 5/2, 7/2$) in Hund's metals; we approximate $\mathbf{S}_i$ as a classical vector with $|\mathbf{S}_i| = 1$. Even with this approximation the model gives results that are in very good agreement with experiments.

Kondo Lattice Model belongs to a class of Hamiltonians with non-interacting electrons coupled to classical spin variables. While the model may appear deceivingly simple, the key difficulty is in determining which classical configurations will lead to the minimum energy. As surprising as it may sound, there is no analytical solution to this problem. The only reliable approach is a hybrid Monte Carlo method that requires diagonalization of Hamiltonian for each Monte Carlo update.

Depending on the strength of Kondo coupling the two limiting cases of the model are as follows:

(i) **Weak coupling :** at $t/|J_K| >> 1$, second order perturbation theory generates an effective long range interaction known as Ruderman-Kittel-Kasuya-Yosida (RKKY) interaction between the localized spins which is mediated by the conduction electrons[71–73]. RKKY Hamiltonian is given by,

$$H_{RKKY} = \sum_{i,j} \mathrm{J}_{ij} \mathbf{S}_i \cdot \mathbf{S}_j. \tag{1.12}$$

(ii) **Strong coupling :** at $t/|J_K| << 1$, we can rewrite the Hamiltonian Eq.(1.11) in a basis where the spin-quantization axes are site dependent and align with the direction of the local magnetic moment[74,75]. Since antiparallel orientations are strongly suppressed for large J_K, the low energy physics is determined by effectively spinless fermions with the spin quantization axis parallel to the local moments. Projecting onto the parallel subspace, we obtain :

$$H_{t-J} = -\sum_{\langle ij \rangle} (t_{ij} c^{\dagger}_{ip} c_{jp} + H.c) + J_{AF} \sum_{\langle ij \rangle} \mathbf{S}_i \cdot \mathbf{S}_j. \tag{1.13}$$

where, $t_{ij} = -t\left[\cos(\frac{\theta_i}{2})\cos(\frac{\theta_j}{2}) + \sin(\frac{\theta_i}{2})\sin(\frac{\theta_j}{2})e^{-\mathrm{i}(\phi_i - \phi_j)}\right]$ depends on the polar and azimuthal angles (θ_i, ϕ_i) of the localised spins. $J_{AF} = 2t^2/J_K$ is the effective antiferromagnetic coupling between the localised spins at neighbouring sites. This model is analogous to the t-J model in large U limit of Hubbard model. The first and second terms of Eq.(1.13) are called double exchange and classical super exchange terms respectively.

1.5.1 Double Exchange Mechanism

For large J_K, the bare energy band splits into two subbands. since, $J_K \to \infty$ we can ignore second term of Eq.(1.13). The strong exchange interaction between localized and itinerant electron spin wants to keep them all aligned. Thus at electronic filling away from half filling, it is not energetically favourable for an itinerant electron to hop to a neighbouring site where the localized spin will be antiparallel. Ferromagnetic alignment of localized spins on neighbouring sites is therefore required. This is called double exchange mechanism, introduced by Zener[76] in 1951 to describe ferromagnetism in the perovskite manganese oxides. This ferromagnetic alignment due to double exchange mechanism occurs in some oxides because of the mixed valency of magnetic ion. For example, $La_{1-x}Sr_xMnO_3$ $(0 \leq x \leq 1)$ in which there is presence of mixture of Mn^{3+} and Mn^{4+} ions. With $x = 0$ and $x = 1$, are both antiferromagnetic insulators, as would be expected for an oxide material in which the magnetism is mediated by superexchange through the oxygen. However when $LaMnO_3$ is doped with Sr up to a level of $x = 0.175$, the material becomes ferromagnetic with a Curie temperature around room temperature, below which it becomes metallic. This we can understand with the help of schematic shown in Fig. 1.5.

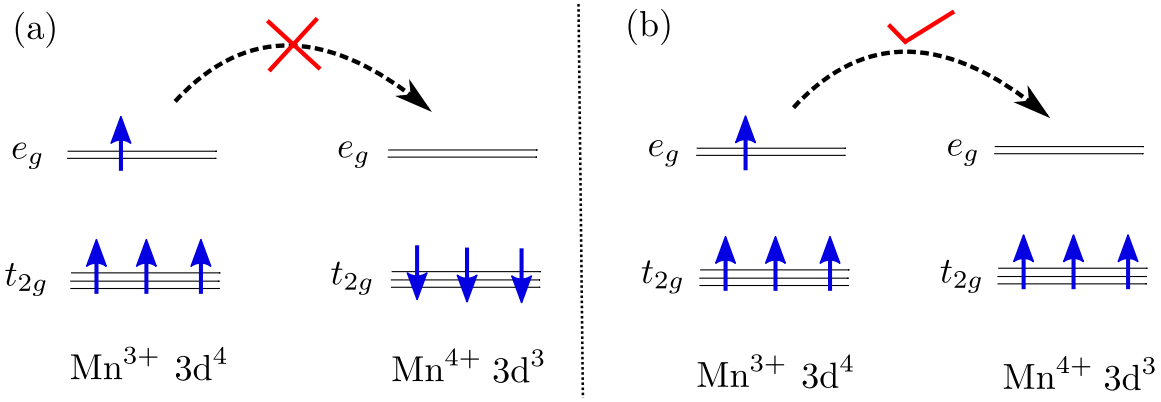

Figure 1.5 Double exchange mechanism gives ferromagnetic coupling between Mn^{3+} and Mn^{4+} ions participating in electron hopping. Exchange interaction doesn't favour hopping if (a) neighbouring ions antiferromagnetically aligned and (b) favors hopping if neighbouring ions are ferromagnetically aligned.

The e_g electron on a Mn^{3+} ion can hop to a neighbouring site where Mn^{4+} which has no electrons in its e_g orbital, this should present no problem. However, there is a strong single-centre (Hund's rule number 1) exchange interaction between the e_g electron and the three electrons in the t_{2g} orbital which wants to keep them all aligned. Thus it is not energetically favourable for an e_g electron to hop to a neighbouring ion in which the t_{2g} spins will be antiparallel to the e_g electron (Fig. 1.5(a)). Ferromagnetic alignment of neighbouring ions is therefore required to maintain the up-spin arrangement on both

the donating and receiving ion. Because the ability to hop gives a kinetic energy saving, allowing the hopping (Fig. 1.5(b)) reduces the overall energy. Thus the system ferromagnetically aligns to save energy. Moreover, the ferromagnetic alignment then allows the e_g electrons to hop through the crystal and the material becomes metallic.

In 1955 Anderson and Hasegawa gave a microscopic derivation of the double-exchange interaction on a two-site Kondo lattice with a ferromagnetic coupling ($J_K < 0$), which models the Hund's rule coupling in the Mn oxides[77,78]. They found that the sign of the coupling was irrelevant for the ferromagnetic ordering within a semiclassical approximation for the localized spins. For $J_K < 0$, the ferromagnetic ordering comes via triplet formation and double-exchange mechanism whereas for $J_K > 0$ there is a competition between singlet formation and double-exchange ordering. When $t/|J_K|$ is small Kondo singlet formation dominates, while as $t/|J_K|$ increases, there is a large energy gain for conduction electron hopping and this favours double-exchange hence the localized spins are then strongly ferromagnetically ordered. This mechanism provides the understanding of ferromagnetic metals, has also played a key role in the description of magnetic and magneto-transport phenomena in, for example, manganites, dilute magnetic semiconductors and Heusler metals[79–81].

1.6 Overview of Thesis

The central theme of the thesis is to explore the physics of metallic systems which contain localised spins interacting with spin orbit coupled itenerant charge carriers. As a result of competing interactions, non trivial magnetization textures emerge in these systems. We present the interesting aspects that we have discovered during this exploration in following chapters.

In **chapter 2** we discuss the Rashba-Dresselhaus spin orbit coupled ferromagnetic Kondo lattice model which is relevant for metallic systems. We then present the detailed analytical calculation of the Hamiltonian in the Double exchange limit. We provide details of Kubo formalism used for electronic transport calculations and derive the current operator for SOC ferromagnetic Kondo lattice model. Since the work of thesis is largely done using numerical simulations, we also discuss the methods and numerical techniques used in the thesis.

In **chapter 3** we propose a microscopic magnetic Hamiltonian for exotic spin textures in metals. Starting from Rashba double exchange model we present the analytical deriva-

tion of an effective spin Hamiltonian. We study the effective spin model using the classical Monte Carlo simulations and map out the phase diagram at low temperatures.

In **chapter 4** we begin with exact calculations on Rashba double exchange model in presence of Zeeman field and show the formation of skyrmions. With the help of the effective spin model we provide an elegant understanding of the conditions under which sparse or packed skyrmion phases emerge in metallic systems. Further, we unveil unique topological features of these skyrmionic phases by computing the Bott index, equivalent of Chern index for disordered systems, and the Hall conductivity.

In **chapter 5** we study double exchange model modified by Dresselhaus SOC in presence of Zeeman field. The form of the Hamiltonian is very similar to Rashba double exchange model. With the help of the effective spin model we understand the similarity and differences between two models. We find that in this model the antiskyrmion phases emerge as ground states. We also map out the Zeeman field vs temperature phase diagram to understand thermal stability of the states. We report the emergence of Bloch skyrmions in these systems by suitably tuning the sign of hopping parameters.

Finally, in **chapter 6** we present a brief summary of the thesis along with some future prospects.

Bibliography

[1] T. Datta-Chaudhuri, P. Abshire and E. Smela, *Lab on a Chip*, 2014, **14**, 1753–1766.

[2] R. Comstock, *Journal of Materials Science: Materials in Electronics*, 2002, **13**, 509–523.

[3] J. S. Meena, S. M. Sze, U. Chand and T.-Y. Tseng, *Nanoscale research letters*, 2014, **9**, 526.

[4] S. M. Yakout.

[5] S.-Q. Shen, *AAPPS Bulletin*, 2008, **18**, 29.

[6] B. Aktas and F. Mikailov, *Advances in Nanoscale Magnetism: Proceedings of the International Conference on Nanoscale Magnetism ICNM-2007, June 25-29, Istanbul, Turkey*, Springer Science & Business Media, 2008, vol. 122.

[7] S. Bhatti, R. Sbiaa, A. Hirohata, H. Ohno, S. Fukami and S. Piramanayagam, *Materials Today*, 2017, **20**, 530–548.

[8] V. K. Joshi, *Engineering science and technology, an international journal*, 2016, **19**, 1503–1513.

[9] S. Wolf, D. Awschalom, R. Buhrman, J. Daughton, v. S. von Molnár, M. Roukes, A. Y. Chtchelkanova and D. Treger, *science*, 2001, **294**, 1488–1495.

[10] A. Hirohata, K. Yamada, Y. Nakatani, L. Prejbeanu, B. Diény, P. Pirro and B. Hillebrands, *Journal of Magnetism and Magnetic Materials*, 2020, 166711.

[11] I. Žutić, J. Fabian and S. D. Sarma, *Reviews of modern physics*, 2004, **76**, 323.

[12] Y. Ando, *Japanese Journal of Applied Physics*, 2015, **54**, 070101.

[13] S. Datta and B. Das, *Applied Physics Letters*, 1990, **56**, 665–667.

[14] B. A. Gurney, *AAPPS Bulletin*, 2008, **18**, 18–23.

[15] H. Zabel, *Superlattices and microstructures*, 2009, **46**, 541–553.

[16] A. Fert, *Angewandte Chemie International Edition*, 2008, **47**, 5956–5967.

[17] J. Ferrer and V. M. Garcia-Suarez, *Journal of Materials Chemistry*, 2009, **19**, 1696–1717.

[18] S. Woo, K. Litzius, B. Krüger, M.-Y. Im, L. Caretta, K. Richter, M. Mann, A. Krone, R. M. Reeve, M. Weigand *et al.*, *Nature materials*, 2016, **15**, 501–506.

[19] X. Yu, W. Koshibae, Y. Tokunaga, K. Shibata, Y. Taguchi, N. Nagaosa and Y. Tokura, *Nature*, 2018, **564**, 95–98.

[20] X. Yu, Y. Onose, N. Kanazawa, J. Park, J. Han, Y. Matsui, N. Nagaosa and Y. Tokura, *Nature*, 2010, **465**, 901–904.

[21] J. Jena, B. Göbel, T. Ma, V. Kumar, R. Saha, I. Mertig, C. Felser and S. S. Parkin, *Nature communications*, 2020, **11**, 1–9.

[22] A. K. Nayak, V. Kumar, T. Ma, P. Werner, E. Pippel, R. Sahoo, F. Damay, U. K. Rößler, C. Felser and S. S. Parkin, *Nature*, 2017, **548**, 561–566.

[23] T. Kurumaji, T. Nakajima, V. Ukleev, A. Feoktystov, T.-h. Arima, K. Kakurai and Y. Tokura, *Physical review letters*, 2017, **119**, 237201.

[24] N. Kanazawa, J.-H. Kim, D. Inosov, J. White, N. Egetenmeyer, J. Gavilano, S. Ishiwata, Y. Onose, T. Arima, B. Keimer *et al.*, *Physical Review B*, 2012, **86**, 134425.

[25] S. Mühlbauer, B. Binz, F. Jonietz, C. Pfleiderer, A. Rosch, A. Neubauer, R. Georgii and P. Böni, *Science*, 2009, **323**, 915–919.

[26] T. Zhou, N. Mohanta, J. E. Han, A. Matos-Abiague and I. Žutić, *Phys. Rev. B*, 2019, **99**, 134505.

[27] J. Kindervater, I. Stasinopoulos, A. Bauer, F. X. Haslbeck, F. Rucker, A. Chacon, S. Mühlbauer, C. Franz, M. Garst, D. Grundler and C. Pfleiderer, *Phys. Rev. X*, 2019, **9**, 041059.

[28] J. Zang, M. Mostovoy, J. H. Han and N. Nagaosa, *Phys. Rev. Lett.*, 2011, **107**, 136804.

[29] S. Sorn, S. Divic and A. Paramekanti, *Phys. Rev. B*, 2019, **100**, 174411.

[30] T. Gao, A. Qaiumzadeh, H. An, A. Musha, Y. Kageyama, J. Shi and K. Ando, *Phys. Rev. Lett.*, 2018, **121**, 017202.

[31] A. Barcza, Z. Gercsi, K. S. Knight and K. G. Sandeman, *Phys. Rev. Lett.*, 2010, **104**, 247202.

[32] X. Z. Yu, D. Morikawa, K. Nakajima, K. Shibata, N. Kanazawa, T. Arima, N. Nagaosa and Y. Tokura, *Science Advances*, 2020, **6**, year.

[33] A. N. Bogdanov and C. Panagopoulos, *arXiv preprint arXiv:2003.09836*, 2020.

[34] A. Fert, N. Reyren and V. Cros, *Nature Reviews Materials*, 2017, **2**, 1–15.

[35] R. Wiesendanger, *Nature Reviews Materials*, 2016, **1**, 1–11.

[36] A. A. Kovalev and S. Sandhoefner, *Frontiers in Physics*, 2018, **6**, 98.

[37] A. Fert, V. Cros and J. Sampaio, *Nat. Nanotechnol.*, 2013, **8**, 152–156.

[38] N. Nagaosa and Y. Tokura, *Nat. Nanotechnol.*, 2013, **8**, 899–911.

[39] B. Göbel, A. Mook, J. Henk and I. Mertig, *Phys. Rev. B*, 2019, **99**, 020405.

[40] B. Dupé, M. Hoffmann, C. Paillard and S. Heinze, *Nature communications*, 2014, **5**, 1–6.

[41] S. D. Pollard, J. A. Garlow, J. Yu, Z. Wang, Y. Zhu and H. Yang, *Nature communications*, 2017, **8**, 1–8.

[42] Y. Zhu, J. Ciston, B. Zheng, X. Miao, C. Czarnik, Y. Pan, R. Sougrat, Z. Lai, C.-E. Hsiung, K. Yao *et al.*, *Nature materials*, 2017, **16**, 532–536.

[43] N. Romming, C. Hanneken, M. Menzel, J. E. Bickel, B. Wolter, K. von Bergmann, A. Kubetzka and R. Wiesendanger, *Science*, 2013, **341**, 636–639.

[44] X. Yu, N. Kanazawa, W. Zhang, T. Nagai, T. Hara, K. Kimoto, Y. Matsui, Y. Onose and Y. Tokura, *Nature communications*, 2012, **3**, 1–6.

[45] X. Yu, N. Kanazawa, Y. Onose, K. Kimoto, W. Zhang, S. Ishiwata, Y. Matsui and Y. Tokura, *Nature materials*, 2011, **10**, 106–109.

[46] X. Zhao, C. Jin, C. Wang, H. Du, J. Zang, M. Tian, R. Che and Y. Zhang, *Proceedings of the National Academy of Sciences*, 2016, **113**, 4918–4923.

[47] S. Meyer, M. Perini, S. von Malottki, A. Kubetzka, R. Wiesendanger, K. von Bergmann and S. Heinze, *Nature communications*, 2019, **10**, 1–8.

[48] A. Tonomura, X. Yu, K. Yanagisawa, T. Matsuda, Y. Onose, N. Kanazawa, H. S. Park and Y. Tokura, *Nano letters*, 2012, **12**, 1673–1677.

[49] M. Hirschberger, T. Nakajima, S. Gao, L. Peng, A. Kikkawa, T. Kurumaji, M. Kriener, Y. Yamasaki, H. Sagayama, H. Nakao *et al.*, *Nature communications*, 2019, **10**, 1–9.

[50] C. Jin, Z.-A. Li, A. Kovács, J. Caron, F. Zheng, F. N. Rybakov, N. S. Kiselev, H. Du, S. Blügel, M. Tian *et al.*, *Nature communications*, 2017, **8**, 1–9.

[51] S. Seki, X. Yu, S. Ishiwata and Y. Tokura, *Science*, 2012, **336**, 198–201.

[52] S. Ishiwata, M. Tokunaga, Y. Kaneko, D. Okuyama, Y. Tokunaga, S. Wakimoto, K. Kakurai, T. Arima, Y. Taguchi and Y. Tokura, *Phys. Rev. B*, 2011, **84**, 054427.

[53] J. White, K. Prša, P. Huang, A. Omrani, I. Živković, M. Bartkowiak, H. Berger, A. Magrez, J. Gavilano, G. Nagy *et al.*, *Physical review letters*, 2014, **113**, 107203.

[54] *The multifaceted skyrmion*, ed. G. E. Brown and M. Rho, World Scientific, Singapore, 2010.

[55] Y. Tokura and N. Kanazawa, *Chemical Reviews*, 2020.

[56] A. Farrell and T. Pereg-Barnea, *Physical Review B*, 2014, **89**, 035112.

[57] J. Chen, D.-W. Zhang and J.-M. Liu, *Scientific reports*, 2016, **6**, 29126.

[58] U. K. Rößler, A. A. Leonov and A. N. Bogdanov, Journal of Physics: Conference Series, 2010, p. 022029.

[59] U. K. Roessler, A. Bogdanov and C. Pfleiderer, *Nature*, 2006, **442**, 797–801.

[60] N. Mohanta, E. Dagotto and S. Okamoto, *Physical Review B*, 2019, **100**, 064429.

[61] J. Iwasaki, A. J. Beekman and N. Nagaosa, *Physical Review B*, 2014, **89**, 064412.

[62] S. D. Yi, S. Onoda, N. Nagaosa and J. H. Han, *Phys. Rev. B*, 2009, **80**, 054416.

[63] S. Hayami and Y. Motome, *Phys. Rev. Lett.*, 2018, **121**, 137202.

[64] S. Hayami and Y. Motome, *Phys. Rev. B*, 2019, **99**, 094420.

[65] Z. Wang, Y. Su, S.-Z. Lin and C. D. Batista, *Phys. Rev. Lett.*, 2020, **124**, 207201.

[66] A. V. Bezvershenko, A. K. Kolezhuk and B. A. Ivanov, *Phys. Rev. B*, 2018, **97**, 054408.

[67] B. Göbel, A. Mook, J. Henk and I. Mertig, *The European Physical Journal B*, 2018, **91**, 179.

[68] M. Chapman and C. S. De Melo, *Nature*, 2011, **471**, 41–42.

[69] A. Manchon, H. C. Koo, J. Nitta, S. Frolov and R. Duine, *Nature materials*, 2015, **14**, 871–882.

[70] M. Gulácsi*, *Advances in physics*, 2004, **53**, 769–937.

[71] M. A. Ruderman and C. Kittel, *Phys. Rev.*, 1954, **96**, 99–102.

[72] T. Kasuya, *Progress of Theoretical Physics*, 1956, **16**, 45–57.

[73] K. Yosida, *Phys. Rev.*, 1957, **106**, 893–898.

[74] D. Pekker, S. Mukhopadhyay, N. Trivedi and P. M. Goldbart, *Phys. Rev. B*, 2005, **72**, 075118.

[75] S. Kumar, J. van den Brink and A. P. Kampf, *Phys. Rev. Lett.*, 2010, **104**, 017201.

[76] C. Zener, *Phys. Rev.*, 1951, **82**, 403–405.

[77] P. W. Anderson and H. Hasegawa, *Phys. Rev.*, 1955, **100**, 675–681.

[78] P. G. de Gennes, *Phys. Rev.*, 1960, **118**, 141–154.

[79] E. Dagotto, *Nanoscale phase separation and colossal magnetoresistance: the physics of manganites and related compounds*, Springer Science & Business Media, 2013, vol. 136.

[80] K. Pradhan and S. K. Das, *Scientific reports*, 2017, **7**, 1–6.

[81] D. Bombor, C. G. Blum, O. Volkonskiy, S. Rodan, S. Wurmehl, C. Hess and B. Büchner, *Physical review letters*, 2013, **110**, 066601.

2

Model and Methods

In this chapter we present the Rashba Dresselhaus spin orbit coupled Kondo lattice model Hamiltonian which is relevant for metals. First we derive the same Hamiltonian in the double exchange limit and finally derive a new effective spin Hamiltonian. Kubo formalism for calculations of longitudinal, transverse conductivities and spin Hall conductivities is discussed. We derive the Kubo formulas for spin Hall conductivities in double exchange limit. Methods used in simulations are also discussed.

2.1 Introduction - Kondo Lattice Model

The Kondo lattice is one of the most important canonical models used to study strongly correlated electron systems because of its relevance to several broad classes of real materials as discussed in Chapter 1. The Kondo lattice Model describes the interaction between a conduction band, itinerant electrons, and a lattice of localized magnetic moments[1] (see Fig. 2.1).

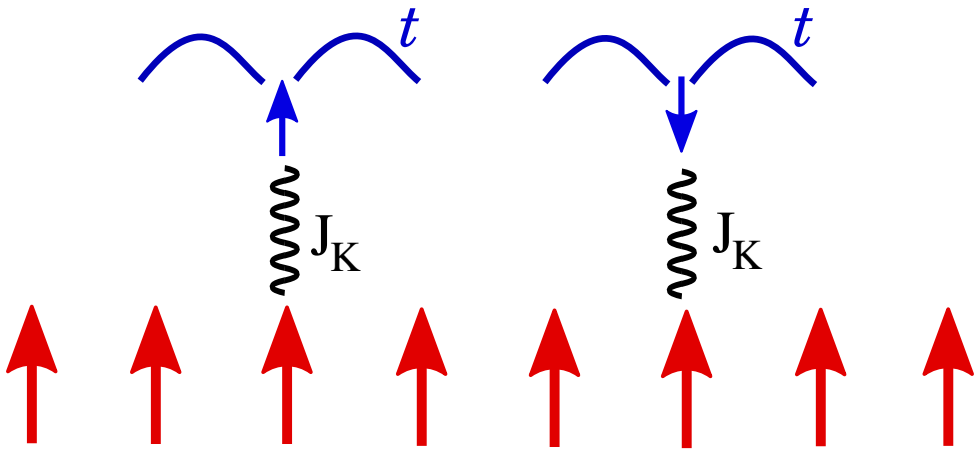

Figure 2.1 Schematic diagram showing the classical localized moments coupled to itinerant electron spins.

The Hamiltonian for Ferromagnetic Kondo Lattice Model is given by,

$$\begin{aligned} H &= H_t + H_{Kondo} \\ &= -t \sum_{\langle ij\rangle,\sigma} (c^{\dagger}_{i\sigma} c_{j\sigma} + H.c) - J_K \sum_i \mathbf{S}_i \cdot \mathbf{s}_i. \end{aligned} \tag{2.1}$$

where, the first term is usual tight binding hopping between nearest neighbor sites. $c_{i\sigma}(c^{\dagger}_{i\sigma})$ is the annihilation (creation) operator for electron at site i with spin σ, $\langle ij\rangle$ implies that sites i and j are nearest neighbors. The second term is the coupling between localized spins and itenerant electron spin at each site. $J_K > 0$ denote the strength of ferromagnetic Kondo coupling. $\mathbf{S}_i$ denotes the classical localized spin at site i and $\mathbf{s}_i$ is the spin operator for an electron at that site. We can expand second term as:

$$H_{Kondo} = -\frac{J_K}{2} \sum_{i,\mu} S^{\mu}_i \cdot \sigma^{\mu}_i. \tag{2.2}$$

$$H_{Kondo} = -\frac{J_K}{2} \sum_i [S^x_i (c^{\dagger}_{i\uparrow} c_{i\downarrow} + c^{\dagger}_{i\downarrow} c_{i\uparrow}) - \mathrm{i} S^y_i (c^{\dagger}_{i\uparrow} c_{i\downarrow} - c^{\dagger}_{i\downarrow} c_{i\uparrow}) + S^z_i (c^{\dagger}_{i\uparrow} c_{i\uparrow} - c^{\dagger}_{i\downarrow} c_{i\downarrow})]. \tag{2.3}$$

where,

$$\begin{aligned}
\sigma^x &= \begin{bmatrix} 0 & 1 \\ 1 & 0 \end{bmatrix} = c^\dagger_{i\uparrow}c_{i\downarrow} + c^\dagger_{i\downarrow}c_{i\uparrow}, \\
\sigma^y &= \begin{bmatrix} 0 & -\mathrm{i} \\ \mathrm{i} & 0 \end{bmatrix} = -\mathrm{i}(c^\dagger_{i\uparrow}c_{i\downarrow} - c^\dagger_{i\downarrow}c_{i\uparrow}), \\
\sigma^z &= \begin{bmatrix} 1 & 0 \\ 0 & -1 \end{bmatrix} = c^\dagger_{i\uparrow}c_{i\uparrow} - c^\dagger_{i\downarrow}c_{i\downarrow}.
\end{aligned} \tag{2.4}$$

are Pauli matrices.

2.2 Rashba Dresselhaus Spin Orbit Coupling

As discussed in Chapter 1, Rashba and Dresselhaus spin-orbit coupling Hamiltonian in 2D continuum system is,

$$H = \alpha(P_y\sigma^x - P_x\sigma^y) + \beta(P_x\sigma^x - P_y\sigma^y) \tag{2.5}$$

The presence of Rashba and Dresselhaus spin orbit coupling on a square lattice is described by the Hamiltonian[2],

$$H = \mathrm{i}\sum_{i,\sigma,\sigma'}(c^\dagger_{i,\sigma}\hat{\Lambda}_1 c_{i+y,\sigma'} - c^\dagger_{i,\sigma}\hat{\Lambda}_2 c_{i+x,\sigma'} - H.c) \tag{2.6}$$

where, The operators, $\hat{\Lambda}_1 = \lambda_R\sigma^x - \lambda_D\sigma^y$ and $\hat{\Lambda}_2 = \lambda_R\sigma^y - \lambda_D\sigma^x$ written in terms of Rashba (λ_R) and Dresselhaus (λ_D) spin orbit coupling strengths and Pauli matrices. Equation (2.6) can be expanded as:

$$\begin{aligned}
H = \sum_i [&(\lambda_R + \mathrm{i}\lambda_D)c^\dagger_{i\downarrow}c_{i+x\uparrow} - (\lambda_R - \mathrm{i}\lambda_D)c^\dagger_{i\uparrow}c_{i+x\downarrow} \\
&+(\lambda_D + \mathrm{i}\lambda_R)c^\dagger_{i\downarrow}c_{i+y\uparrow} - (\lambda_D - \mathrm{i}\lambda_R)c^\dagger_{i\uparrow}c_{i+y\downarrow}] + H.c
\end{aligned} \tag{2.7}$$

If $\lambda_D = 0$, we have Rashba SOC Hamiltonian

$$H_R = \lambda_R\sum_i [(c^\dagger_{i\downarrow}c_{i+x\uparrow} - c^\dagger_{i\uparrow}c_{i+x\downarrow}) + \mathrm{i}(c^\dagger_{i\downarrow}c_{i+y\uparrow} + c^\dagger_{i\uparrow}c_{i+y\downarrow})] + H.c, \tag{2.8}$$

and if $\lambda_R = 0$, we have Dresselhaus SOC Hamiltonian

$$H_D = \lambda_D \sum_i [\mathrm{i}(c^\dagger_{i\downarrow} c_{i+x\uparrow} + c^\dagger_{i\uparrow} c_{i+x\downarrow}) + (c^\dagger_{i\downarrow} c_{i+y\uparrow} - c^\dagger_{i\uparrow} c_{i+y\downarrow})] + H.c. \tag{2.9}$$

The tight-binding model with Rashba and Dresselhaus SOC on a square lattice is described by the Hamiltonian,

$$\begin{aligned} H &= -t \sum_{\langle ij\rangle,\sigma} (c^\dagger_{i\sigma} c_{j\sigma} + H.c) \\ &+ \sum_i [(\lambda_R + \mathrm{i}\lambda_D) c^\dagger_{i\downarrow} c_{i+x\uparrow} - (\lambda_R - \mathrm{i}\lambda_D) c^\dagger_{i\uparrow} c_{i+x\downarrow} \\ &+ (\lambda_D + \mathrm{i}\lambda_R) c^\dagger_{i\downarrow} c_{i+y\uparrow} - (\lambda_D - \mathrm{i}\lambda_R) c^\dagger_{i\uparrow} c_{i+y\downarrow}] + H.c. \end{aligned} \tag{2.10}$$

using,

$$c_{i\sigma} = \frac{1}{\sqrt{N}} \sum_{\mathbf{k}} e^{-\mathrm{i}\mathbf{k}\cdot\mathbf{r_i}} c_{\mathbf{k}\sigma},$$

$$\frac{1}{N} \sum_i e^{\mathrm{i}(\mathbf{k}-\mathbf{k}')\cdot\mathbf{r_i}} = \delta_{\mathbf{k}\mathbf{k}'},$$

with definitions,

$$\begin{aligned} S_1 &= \lambda_R \sin(k_y) + \lambda_D \sin(k_x), \\ S_2 &= \lambda_R \sin(k_x) + \lambda_D \sin(k_y), \end{aligned} \tag{2.11}$$

we get,

$$\begin{aligned} H &= \sum_{\mathbf{k}} -2t(\cos(k_x) + \cos(k_y)) c^\dagger_{\mathbf{k}\uparrow} c_{\mathbf{k}\uparrow} - 2t(\cos(k_x) + \cos(k_y)) c^\dagger_{\mathbf{k}\downarrow} c_{\mathbf{k}\downarrow} \\ &+ 2(S_1 + \mathrm{i}S_2) c^\dagger_{\mathbf{k}\uparrow} c_{\mathbf{k}\downarrow} + 2(S_1 - \mathrm{i}S_2) c^\dagger_{\mathbf{k}\downarrow} c_{\mathbf{k}\uparrow}. \end{aligned} \tag{2.12}$$

By diagonalizing the Hamiltonian in momentum space, we obatain the eigenvalues

$$\varepsilon_{k\pm} = -2t(\cos(k_x) + \cos(k_y)) \pm 2\sqrt{S_1^2 + S_2^2} \tag{2.13}$$

and eigenvectors

$$\Psi_{k\pm} = \frac{1}{\sqrt{2}} \left[c^\dagger_{\mathbf{k}\uparrow} \pm \frac{S_1 - \mathrm{i}S_2}{\sqrt{S_1^2 + S_2^2}} c^\dagger_{\mathbf{k}\downarrow} \right] |0\rangle. \tag{2.14}$$

So the Hamiltonian Eq.(2.14) has two bands of chiral eigenstates. The chiral states are of different nature for pure Rashba and pure Dresselhaus SOC cases as shown in (Fig. 2.2).

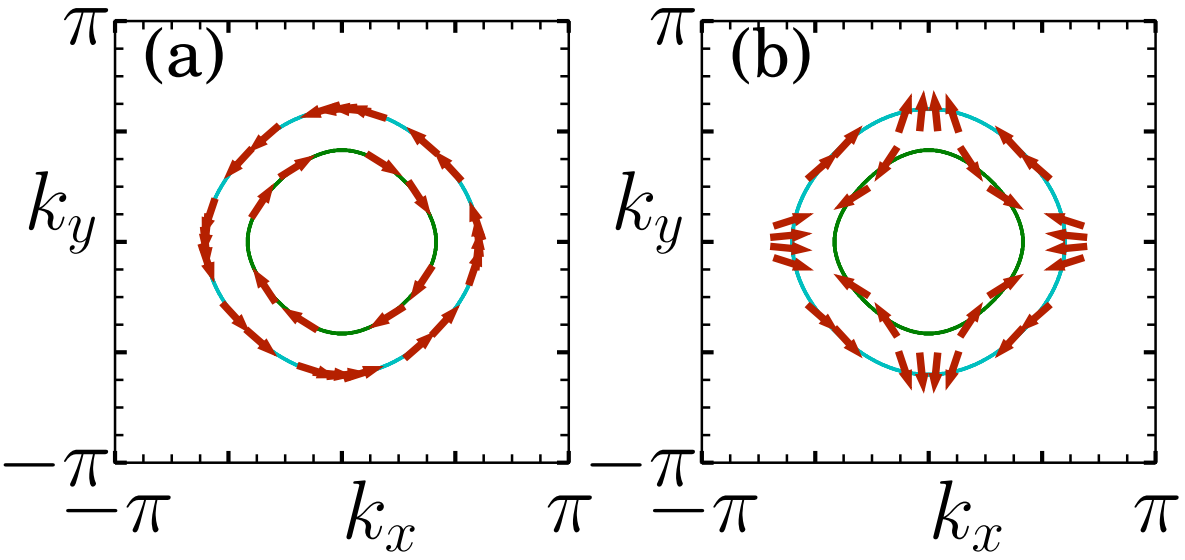

Figure 2.2 Fermi contours at $1/5$ filling for (a) pure Rashba SOC ($\lambda_R = 0.3$, $\lambda_D = 0.0$) , (b) pure Dresselhaus SOC ($\lambda_R = 0.0$, $\lambda_D = 0.3$). Hopping parameter, $t = 1.0$ for the calculation.

2.3 Rashba Dresselhaus Kondo Lattice Model

The FKLM in the presence of Rashba and Dresselhaus SOC on a square lattice in global quantization axis frame is described by the Hamiltonian,

$$\begin{aligned} H &= H_t + H_R + H_D + H_{Kondo} \\ &= -t \sum_{\langle ij\rangle,\sigma} (c^\dagger_{i\sigma} c_{j\sigma} + H.c) \\ &\quad + \lambda_R \sum_i [(c^\dagger_{i\downarrow} c_{i+x\uparrow} - c^\dagger_{i\uparrow} c_{i+x\downarrow}) + \mathrm{i}(c^\dagger_{i\downarrow} c_{i+y\uparrow} + c^\dagger_{i\uparrow} c_{i+y\downarrow})] + H.c \\ &\quad + \lambda_D \sum_i [\mathrm{i}(c^\dagger_{i\downarrow} c_{i+x\uparrow} + c^\dagger_{i\uparrow} c_{i+x\downarrow}) + (c^\dagger_{i\downarrow} c_{i+y\uparrow} - c^\dagger_{i\uparrow} c_{i+y\downarrow})] + H.c \\ &\quad - J_K \sum_i \mathbf{S}_i \cdot \mathbf{s}_i. \end{aligned} \tag{2.15}$$

We re-write the Hamiltonian in a frame of reference which has site-dependent quantization axis pointing along the local classical spins direction. This transforms the Hamiltonian in new operators, $d_{ip}(d_{ia})$ which annihilates an electron at site i with spin parallel (antiparallel) to the localized spin. This is achieved by performing a site dependent rotation of the spin-$\frac{1}{2}$ basis given by the canonical SU(2) transformations[3],

$$\begin{bmatrix} c_{i\uparrow} \\ c_{i\downarrow} \end{bmatrix} = \begin{bmatrix} \eta_i & \eta_i' \end{bmatrix} \begin{bmatrix} d_{ip} \\ d_{ia} \end{bmatrix} \tag{2.16}$$

where,

$$\begin{aligned}\eta_i &= e^{i\chi_i}\begin{bmatrix}\cos\left(\frac{\theta_i}{2}\right)e^{-i\phi_i/2}\\ \sin\left(\frac{\theta_i}{2}\right)e^{i\phi_i/2}\end{bmatrix},\\ \eta_i^{'} &= e^{-i\chi_i}\begin{bmatrix}-\sin\left(\frac{\theta_i}{2}\right)e^{-i\phi_i/2}\\ \cos\left(\frac{\theta_i}{2}\right)e^{i\phi_i/2}\end{bmatrix}\end{aligned} \tag{2.17}$$

are the spinors defined in terms of θ_i, ϕ_i are the polar and azimuthal angles describe the direction of the local spin $\mathbf{S}_i$ and phase factor, χ_i is a gauge freedom. For follow up derivations we use $\chi_i = \phi_i/2$. That is,

$$\begin{bmatrix}c_{i\uparrow}\\ c_{i\downarrow}\end{bmatrix} = \begin{bmatrix}\cos\left(\frac{\theta_i}{2}\right) & -\sin\left(\frac{\theta_i}{2}\right)e^{-i\phi_i}\\ \sin\left(\frac{\theta_i}{2}\right)e^{i\phi_i} & \cos\left(\frac{\theta_i}{2}\right)\end{bmatrix}\begin{bmatrix}d_{ip}\\ d_{ia}\end{bmatrix} \tag{2.18}$$

which gives,

$$\begin{aligned}c_{i\uparrow} &= \cos\left(\frac{\theta_i}{2}\right)d_{ip} - \sin\left(\frac{\theta_i}{2}\right)e^{-i\phi_i}d_{ia},\\ c_{i\downarrow} &= \sin\left(\frac{\theta_i}{2}\right)e^{i\phi_i}d_{ip} + \cos\left(\frac{\theta_i}{2}\right)d_{ia},\\ c_{i\uparrow}^{\dagger} &= \cos\left(\frac{\theta_i}{2}\right)d_{ip}^{\dagger} - \sin\left(\frac{\theta_i}{2}\right)e^{i\phi_i}d_{ia}^{\dagger},\\ c_{i\downarrow}^{\dagger} &= \sin\left(\frac{\theta_i}{2}\right)e^{-i\phi_i}d_{ip}^{\dagger} + \cos\left(\frac{\theta_i}{2}\right)d_{ia}^{\dagger}.\end{aligned} \tag{2.19}$$

where, $d_{ip}^{\dagger}(d_{ia}^{\dagger})$ creates an electron at site i with spin parallel (antiparallel) to the localized spin. These transformations Eq.(2.19) modify the various terms of the Hamiltonian Eq.(2.15) as we describe in detail below.

2.3.1 Tight Binding Term

The Tight Binding term of the Hamiltonian Eq.(2.15) is,

$$H_t = -t\sum_{\langle ij\rangle}(c_{i\uparrow}^{\dagger}c_{j\uparrow} + c_{i\downarrow}^{\dagger}c_{j\downarrow}) + H.c \tag{2.20}$$

where, site $j = i + \gamma$ is the nn of site i along spatial direction $\gamma \in \{x, y\}$. Using the transformations Eq.(2.19), we get

$$\begin{aligned} H_t &= -t \sum_{\langle ij \rangle} \Big[\Big(\cos\Big(\frac{\theta_i}{2}\Big) d_{ip}^\dagger - \sin\Big(\frac{\theta_i}{2}\Big) e^{i\phi_i} d_{ia}^\dagger \Big) \Big(\cos\Big(\frac{\theta_j}{2}\Big) d_{jp} - \sin\Big(\frac{\theta_j}{2}\Big) e^{-i\phi_j} d_{ja} \Big) \Big] \\ &\quad + \Big[\Big(\sin\Big(\frac{\theta_i}{2}\Big) e^{-i\phi_i} d_{ip}^\dagger + \cos\Big(\frac{\theta_i}{2}\Big) d_{ia}^\dagger \Big) \Big(\sin\Big(\frac{\theta_j}{2}\Big) e^{i\phi_j} d_{jp} + \cos\Big(\frac{\theta_j}{2}\Big) d_{ja} \Big) \Big] + H.c \end{aligned} \tag{2.21}$$

Expanding Eq.(2.21) we get the various terms of Tight Binding Hamiltonian ,

$$h_t^{pp} = -t \sum_{\langle ij \rangle} \Big[\cos\Big(\frac{\theta_i}{2}\Big) \cos\Big(\frac{\theta_j}{2}\Big) + \sin\Big(\frac{\theta_i}{2}\Big) \sin\Big(\frac{\theta_j}{2}\Big) e^{-i(\phi_i - \phi_j)} \Big] d_{ip}^\dagger d_{jp}, \tag{2.22}$$

$$h_t^{pa} = -t \sum_{\langle ij \rangle} \Big[\sin\Big(\frac{\theta_i}{2}\Big) \cos\Big(\frac{\theta_j}{2}\Big) e^{-i\phi_i} - \cos\Big(\frac{\theta_i}{2}\Big) \sin\Big(\frac{\theta_j}{2}\Big) e^{-i\phi_j} \Big] d_{ip}^\dagger d_{ja}, \tag{2.23}$$

$$h_t^{ap} = -t \sum_{\langle ij \rangle} \Big[-\sin\Big(\frac{\theta_i}{2}\Big) \cos\Big(\frac{\theta_j}{2}\Big) e^{i\phi_i} + \cos\Big(\frac{\theta_i}{2}\Big) \sin\Big(\frac{\theta_j}{2}\Big) e^{i\phi_j} \Big] d_{ia}^\dagger d_{jp}, \tag{2.24}$$

$$h_t^{aa} = -t \sum_{\langle ij \rangle} \Big[\sin\Big(\frac{\theta_i}{2}\Big) \sin\Big(\frac{\theta_j}{2}\Big) e^{i(\phi_i - \phi_j)} + \cos\Big(\frac{\theta_i}{2}\Big) \cos\Big(\frac{\theta_j}{2}\Big) \Big] d_{ia}^\dagger d_{ja}. \tag{2.25}$$

2.3.2 Rashba SOC Term

We transform the Rashba SOC terms of the Hamiltonian Eq.(2.15) along x and y directions using Eq.(2.19)

along x $(j = i + x)$

$$\begin{aligned} H_R(x) &= \lambda_R \sum_{\langle ij \rangle} (c_{i\downarrow}^\dagger c_{j\uparrow} - c_{i\uparrow}^\dagger c_{j\downarrow}) + H.c \\ &= \lambda_R \sum_{\langle ij \rangle} \Big[\Big(\sin\Big(\frac{\theta_i}{2}\Big) e^{-i\phi_i} d_{ip}^\dagger + \cos\Big(\frac{\theta_i}{2}\Big) d_{ia}^\dagger \Big) \Big(\cos\Big(\frac{\theta_j}{2}\Big) d_{jp} - \sin\Big(\frac{\theta_j}{2}\Big) e^{-i\phi_j} d_{ja} \Big) \Big] \\ &\quad - \Big[\Big(\cos\Big(\frac{\theta_i}{2}\Big) d_{ip}^\dagger - \sin\Big(\frac{\theta_i}{2}\Big) e^{i\phi_i} d_{ia}^\dagger \Big) \Big(\sin\Big(\frac{\theta_j}{2}\Big) e^{i\phi_j} d_{jp} + \cos\Big(\frac{\theta_j}{2}\Big) d_{ja} \Big) \Big] + H.c \end{aligned} \tag{2.26}$$

$$h_R^{pp}(x) = \lambda_R \sum_{\langle ij \rangle} \Big[\sin\Big(\frac{\theta_i}{2}\Big)\cos\Big(\frac{\theta_j}{2}\Big)e^{-\mathrm{i}\phi_i} - \cos\Big(\frac{\theta_i}{2}\Big)\sin\Big(\frac{\theta_j}{2}\Big)e^{\mathrm{i}\phi_j}\Big] d_{ip}^\dagger d_{jp}, \quad (2.27)$$

$$h_R^{pa}(x) = \lambda_R \sum_{\langle ij \rangle} \Big[-\sin\Big(\frac{\theta_i}{2}\Big)\sin\Big(\frac{\theta_j}{2}\Big)e^{-\mathrm{i}(\phi_i+\phi_j)} - \cos\Big(\frac{\theta_i}{2}\Big)\cos\Big(\frac{\theta_j}{2}\Big)\Big] d_{ip}^\dagger d_{ja}, \quad (2.28)$$

$$h_R^{ap}(x) = \lambda_R \sum_{\langle ij \rangle} \Big[\cos\Big(\frac{\theta_i}{2}\Big)\cos\Big(\frac{\theta_j}{2}\Big) + \sin\Big(\frac{\theta_i}{2}\Big)\sin\Big(\frac{\theta_j}{2}\Big)e^{\mathrm{i}(\phi_i+\phi_j)}\Big] d_{ia}^\dagger d_{jp}, \quad (2.29)$$

$$h_R^{aa}(x) = \lambda_R \sum_{\langle ij \rangle} \Big[-\cos\Big(\frac{\theta_i}{2}\Big)\sin\Big(\frac{\theta_j}{2}\Big)e^{-\mathrm{i}\phi_j} + \sin\Big(\frac{\theta_i}{2}\Big)\cos\Big(\frac{\theta_j}{2}\Big)e^{\mathrm{i}\phi_i}\Big] d_{ia}^\dagger d_{ja}. \quad (2.30)$$

along y $(j = i + y)$

$$\begin{aligned} H_R(y) &= \mathrm{i}\lambda_R \sum_{\langle ij \rangle} (c_{i\downarrow}^\dagger c_{j\uparrow} + c_{i\uparrow}^\dagger c_{j\downarrow}) + H.c \\ &= \mathrm{i}\lambda_R \sum_{\langle ij \rangle} \Big[\Big(\sin\Big(\frac{\theta_i}{2}\Big)e^{-\mathrm{i}\phi_i} d_{ip}^\dagger + \cos\Big(\frac{\theta_i}{2}\Big) d_{ia}^\dagger \Big) \Big(\cos\Big(\frac{\theta_j}{2}\Big) d_{jp} - \sin\Big(\frac{\theta_j}{2}\Big)e^{-\mathrm{i}\phi_j} d_{ja} \Big) \Big] \\ &\quad + \Big[\Big(\cos\Big(\frac{\theta_i}{2}\Big) d_{ip}^\dagger - \sin\Big(\frac{\theta_i}{2}\Big)e^{\mathrm{i}\phi_i} d_{ia}^\dagger \Big) \Big(\sin\Big(\frac{\theta_j}{2}\Big)e^{\mathrm{i}\phi_j} d_{jp} + \cos\Big(\frac{\theta_j}{2}\Big) d_{ja} \Big) \Big] + H.c \end{aligned} \quad (2.31)$$

$$h_R^{pp}(y) = \mathrm{i}\lambda_R \sum_{\langle ij \rangle} \Big[\cos\Big(\frac{\theta_i}{2}\Big)\sin\Big(\frac{\theta_j}{2}\Big)e^{\mathrm{i}\phi_j} + \sin\Big(\frac{\theta_i}{2}\Big)\cos\Big(\frac{\theta_j}{2}\Big)e^{-\mathrm{i}\phi_i}\Big] d_{ip}^\dagger d_{jp}, \quad (2.32)$$

$$h_R^{pa}(y) = \mathrm{i}\lambda_R \sum_{\langle ij \rangle} \Big[\cos\Big(\frac{\theta_i}{2}\Big)\cos\Big(\frac{\theta_j}{2}\Big) - \sin\Big(\frac{\theta_i}{2}\Big)\sin\Big(\frac{\theta_j}{2}\Big)e^{-\mathrm{i}(\phi_i+\phi_j)}\Big] d_{ip}^\dagger d_{ja}, \quad (2.33)$$

$$h_R^{ap}(y) = \mathrm{i}\lambda_R \sum_{\langle ij \rangle} \Big[-\sin\Big(\frac{\theta_i}{2}\Big)\sin\Big(\frac{\theta_j}{2}\Big)e^{\mathrm{i}(\phi_i+\phi_j)} + \cos\Big(\frac{\theta_i}{2}\Big)\cos\Big(\frac{\theta_j}{2}\Big)\Big] d_{ia}^\dagger d_{jp}, \quad (2.34)$$

$$h_R^{aa}(y) = \mathrm{i}\lambda_R \sum_{\langle ij\rangle} \Big[-\sin\Big(\frac{\theta_i}{2}\Big)\cos\Big(\frac{\theta_j}{2}\Big)e^{\mathrm{i}\phi_i} - \cos\Big(\frac{\theta_i}{2}\Big)\sin\Big(\frac{\theta_j}{2}\Big)e^{-\mathrm{i}\phi_j}\Big] d_{ia}^{\dagger} d_{ja}. \quad (2.35)$$

2.3.3 Dresselhaus SOC Term

Similarly, we transform the Dresselhaus SOC terms of the Hamiltonian Eq.(2.15) along x and y directions using Eq.(2.19)

along x $(j = i + x)$

$$\begin{aligned} H_D(x) &= \mathrm{i}\lambda_D \sum_{\langle ij\rangle} (c_{i\downarrow}^{\dagger} c_{j\uparrow} + c_{i\uparrow}^{\dagger} c_{j\downarrow}) + H.c \\ &= \mathrm{i}\lambda_D \sum_{\langle ij\rangle} \Big[\Big(\sin\Big(\frac{\theta_i}{2}\Big)e^{-\mathrm{i}\phi_i} d_{ip}^{\dagger} + \cos\Big(\frac{\theta_i}{2}\Big) d_{ia}^{\dagger} \Big) \Big(\cos\Big(\frac{\theta_j}{2}\Big) d_{jp} - \sin\Big(\frac{\theta_j}{2}\Big)e^{-\mathrm{i}\phi_j} d_{ja} \Big) \Big] \\ &\quad + \Big[\Big(\cos\Big(\frac{\theta_i}{2}\Big) d_{ip}^{\dagger} - \sin\Big(\frac{\theta_i}{2}\Big)e^{\mathrm{i}\phi_i} d_{ia}^{\dagger} \Big) \Big(\sin\Big(\frac{\theta_j}{2}\Big)e^{\mathrm{i}\phi_j} d_{jp} + \cos\Big(\frac{\theta_j}{2}\Big) d_{ja} \Big) \Big] + H.c \end{aligned} \quad (2.36)$$

$$h_D^{pp}(x) = \mathrm{i}\lambda_D \sum_{\langle ij\rangle} \Big[\cos\Big(\frac{\theta_i}{2}\Big)\sin\Big(\frac{\theta_j}{2}\Big)e^{\mathrm{i}\phi_j} + \sin\Big(\frac{\theta_i}{2}\Big)\cos\Big(\frac{\theta_j}{2}\Big)e^{-\mathrm{i}\phi_i}\Big] d_{ip}^{\dagger} d_{jp}, \quad (2.37)$$

$$h_D^{pa}(x) = \mathrm{i}\lambda_D \sum_{\langle ij\rangle} \Big[\cos\Big(\frac{\theta_i}{2}\Big)\cos\Big(\frac{\theta_j}{2}\Big) - \sin\Big(\frac{\theta_i}{2}\Big)\sin\Big(\frac{\theta_j}{2}\Big)e^{-\mathrm{i}(\phi_i+\phi_j)}\Big] d_{ip}^{\dagger} d_{ja}, \quad (2.38)$$

$$h_D^{ap}(x) = \mathrm{i}\lambda_D \sum_{\langle ij\rangle} \Big[-\sin\Big(\frac{\theta_i}{2}\Big)\sin\Big(\frac{\theta_j}{2}\Big)e^{\mathrm{i}(\phi_i+\phi_j)} + \cos\Big(\frac{\theta_i}{2}\Big)\cos\Big(\frac{\theta_j}{2}\Big)\Big] d_{ia}^{\dagger} d_{jp}, \quad (2.39)$$

$$h_D^{aa}(x) = \mathrm{i}\lambda_D \sum_{\langle ij\rangle} \Big[-\sin\Big(\frac{\theta_i}{2}\Big)\cos\Big(\frac{\theta_j}{2}\Big)e^{\mathrm{i}\phi_i} - \cos\Big(\frac{\theta_i}{2}\Big)\sin\Big(\frac{\theta_j}{2}\Big)e^{-\mathrm{i}\phi_j}\Big] d_{ia}^{\dagger} d_{ja}. \quad (2.40)$$

along y $(j = i+y)$

$$\begin{aligned} H_D(y) &= \lambda_D \sum_{\langle ij \rangle} (c^\dagger_{i\downarrow} c_{j\uparrow} - c^\dagger_{i\uparrow} c_{j\downarrow}) + H.c \\ &= \lambda_D \sum_{\langle ij \rangle} \left[\left(\sin\left(\frac{\theta_i}{2}\right) e^{-i\phi_i} d^\dagger_{ip} + \cos\left(\frac{\theta_i}{2}\right) d^\dagger_{ia} \right) \left(\cos\left(\frac{\theta_j}{2}\right) d_{jp} - \sin\left(\frac{\theta_j}{2}\right) e^{-i\phi_j} d_{ja} \right) \right] \\ &\quad - \left[\left(\cos\left(\frac{\theta_i}{2}\right) d^\dagger_{ip} - \sin\left(\frac{\theta_i}{2}\right) e^{i\phi_i} d^\dagger_{ia} \right) \left(\sin\left(\frac{\theta_j}{2}\right) e^{i\phi_j} d_{jp} + \cos\left(\frac{\theta_j}{2}\right) d_{ja} \right) \right] + H.c \end{aligned} \tag{2.41}$$

$$h^{pp}_D(y) = \lambda_D \sum_{\langle ij \rangle} \left[\sin\left(\frac{\theta_i}{2}\right) \cos\left(\frac{\theta_j}{2}\right) e^{-i\phi_i} - \cos\left(\frac{\theta_i}{2}\right) \sin\left(\frac{\theta_j}{2}\right) e^{i\phi_j} \right] d^\dagger_{ip} d_{jp}, \tag{2.42}$$

$$h^{pa}_D(y) = \lambda_D \sum_{\langle ij \rangle} \left[-\sin\left(\frac{\theta_i}{2}\right) \sin\left(\frac{\theta_j}{2}\right) e^{-i(\phi_i+\phi_j)} - \cos\left(\frac{\theta_i}{2}\right) \cos\left(\frac{\theta_j}{2}\right) \right] d^\dagger_{ip} d_{ja}, \tag{2.43}$$

$$h^{ap}_D(y) = \lambda_D \sum_{\langle ij \rangle} \left[\cos\left(\frac{\theta_i}{2}\right) \cos\left(\frac{\theta_j}{2}\right) + \sin\left(\frac{\theta_i}{2}\right) \sin\left(\frac{\theta_j}{2}\right) e^{i(\phi_i+\phi_j)} \right] d^\dagger_{ia} d_{jp}, \tag{2.44}$$

$$h^{aa}_D(y) = \lambda_D \sum_{\langle ij \rangle} \left[-\cos\left(\frac{\theta_i}{2}\right) \sin\left(\frac{\theta_j}{2}\right) e^{-i\phi_j} + \sin\left(\frac{\theta_i}{2}\right) \cos\left(\frac{\theta_j}{2}\right) e^{i\phi_i} \right] d^\dagger_{ia} d_{ja}. \tag{2.45}$$

2.3.4 Kondo Term

Pauli matrices Eq.(2.4) transform in new operators using Eq.(2.19) as:

$$\begin{aligned} \sigma^x &= \begin{bmatrix} \sin(\theta_i)\cos(\phi_i) & \cos^2\left(\frac{\theta_i}{2}\right) - \sin^2\left(\frac{\theta_i}{2}\right) e^{-i2\phi_i} \\ \cos^2\left(\frac{\theta_i}{2}\right) - \sin^2\left(\frac{\theta_i}{2}\right) e^{i2\phi_i} & -\sin(\theta_i)\cos(\phi_i) \end{bmatrix} \\ \sigma^y &= \begin{bmatrix} \sin(\theta_i)\sin(\phi_i) & -i\left(\cos^2\left(\frac{\theta_i}{2}\right) + \sin^2\left(\frac{\theta_i}{2}\right) e^{-i2\phi_i} \right) \\ i\left(\cos^2\left(\frac{\theta_i}{2}\right) + \sin^2\left(\frac{\theta_i}{2}\right) e^{i2\phi_i} \right) & -\sin(\theta_i)\sin(\phi_i) \end{bmatrix} \\ \sigma^z &= \begin{bmatrix} \cos(\theta_i) & -\sin(\theta_i) e^{-i\phi_i} \\ -\sin(\theta_i) e^{i\phi_i} & -\cos(\theta_i) \end{bmatrix} \end{aligned} \tag{2.46}$$

using Eq.(2.46) in Kondo Hamiltonian Eq.(2.2) we get,

$$H_{Kondo} = -\frac{J_K}{2}\sum_i \begin{bmatrix} d_{ip}^\dagger & d_{ia}^\dagger \end{bmatrix} \begin{bmatrix} h_{kondo}^{pp} & h_{kondo}^{pa} \\ h_{kondo}^{pa} & h_{kondo}^{aa} \end{bmatrix} \begin{bmatrix} d_{ip} \\ d_{ia} \end{bmatrix} \tag{2.47}$$

where,

$$\begin{aligned} h_{kondo}^{pp} &= S_i^x[\sin(\theta_i)\cos(\phi_i)] + S_i^y[\sin(\theta_i)\sin(\phi_i)] + S_i^z[\cos(\theta_i)] \\ &= (S_i^x)^2 + (S_i^y)^2 + (S_i^z)^2 = |\mathbf{S}_i| = 1, \end{aligned} \tag{2.48}$$

$$\begin{aligned} h_{kondo}^{pa} &= S_i^x\left[\cos^2\left(\frac{\theta_i}{2}\right) - \sin^2\left(\frac{\theta_i}{2}\right)e^{-i2\phi_i}\right] + S_i^y\left[-i\left(\cos^2\left(\frac{\theta_i}{2}\right) + \sin^2\left(\frac{\theta_i}{2}\right)e^{-i2\phi_i}\right)\right] + S_i^z\left[-\sin(\theta_i)e^{-i\phi_i}\right] \\ &= \sin(\theta_i)\cos(\phi_i)\cos^2\left(\frac{\theta_i}{2}\right) - \sin(\theta_i)\cos(\phi_i)\sin^2\left(\frac{\theta_i}{2}\right)e^{-i2\phi_i} - i\sin(\theta_i)\sin(\phi_i)\cos^2\left(\frac{\theta_i}{2}\right) \\ &\quad -i\sin(\theta_i)\sin(\phi_i)\sin^2\left(\frac{\theta_i}{2}\right)e^{-i2\phi_i} - \sin(\theta_i)\cos(\theta_i)e^{-i\phi_i} \\ &= -\sin(\theta_i)\sin^2\left(\frac{\theta_i}{2}\right)e^{-i\phi_i} + \sin(\theta_i)\cos^2\left(\frac{\theta_i}{2}\right)e^{-i\phi_i} - \sin(\theta_i)\cos(\theta_i)e^{-i\phi_i} \\ &= \sin(\theta_i)e^{-i\phi_i}\left(\cos^2\left(\frac{\theta_i}{2}\right) - \sin^2\left(\frac{\theta_i}{2}\right)\right) - \sin(\theta_i)\cos(\theta_i)e^{-i\phi_i} \\ &= \sin(\theta_i)\cos(\theta_i)e^{-i\phi_i} - \sin(\theta_i)\cos(\theta_i)e^{-i\phi_i} = 0, \end{aligned} \tag{2.49}$$

$$h_{kondo}^{ap} = (h_{kondo}^{pa})^* = 0, \tag{2.50}$$

$$\begin{aligned} h_{kondo}^{aa} &= -S_i^x[\sin(\theta_i)\cos(\phi_i)] - S_i^y[\sin(\theta_i)\sin(\phi_i)] - S_i^z[\cos(\theta_i)] \\ &= -[(S_i^x)^2 + (S_i^y)^2 + (S_i^z)^2] = -|\mathbf{S}_i| = -1. \end{aligned} \tag{2.51}$$

Kondo term of the Hamiltonian in rotated reference frame reduces to,

$$\begin{aligned} H_{Kondo} &= -\frac{J_K}{2}\sum_i \begin{bmatrix} d_{ip}^\dagger & d_{ia}^\dagger \end{bmatrix} \begin{bmatrix} 1 & 0 \\ 0 & -1 \end{bmatrix} \begin{bmatrix} d_{ip} \\ d_{ia} \end{bmatrix} \\ &= -\frac{J_K}{2}\sum_i d_{ip}^\dagger d_{ip} - d_{ia}^\dagger d_{ia}. \end{aligned} \tag{2.52}$$

We can see here that in the rotated frame of reference the Kondo term just contains the diagonal elements as the itinerant electrons tend to align parallel or antiparallel to the direction of localized spins. However, this simplification in the Kondo coupling term came at the cost of complicated hopping and SOC terms as described above.

2.4 Rashba Dresselhaus Double Exchange Model

The advantage of transforming the Hamiltonian Eq.(2.15) in new operators which align electron spin parallel or antiparallel to the localized moments is that the coupling term now contains just the diagonal terms in the Hamiltonian matrix, whereas the angular dependencies of the spins are incorporated in hopping amplitudes.

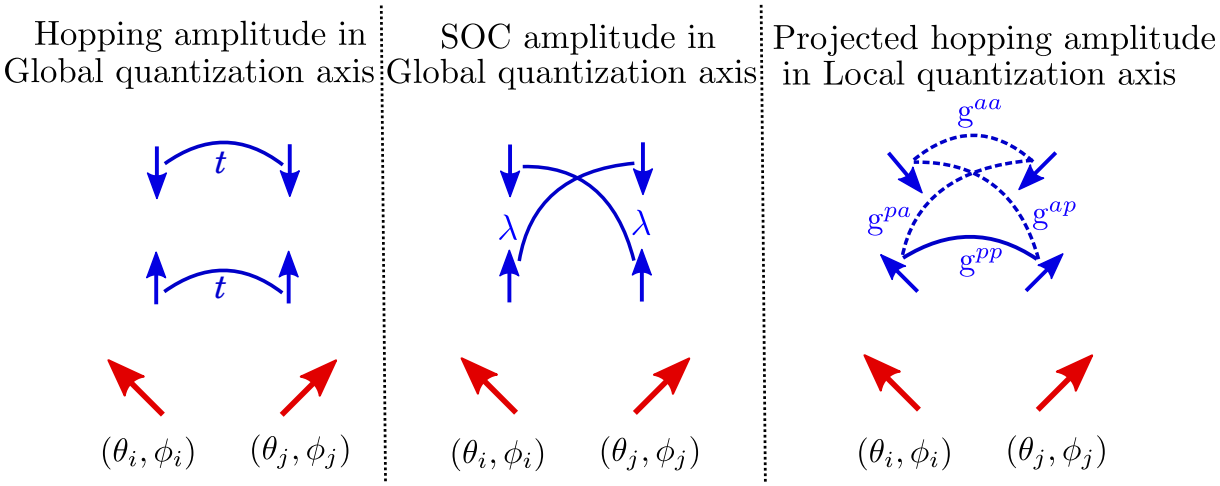

Figure 2.3 Schematic diagram showing itinerant electrons in global quantization and local quantization axis frame of reference.

In the double exchange ($J_K \to \infty$) limit, the bare energy band splits into two sub-bands of spins parallel and antiparallel to the localized moments at each site. Since antiparallel orientations are strongly suppressed for large J_K, the low energy physics is determined by effectively spinless fermions with the spin quantization axis parallel to the local moments (see Fig. 2.3). Projecting onto the parallel subspace, we obtain the modified hopping and SOC amplitudes :

$$t_{ij}(\gamma) = -t\left[\cos\left(\frac{\theta_i}{2}\right)\cos\left(\frac{\theta_j}{2}\right)+\sin\left(\frac{\theta_i}{2}\right)\sin\left(\frac{\theta_j}{2}\right)e^{-\mathrm{i}(\phi_i-\phi_j)}\right], \tag{2.53}$$

$$\lambda^R_{ij}(x) = \lambda_R\left[\sin\left(\frac{\theta_i}{2}\right)\cos\left(\frac{\theta_j}{2}\right)e^{-\mathrm{i}\phi_i}-\cos\left(\frac{\theta_i}{2}\right)\sin\left(\frac{\theta_j}{2}\right)e^{\mathrm{i}\phi_j}\right], \tag{2.54}$$

$$\lambda^R_{ij}(y) = \mathrm{i}\lambda_R\left[\cos\left(\frac{\theta_i}{2}\right)\sin\left(\frac{\theta_j}{2}\right)e^{\mathrm{i}\phi_j}+\sin\left(\frac{\theta_i}{2}\right)\cos\left(\frac{\theta_j}{2}\right)e^{-\mathrm{i}\phi_i}\right], \tag{2.55}$$

$$\lambda_{ij}^{D}(x) = i\lambda_D\Big[\cos\Big(\frac{\theta_i}{2}\Big)\sin\Big(\frac{\theta_j}{2}\Big)e^{i\phi_j}+\sin\Big(\frac{\theta_i}{2}\Big)\cos\Big(\frac{\theta_j}{2}\Big)e^{-i\phi_i}\Big], \tag{2.56}$$

$$\lambda_{ij}^{D}(y) = \lambda_D\Big[\sin\Big(\frac{\theta_i}{2}\Big)\cos\Big(\frac{\theta_j}{2}\Big)e^{-i\phi_i}-\cos\Big(\frac{\theta_i}{2}\Big)\sin\Big(\frac{\theta_j}{2}\Big)e^{i\phi_j}\Big]. \tag{2.57}$$

So, we describe the Rashba Dresselhaus Double Exchange Model by,

$$H_{RDDE} = \sum_{\langle ij\rangle,\gamma}[g_{ij}^{\gamma}d_{ip}^{\dagger}d_{jp}+H.c], \tag{2.58}$$

where,

$$g_{ij}^{\gamma} = t_{ij}(\gamma)+\lambda_{ij}^{R}(\gamma)+\lambda_{ij}^{D}(\gamma) \tag{2.59}$$

is the projected hopping and site $j = i+\gamma$ is the nn of site i along spatial direction $\gamma \in \{x,y\}$.

2.5 Effective Spin Model

In this section we derive an effective spin hamiltonian from Rashba Dresselhaus Double Exchange Model. Using Eq.(2.53) to Eq.(2.57) in Eq.(2.59), we can write the real and imaginary parts of g_{ij}^{γ} as:

$$\begin{aligned}\mathrm{Re}(g_{ij}^{x}) = & -t\left[\cos\left(\frac{\theta_i}{2}\right)\cos\left(\frac{\theta_j}{2}\right)+\sin\left(\frac{\theta_i}{2}\right)\sin\left(\frac{\theta_j}{2}\right)\cos(\phi_i-\phi_j)\right] \\ & +\lambda_R\left[\sin\left(\frac{\theta_i}{2}\right)\cos\left(\frac{\theta_j}{2}\right)\cos\phi_i-\cos\left(\frac{\theta_i}{2}\right)\sin\left(\frac{\theta_j}{2}\right)\cos\phi_j\right] \\ & -\lambda_D\left[\cos\left(\frac{\theta_i}{2}\right)\sin\left(\frac{\theta_j}{2}\right)\sin\phi_j-\sin\left(\frac{\theta_i}{2}\right)\cos\left(\frac{\theta_j}{2}\right)\sin\phi_i\right],\end{aligned} \tag{2.60}$$

$$\begin{aligned}\mathrm{Im}(g_{ij}^{x}) = & \, t\left[\sin\left(\frac{\theta_i}{2}\right)\sin\left(\frac{\theta_j}{2}\right)\sin(\phi_i-\phi_j)\right]-\lambda_R\left[\sin\left(\frac{\theta_i}{2}\right)\cos\left(\frac{\theta_j}{2}\right)\sin\phi_i+\cos\left(\frac{\theta_i}{2}\right)\sin\left(\frac{\theta_j}{2}\right)\sin\phi_j\right] \\ & +\lambda_D\left[\sin\left(\frac{\theta_i}{2}\right)\cos\left(\frac{\theta_j}{2}\right)\cos\phi_i+\cos\left(\frac{\theta_i}{2}\right)\sin\left(\frac{\theta_j}{2}\right)\cos\phi_j\right],\end{aligned}$$

$$\begin{aligned}\mathrm{Re}(g_{ij}^{y}) = & -t\left[\cos\left(\frac{\theta_i}{2}\right)\cos\left(\frac{\theta_j}{2}\right)+\sin\left(\frac{\theta_i}{2}\right)\sin\left(\frac{\theta_j}{2}\right)\cos(\phi_i-\phi_j)\right] \\ & -\lambda_R\left[\cos\left(\frac{\theta_i}{2}\right)\sin\left(\frac{\theta_j}{2}\right)\sin\phi_j-\sin\left(\frac{\theta_i}{2}\right)\cos\left(\frac{\theta_j}{2}\right)\sin\phi_i\right] \\ & +\lambda_D\left[\sin\left(\frac{\theta_i}{2}\right)\cos\left(\frac{\theta_j}{2}\right)\cos\phi_i-\cos\left(\frac{\theta_i}{2}\right)\sin\left(\frac{\theta_j}{2}\right)\cos\phi_j\right],\end{aligned}$$

$$\begin{aligned}\mathrm{Im}(g_{ij}^{y}) = & \, t\left[\sin\left(\frac{\theta_i}{2}\right)\sin\left(\frac{\theta_j}{2}\right)\sin(\phi_i-\phi_j)\right]+\lambda_R\left[\sin\left(\frac{\theta_i}{2}\right)\cos\left(\frac{\theta_j}{2}\right)\cos\phi_i+\cos\left(\frac{\theta_i}{2}\right)\sin\left(\frac{\theta_j}{2}\right)\cos\phi_j\right] \\ & -\lambda_D\left[\sin\left(\frac{\theta_i}{2}\right)\cos\left(\frac{\theta_j}{2}\right)\sin\phi_i+\cos\left(\frac{\theta_i}{2}\right)\sin\left(\frac{\theta_j}{2}\right)\sin\phi_j\right].\end{aligned}$$

Writing g_{ij}^{γ} in polar form, $g_{ij}^{\gamma} = f_{ij}^{\gamma}e^{ih_{ij}^{\gamma}}$, such that

$$\begin{aligned} f_{ij}^{x} &= \{(\mathrm{Re}(g_{ij}^{x}))^2+(\mathrm{Im}(g_{ij}^{x}))^2\}^{1/2}, \\ f_{ij}^{y} &= \{(\mathrm{Re}(g_{ij}^{y}))^2+(\mathrm{Im}(g_{ij}^{y}))^2\}^{1/2} \end{aligned}$$

Using Eq.(2.60) and simplifying, we obtain the following closed form expressions for f_{ij}^{x} and f_{ij}^{y} :

$$f_{ij}^{x} = \Big\{ \frac{1}{2}[t^2(1+S_i^xS_j^x+S_i^yS_j^y+S_i^zS_j^z)+\lambda_R^2(1-S_i^xS_j^x+S_i^yS_j^y-S_i^zS_j^z) \\ -2t\lambda_R(S_i^xS_j^z-S_i^zS_j^x)+\lambda_D^2(1+S_i^xS_j^x-S_i^yS_j^y-S_i^zS_j^z)+2t\lambda_D(S_i^zS_j^y-S_i^yS_j^z)] \Big\}^{1/2}$$

$$= \Big\{ \frac{1}{2}[t^2(1+\mathbf{S}_i\cdot\mathbf{S}_j)+\lambda_R^2(1-\mathbf{S}_i\cdot\mathbf{S}_j+2S_i^yS_j^y)+2t\lambda_R\hat{\mathbf{y}}\cdot(\mathbf{S}_i\times\mathbf{S}_j) \\ +\lambda_D^2(1-\mathbf{S}_i\cdot\mathbf{S}_j+2S_i^xS_j^x)-2t\lambda_D\hat{\mathbf{x}}\cdot(\mathbf{S}_i\times\mathbf{S}_j)] \Big\}^{1/2} \quad (2.61)$$

$$f_{ij}^{y} = \Big\{ \frac{1}{2}[t^2(1+S_i^xS_j^x+S_i^yS_j^y+S_i^zS_j^z)+\lambda_R^2(1+S_i^xS_j^x-S_i^yS_j^y-S_i^zS_j^z) \\ +2t\lambda_R(S_i^zS_j^y-S_i^yS_j^z)+\lambda_D^2(1-S_i^xS_j^x+S_i^yS_j^y-S_i^zS_j^z)-2t\lambda_D(S_i^xS_j^z-S_i^zS_j^x)] \Big\}^{1/2}$$

$$= \Big\{ \frac{1}{2}[t^2(1+\mathbf{S}_i\cdot\mathbf{S}_j)+\lambda_R^2(1-\mathbf{S}_i\cdot\mathbf{S}_j+2S_i^xS_j^x)-2t\lambda_R\hat{\mathbf{x}}\cdot(\mathbf{S}_i\times\mathbf{S}_j) \\ +\lambda_D^2(1-\mathbf{S}_i\cdot\mathbf{S}_j+2S_i^yS_j^y)+2t\lambda_D\hat{\mathbf{y}}\cdot(\mathbf{S}_i\times\mathbf{S}_j)] \Big\}^{1/2} \quad (2.62)$$

The phase angles, h_{ij}^{γ}, are easily obtained via,

$$h_{ij}^{\gamma} = \arctan\left(\frac{\mathrm{Im}(g_{ij}^{\gamma})}{\mathrm{Re}(g_{ij}^{\gamma})}\right), \quad (2.63)$$

The ground state expectation values of the Hamiltonian Eq. (2.58) is identical to the expression, $-\sum_{\langle ij\rangle,\gamma} D_{ij}^{\gamma} f_{ij}^{\gamma}$, where $D_{ij}^{\gamma} = \langle [e^{\mathrm{i}h_{ij}^{\gamma}} d_{ip}^{\dagger} d_{jp} + \mathrm{H.}c.] \rangle_{gs}$. Following the strategy used in double exchange models[4], we promote the above expression to a spin Hamiltonian,

$$H_{\mathrm{S}} = -\sum_{\langle ij\rangle,\gamma} D_{ij}^{\gamma} f_{ij}^{\gamma}. \quad (2.64)$$

We emphasize that, by construction, the magnetic ground states of H_{S} Eq. (2.64) and

H_{RDDE} Eq. (2.58) are identical. We also note that an equality of energy between ground states of H_{S} Eq. (2.64) and H_{RDDE} Eq. (2.58) exists only if D_{ij}^{γ} are allowed to be inhomogeneous. A model with constant coupling parameter is an ad hoc approximation, unless a consistency check is carried out to show that the ground state supports $D_{ij}^{\gamma} \equiv D_0$.

2.6 Kubo-Greenwood Formalism

Many experiments in condensed matter physics measure the liner response to an external perturbation. Kubo formulas are the correlation function that describes the linear response[5]. This formation was first proposed by Green (1952,1954) for transport in liquids. Kubo (1957,1959) first derived the equations for electrical conductivity in solids. We use the standard Kubo formalism for the computation of the transport properties of any given non-interacting Hamiltonian. A brief theory of the formalism is presented here:

In electrical conduction, a time-dependent external electric field,

$$E(t) = E_o \exp(-\imath\omega t) \tag{2.65}$$

is applied. In linear response, the induced current is proportional to the applied electric field. $\sigma(\omega)$ is the response function

$$\sigma(\omega) = \frac{\hbar}{N}\sum_{m}\sum_{n\neq m}\frac{f(E_m)-f(E_n)}{E_m-E_n}|\langle m|J_\gamma|n\rangle|^2\delta(|E_m-E_n|-\hbar\omega)) \tag{2.66}$$

where, E_m and E_n are eigenvalues corresponding to the eigenstates $|m\rangle$ and $|n\rangle$, $f(E_m) = 1/1+\exp(\frac{E_m-\mu_o}{kT})$ is Fermi distribution function and J_γ is current density opperator along γ direction in tight binding model is given by,

$$J_\gamma = -\mathrm{i}t\sum_{i,j}(n_\gamma.\delta_{\mathbf{ij}})(c_j^\dagger c_i - c_i^\dagger c_j) \tag{2.67}$$

where, n_γ is the unit vector in γ direction whereas δ_{ij} is vector from i to j site. In square lattice for current density opperator along x direction, $n_x\cdot\delta_{ij}=1$ and $n_x\cdot\delta_{ij}=0$. So, Longitudinal current density operator is,

$$J_x = -\mathrm{i}t\sum_{i,j}(c_j^\dagger c_i - c_i^\dagger c_j) \tag{2.68}$$

since, eigen sates can be written in site basis,

$$|m\rangle = \sum_i z(i,m)|i\rangle \tag{2.69}$$

so,the matrix elements of J_x in eigen basis of H can be written as,

$$\langle m|J_x|n\rangle = -\mathrm{i}t\sum_{i,j} z^*(j,m)z(i,n) - z^*(i,m)z(j,n) \tag{2.70}$$

The general expression for longitudinal and transverse d.c electrical conductivities i.e for $\omega \to 0$ at $T = 0$ are given by[6],

$$\sigma_{xx}(E) = \frac{\hbar}{N}\sum_m \sum_{n\neq m} \Big(\frac{f(E_m) - f(E_n)}{E_m - E_n}\Big) \frac{\Gamma}{(E_m - E_n)^2 + \Gamma^2} |\langle m|J_x|n\rangle|^2 \tag{2.71}$$

$$\sigma_{xy}(E) = \frac{\mathrm{i}\hbar}{N}\sum_m \sum_{n\neq m} (f(E_m) - f(E_n)) \frac{\langle m|J_x|n\rangle\langle n|J_y|m\rangle}{(E_m - E_n)^2 + \Gamma^2} \tag{2.72}$$

Γ is a positive infinitesimal Lorentzian broadening. Resistivities are obtained by using,

$$\rho_{xx} = \frac{\sigma_{xx}}{\sigma_{xx}^2 + \sigma_{xy}^2}, \tag{2.73}$$

$$\rho_{xy} = \frac{\sigma_{xy}}{\sigma_{xx}^2 + \sigma_{xy}^2}. \tag{2.74}$$

2.6.1 Current density operators

Here we derive the current density operators (J_γ) for Rashba Double Exchange Model on square lattice. The current operator is defined as $\boldsymbol{J} = \frac{\mathrm{i}e}{\hbar}[H, \boldsymbol{r}]$ that takes the following form:

$$J = \frac{\mathrm{i}e}{\hbar}[H, \hat{n}_i] \tag{2.75}$$

where, $\hat{n}_i = c_i^\dagger c_i$ is number operator. We use following properties of anticommutators of fermionic operators:

$$\{c_{i\sigma}^\dagger, c_{j\sigma}^\dagger\} = \{c_{i\sigma}, c_{j\sigma}\} = 0 \tag{2.76}$$

$$\{c^{\dagger}_{i\sigma}, c_{j\sigma'}\} = \delta_{ij}\delta_{\sigma\sigma'} \tag{2.77}$$

to get,

$$[c_{i\sigma}, \hat{n}_{i\sigma}] = c_{i\sigma} \tag{2.78}$$

$$[c^{\dagger}_{i\sigma}, \hat{n}_{i\sigma}] = -c^{\dagger}_{i\sigma} \tag{2.79}$$

$$[c_{i\sigma}, \hat{n}_{i\sigma'}] = [c^{\dagger}_{i\sigma}, \hat{n}_{i\sigma'}] = 0 \tag{2.80}$$

$$[c_{i\sigma}, \hat{n}_{j\sigma}] = [c^{\dagger}_{i\sigma}, \hat{n}_{j\sigma}] = 0 \tag{2.81}$$

The tight binding (TB) and Rashba spin orbit (SO) coupling contributions of current operator along $\gamma \in \{x, y\}$ directions such that site $j = i + \gamma$ is the nn of site i are,

TB **along** γ

$$\begin{aligned} J^{\mathrm{TB}}_{\gamma} &= \frac{-\mathrm{i}et}{\hbar} \sum_{\langle ij\rangle,\sigma} [(c^{\dagger}_{i\sigma} c_{j\sigma} + c^{\dagger}_{j\sigma} c_{i\sigma}), \hat{n}_{i\sigma}] \\ &= \frac{-\mathrm{i}et}{\hbar} \sum_{\langle ij\rangle,\sigma} [c^{\dagger}_{i\sigma} c_{j\sigma}, \hat{n}_{i\sigma}] + [c^{\dagger}_{j\sigma} c_{i\sigma}, \hat{n}_{i\sigma}] \\ &= \frac{-\mathrm{i}et}{\hbar} \sum_{\langle ij\rangle,\sigma} c^{\dagger}_{i\sigma}[c_{j\sigma}, \hat{n}_{i\sigma}] + [c^{\dagger}_{i\sigma}, \hat{n}_{i\sigma}] c_{j\sigma} + c^{\dagger}_{j\sigma}[c_{i\sigma}, \hat{n}_{i\sigma}] + [c^{\dagger}_{j\sigma}, \hat{n}_{i\sigma}] c_{i\sigma} \end{aligned} \tag{2.82}$$

using Eq. (2.78) - Eq. (2.81) in Eq. (2.82) we get,

$$J^{\mathrm{TB}}_{\gamma} = \frac{-\mathrm{i}et}{\hbar} \sum_{\langle ij\rangle,\sigma} (c^{\dagger}_{j\sigma} c_{i\sigma} - H.c) \tag{2.83}$$

SO **along x**

$$\begin{aligned} J^{\mathrm{SO}}_{x} &= \frac{\mathrm{i}e}{\hbar}[H_x, \hat{n}_i] = [H_x, \hat{n}_{i\uparrow} + \hat{n}_{i\downarrow}] \\ &= \frac{\mathrm{i}e\lambda_R}{\hbar} \sum_{\langle ij\rangle} [(c^{\dagger}_{i\downarrow} c_{j\uparrow} - c^{\dagger}_{i\uparrow} c_{j\downarrow} + c^{\dagger}_{j\uparrow} c_{i\downarrow} - c^{\dagger}_{j\downarrow} c_{i\uparrow}), \hat{n}_{i\uparrow} + \hat{n}_{i\downarrow}] \end{aligned} \tag{2.84}$$

simplifying Eq. (2.84) we get,

$$J_x^{SO} = \frac{ie\lambda_R}{\hbar}\sum_{\langle ij\rangle}((c_{j\uparrow}^{\dagger}c_{i\downarrow} - c_{j\downarrow}^{\dagger}c_{i\uparrow}) - H.c) \tag{2.85}$$

SO **along y**

$$\begin{aligned} J_y^{SO} &= \frac{ie}{\hbar}[H_y, \hat{n}_i] = [H_y, \hat{n}_{i\uparrow} + \hat{n}_{i\downarrow}] \\ &= \frac{ie\lambda_R}{\hbar}\sum_{\langle ij\rangle}[(ic_{i\downarrow}^{\dagger}c_{j\uparrow} + ic_{i\uparrow}^{\dagger}c_{j\downarrow} - ic_{j\uparrow}^{\dagger}c_{i\downarrow} - ic_{j\downarrow}^{\dagger}c_{i\uparrow}), \hat{n}_{i\uparrow} + \hat{n}_{i\downarrow}] \end{aligned} \tag{2.86}$$

simplifying Eq. (2.86) we get,

$$J_y^{SO} = \frac{ie\lambda_R}{\hbar}\sum_{\langle ij\rangle}(-i(c_{j\uparrow}^{\dagger}c_{i\downarrow} + c_{j\downarrow}^{\dagger}c_{i\uparrow}) - H.c) \tag{2.87}$$

Transforming Eq. (2.83), (2.85) and (2.87) using unitary transformations defined in Eq. (2.19) and projecting onto the parallel subspace in double exchange limit (the same way as we transformed the Hamiltonian), we get the current operator for Rashba Dresselhaus double exchange model as,

$$J_\gamma = \frac{ie}{\hbar}\sum_{\langle ij\rangle,\gamma}[g_{ij}^{\gamma}d_{ip}^{\dagger}d_{jp} - H.c], \tag{2.88}$$

where, g_{ij}^{γ} is given by Eq. (2.59).

2.7 Methods

In the present thesis, we study the spin-orbit coupled magnetic metallic systems. Because of this interesting interplay of magnetism and itinerant charge carriers, we expect exotic spin textures as ground states. To understand the essential physics behind such exotic magnetic orderings and related phenomena, we study the models introduced in this chapter. In order to study classical spin Hamiltonians, we employ Markov chain classical Monte Carlo technique. The standard Metropolis algorithm is used for the importance sampling of spin configurations at finite temperatures. For semi-classical spin Hamiltonians, we rely on hybrid monte Carlo method. For analysis of the topological aspects of the studied Hamiltonians, we perform Bott index calculations. In the following, we elaborate on these methods, which have been used to obtain the results reported in

this thesis.

2.7.1 Classical Monte Carlo

Monte Carlo methods are a broad class of computational algorithms that rely on repeated random sampling to obtain numerical results. The advantage of this technique is that we can estimate the physical quantities accurately by using only sample quite a small fraction of the states of the system. Monte Carlo technique is used to solve quantitative problems in the area of physics and in other areas of science, engineering, and finance. This technique was implemented to study the neutron transport[7], chemical kinetics[8]. Monte Carlo method also plays a key role in designing and analyzing materials such as organic solar cells[9], organic LEDs[10], etc. This method has been successfully applied in statistical physics, probability theory, mathematical optimization and computer science[11]. In condensed matter physics, it has proved to be a powerful method to study Hamiltonians whose complexity does not allow for analytical treatment. In magnetic systems, the classical and semi-classical spin models often simulated using Monte Carlo methods. The Quantum version of the method can be used to study quantum electronic Hamiltonians. However, it suffers from the infamous "sign problem" for some fermionic models, and is limited to small lattices. The classical Monte Carlo, on the other hand, can be used to simulate very large lattices and hence provides results close to thermodynamic limit. Another advantage of all Monte-Carlo methods is that they allow access to local physical quantities, and can provide a deeper understanding of complex ordering.

The core idea in Monte Carlo is to simulate the random thermal fluctuation of the system from state to state over the course of an experiment. In the Monte Carlo simulation of a thermal system, one is mainly interested in the calculation of the expectation value $\langle M \rangle$ of some observable quantity ' M ', such as the internal energy, susceptibility, or the magnetization in a magnetic model. This is done by averaging ' M ' over all the microstates of the canonical ensemble weighted with the Boltzmann probability.

$$\langle M \rangle = \frac{\sum_\mu M_\mu e^{-\beta E_\mu}}{\sum_\mu e^{-\beta E_\mu}} \tag{2.89}$$

where, E_μ is the energy of state μ. Since it is impossible to calculate $\langle M \rangle$ by averaging over all the microstates because of the large number of microstates which increases rapidly with system size. So we restrict ourselves to only those states which are statistically most relevant. The technique for picking out the important states from the very large number of possibilities is called importance sampling. This is done by choosing the states with Boltzmann probability $P_\mu = Z^{-1} e^{-\beta E_\mu}$ where ' Z ' is partition function of

the system.

Monte Carlo make use of Markov process repeatedly to generate a Markov chain of states. Starting with a state μ, we generate a new state ν with some fixed transition probability $P(\mu \to \nu)$, and then we feed that state to generate another state and so on. The transition probabilities must satisfy the constraint:

$$\sum_{\nu} P(\mu \to \nu) \quad = \quad 1 \tag{2.90}$$

This process when run for long enough starting from any state of the system eventually produces a succession of states which appear with probabilities given by the Boltzmann distribution. There are two requirements for Markov process. It must obey condition of ergodicity and the condition of detailed balance. Condition of ergodicity ensures the possibility for our Markov process to reach any state of the system from any other state. Condition of detailed balance is expressed mathematically as:

$$p_{\mu} P(\mu \to \nu) \quad = \quad p_{\nu} P(\nu \to \mu) \tag{2.91}$$

The left hand side of the equation, is the product of probability of being in a state μ and the probability of making a transition from that state to another state ν. In other words, it is the overall rate at which transitions from μ to ν happen in our system. The right hand side is the overall rate for the reverse transition. The condition of detailed balance tells us that on average the system should go from μ to ν just as often as it goes from ν to μ. We can choose any probability distribution p_{μ} of states generated by our Markov process such that it satisfies Eq. (2.91). Since we want the equilibrium distribution to be the Boltzmann distribution, the detailed balance equation becomes:

$$\frac{P(\mu \to \nu)}{P(\nu \to \mu)} \quad = \quad \frac{p_{\nu}}{p_{\mu}} = e^{-\beta(E_{\nu} - E_{\mu})} \tag{2.92}$$

After we choose the transition probabilities we use Metropolis Algorithm proposed by Metropolis and his co-workers in 1953. This algorithm chooses a set of selection probabilities $g(\mu \to \nu)$ for each possible transition from state $\mu \to \nu$. Then chooses a set of acceptance probabilities $A(\mu \to \nu)$ such that the condition of detailed balance is satisfied. The algorithm works by repeatedly choosing a new state ν, and then accept or reject it at random with chosen acceptance probability. We get,

$$P(\mu \to \nu) \quad = \quad g(\mu \to \nu) A(\mu \to \nu) \tag{2.93}$$

If we use classical monte carlo for a N classical spin system with single-spin-flip dynam-

ics. There are N different spins that we can flip, and hence N possible states ν which can be reached from a given state μ. Thus the selection probabilities,

$$g(\mu \to \nu) \quad = \quad \frac{1}{N} \tag{2.94}$$

Using Eq. (2.93) and Eq. (2.94) in Eq. (2.92) we get,

$$\frac{P(\mu \to \nu)}{P(\nu \to \mu)} \quad = \quad \frac{A(\mu \to \nu)}{A(\nu \to \mu)} = e^{-\beta(E_\nu - E_\mu)} \tag{2.95}$$

The chances of making any move for which $\Delta E > 0$ are very small, it means that an algorithm using the acceptance ratio would be extremely slow, spending most of its time rejecting moves and not flipping any spins at all. The way to maximize the acceptance ratios is, suppose that if $E_\mu < E_\nu$. Then the larger of the two acceptance ratios is $A(\nu \to \mu)$, so we set that equal to 1. Then to satisfy Eq. (2.95) $A(\mu \to \nu)$ must be $e^{-\beta(E_\nu - E_\mu)}$. Thus for the optimal algorithm[12,13],

$$A(\mu \to \nu) = \begin{cases} e^{-\beta(E_\nu - E_\mu)} & \text{If} \quad E_\nu - E_\mu > 0 \\ 1 \quad \text{otherwise} \end{cases} \tag{2.96}$$

2.7.2 Steps to implement Metropolis Algorithm

For the classical spin Hamiltonian Eq. (2.64), we make use of conventional Classical Monte Carlo simulation technique. In this thesis work we have investigated the Hamiltonians by following two protocols. In the field cooled protocol, the temperature is lowered in the presence of a finite external field. At each temperature point we implement Metropolis algorithm in following steps:

• *An initial completely random configuration of spins with polar (θ_i) and azimuthal (ϕ_i) angles defined at each site i is taken on the given lattice at temperature much larger than other energy scales in the model. Energy of this configuration is then calculated. (θ, ϕ) are picked from a set of uniformly distributed discrete points on the surface of a unit sphere.*

• *A new configuration is then generated by selecting a lattice site and changing $\theta_i \to \theta_i'$, $\phi_i \to \phi_i'$ at that site and energy is calculated.*

• *Difference in energy of old and new configurations i.e $\Delta E = E(\theta_i', \phi_i') - E(\theta_i, \phi_i)$ is evaluated*

• *If $\Delta E \leq 0$ then the move is accepted, since in this case $A(\mu \to \nu) = 1$.*

• *If* $\Delta E > 0$ *then* $A(\mu \to \nu) = e^{-\beta(E_\nu - E_\mu)}$ *is calculated and a random number* $r \in (0,1)$ *is chosen. If* $r < A(\mu \to \nu)$ *the move is accepted, else rejected.*

• *The above steps are repeated until each site is visited once for attempting an update. This completes one Monte Carlo update over the lattice.*

• *Approximately* 10^6 *such updates are performed at each temperature for the system to reach equilibrium.*

• *Physical quantities such as, various order parameters, average energy etc., are then computed by averaging over next* 10^6 *updates.*

• *The temperature is then reduced and the above procedure is repeated with the last configuration of the old temperature serving as the first configuration of the new temperature.*

In the zero field cooled protocol, the simulations begin in the paramagnetic phase with $h_z = 0$ and temperature is then lowered in discrete steps. To calculate the field dependence at low temperatures, which is the main focus of the study, the external field h_z is increased in discrete steps. For detailed exploration of parameter space we use 60×60 lattice, and the stability of results is ensured by simulating sizes up to 200×200 for selected cases.

2.7.3 Hybrid Monte Carlo

Hamiltonian Eq. (2.15) and Eq. (2.58), belongs to a class of models with classical degrees of freedom coupled to electrons. The Hybrid Monte Carlo simulation, an extension of Classical Monte Carlo simulation is the most reliable and numerically exact approach for the study of such Hamiltonians. In this approach, the classical variables are updated according to Metropolis algorithm, and we can treat classical spins as a 'fixed' background when solving the electron problem. Unlike classical variables for solving electron problem, one has to perform exact diagonalization of the quantum hamiltonian. For a lattice with N sites, the resulting Hamiltonian matrix is '2N' dimensional, where 2 is because of up and down spin states. One need to diagonalize the full Hamiltonian at each step of the monte carlo. Diagonalization itself is a process which scales as $\mathcal{O}(\mathrm{N}^3)$ and one needs to repeat this N times for a system sweep, so the cost per sweep for this class of model is $\mathcal{O}(\mathrm{N}^4)$, in contrast to the $\mathcal{O}(\mathrm{N})$ cost for the classical spin Hamiltonian Eq. (2.64). Hence simulations are limited to very small lattices ~ 100 sites. To estimate the energy change associated with the spin updated at the choosen site, we don't need to diagonalize the full Hamiltonian, instead we can perform the

exact diagonalization of the fermionic part of Hamiltonian on a smaller cluster centred around the site to be updated. Hence for simulations on the larger lattices without compromising on the accuracy we use Travelling cluster approximation (TCA) method[14, 15]. If we take that cluster of dimension N_c, then the cost of the MC is $\mathcal{O}(NN_c^3)$. This leads to a huge gain and allows us to go up lattices of size 40^2. For the results presented in this thesis, TCA simulations are performed on 24×24 lattice with periodic boundary conditions using an 8×8 cluster with open boundary conditions. A typical schematic is shown in Fig. . While for calculating the system properties, we diagonalize the full system. The 'CHEEVX' subroutine of the LAPACK library is used for the diagonalization of the Hamiltonian. We use $\sim 10^3$ MC steps each for equilibration and averaging at each value of temperature and Zeeman field. Other details are same as in the classical Monte Carlo simulation method.

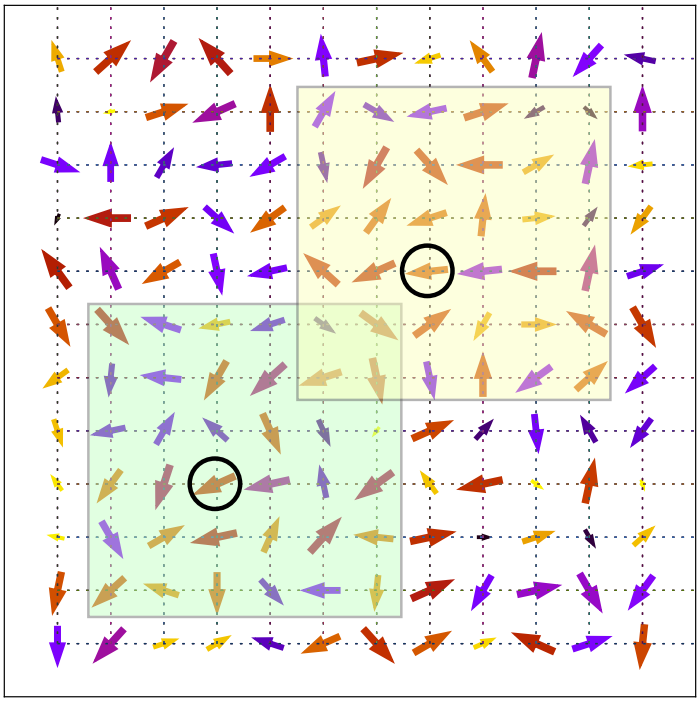

Figure 2.4 Schematic showing the travelling cluster approximation on a square lattice (size 12^2) consists of random spins. The green and the yellow squares are two representative clusters (size 6^2) built around the circled sites which are to be updated.

2.7.4 Bott Index

Loring and Hasting first introduced the concept of Bott index in condensed matter systems[16]. It is a measure of the obstruction to form localized Wannier orbitals from the occupied states[17,18]. Bott index has been handy in successfully describe the approxi-

mate integer quanta of the transverse conductivity of a finite two-dimensional system described by a short-range, spectrally gapped Hamiltonian even in the presence of local disorder[19]. In this thesis, we study the Bott index variation to study the topological aspect of the transverse conductivity in the presence of skyrmion (Chapter 4). The mathematical implementation of Bott index has already been explained in some of the previous studies[20–24]. First, a projector operator is constructed out of all the occupied states below Fermi level.

$$P = \sum_{i}^{Nel} |\psi_i\rangle \langle\psi_i| , \tag{2.97}$$

where, $|\psi_i\rangle$ is the occupied state corresponds to the ith eigenvalue ε_i, and Nel is the number of electrons in the system. The position coordinates (x_i , y_i) of any lattice site i can be mapped into the spherical co-ordinates (θ_i , ϕ_i) on a torus (using periodic boundary condition) where $0 \leq \theta_i < 2\pi$ and $0 \leq \phi_i < 2\pi$. The next step is to calculate the position operators mapped onto the project operator P, given as,

$$\begin{aligned} U &= Pe^{i\Theta}P, \\ V &= Pe^{i\Phi}P, \end{aligned} \tag{2.98}$$

where, Θ and Φ are the diagonal matrices with θ_i and ϕ_i as diagonal elements respectively. The Bott index, which determines the commutativity of the projected position operators U and V[25,26] is given by,

$$B = \frac{1}{2\pi}\mathrm{Im}\Big\{\mathrm{tr}\big[\log(VUV^{\dagger}U^{\dagger})\big]\Big\}, \tag{2.99}$$

The Bott index is demonstrated to be closely related to the Chern number[19], it can be employed as a topological invariant to distinguish between topologically nontrivial from trivial states, and hence is proved to be quite useful in the study of topological Hall effect. This calculation involves diagonalization of complex non-symmetric matrix for which we use the 'CGEES' LAPACK subroutine.

For a better numerical convergence, the product $VUV^{\dagger}U^{\dagger}$ needs to be unitary. Hence, $\det(VUV^{\dagger}U^{\dagger}) = 1$ and the eigenvalues of $\log(VUV^{\dagger}U^{\dagger})$ should be purely imaginary, and the Bott index is a real integer[19]. For improved numerical stability, we perform singular value decomposition (SVD) $M = Z\Sigma W^{\dagger}$ for the projected position operators U and V. Z and W are the unitary matrices where Σ is real diagonal matrix. It can be shown that the "unitary part" $\tilde{M} = ZW^{\dagger}$ is the transformed unitary projected position operators.

Mathematically, the Singular value decomposition is similar to a scaling transformation; hence it does not alter the commutation relation between two operators. Therefore, we can safely state that employing SVD does change anything to the original formalism, but the convergence and numerical stability get effectively improved. For SVD the 'CGESVD' subroutine from LAPACK package has been employed.

Bibliography

[1] M. Gulácsi*, *Advances in physics*, 2004, **53**, 769–937.

[2] Z. Li, L. Covaci and F. Marsiglio, *Physical Review B*, 2012, **85**, 205112.

[3] D. Pekker, S. Mukhopadhyay, N. Trivedi and P. M. Goldbart, *Physical Review B*, 2005, **72**, 075118.

[4] S. Kumar and P. Majumdar, *The European Physical Journal B-Condensed Matter and Complex Systems*, 2005, **46**, 315–324.

[5] G. D. Mahan, *Many-particle physics*, Springer Science & Business Media, 2013.

[6] P. Dutta, S. K. Maiti and S. Karmakar, *Journal of Applied Physics*, 2012, **112**, 044306.

[7] N. Metropolis, *Los Alamos Science*, 1987, **15**, 125–130.

[8] D. T. Gillespie, *Journal of computational physics*, 1976, **22**, 403–434.

[9] O. Stenzel, L. J. A. Koster, R. Thiedmann, S. D. Oosterhout, R. A. Janssen and V. Schmidt, *Advanced Functional Materials*, 2012, **22**, 1236–1244.

[10] A. Dieguez, A. Romano-Rodrıguez, A. Vila and J. Morante, *Journal of Applied Physics*, 2001, **90**, 1550–1557.

[11] D. P. Kroese, T. Brereton, T. Taimre and Z. I. Botev, *Wiley Interdisciplinary Reviews: Computational Statistics*, 2014, **6**, 386–392.

[12] M. Newman and G. Barkema, *Monte carlo methods in statistical physics chapter 1-4*, Oxford University Press: New York, USA, 1999, vol. 24.

[13] K. Binder, D. M. Ceperley, J.-P. Hansen, M. Kalos, D. Landau, D. Levesque, H. Mueller-Krumbhaar, D. Stauffer and J.-J. Weis, *Monte Carlo methods in statistical physics*, Springer Science & Business Media, 2012, vol. 7.

[14] S. Kumar and P. Majumdar, *The European Physical Journal B-Condensed Matter and Complex Systems*, 2006, **50**, 571–579.

[15] A. Mukherjee, N. D. Patel, C. Bishop and E. Dagotto, *Physical Review E*, 2015, **91**, 063303.

[16] T. A. Loring and M. B. Hastings, *EPL (Europhysics Letters)*, 2010, **92**, 67004.

[17] M. B. Hastings and T. A. Loring, *Journal of mathematical physics*, 2010, **51**, 015214.

[18] M. B. Hastings and T. A. Loring, *Annals of Physics*, 2011, **326**, 1699 – 1759.

[19] D. Toniolo, *arXiv preprint arXiv:1708.05912*, 2017.

[20] T. A. Loring, *Annals of Physics*, 2015, **356**, 383 – 416.

[21] A. Agarwala and V. B. Shenoy, *Phys. Rev. Lett.*, 2017, **118**, 236402.

[22] M. A. Bandres, M. C. Rechtsman and M. Segev, *Phys. Rev. X*, 2016, **6**, 011016.

[23] D. Toniolo, *Physical Review B*, 2018, **98**, 235425.

[24] H. Huang and F. Liu, *Phys. Rev. B*, 2018, **98**, 125130.

[25] J. Bellissard, A. van Elst and H. Schulz- Baldes, *Journal of Mathematical Physics*, 1994, **35**, 5373–5451.

[26] R. Exel and T. A. Loring, *Journal of Functional Analysis*, 1991, **95**, 364–376.

3

Study of microscopic magnetic Hamiltonian for exotic spin textures in metals

---

Adapted from the work :

Deepak. S. Kathyat, Arnob Mukherjee, and Sanjeev Kumar

PHYSICAL REVIEW B **102**, 075106 (2020)

3.1 Introduction

Search for magnetic materials supporting unusual spin textures has become an important theme of research in recent years[1–7]. Presence of such textures in insulators and metals holds promise for technological applications[8–10]. In particular, topologically protected magnetic textures such as skyrmions, are considered building blocks of race-track memory devices[11–13]. Presence of such spin textures in metals allows for their control using ultra-low currents. Furthermore, noncoplanar magnetic states in metals are known to dramatically influence the spin-polarized charge transport – a feature that can be utilized in spintronics applications[14–20]. There are various metallic magnets, *e.g.* MnSi, FeGe, Co-Zn-Mn alloys, etc., that support exotic spin textures not only in the ground state but also at higher temperatures[5,21–24]. Similar spin textures are also observed in thin films as well as multilayers involving transition metals[25–29].

The key step towards designing or discovering materials with unconventional spin textures is to understand the physics of minimal microscopic models incorporating essential elementary mechanisms[30–32]. Spin Hamiltonians naturally emerge in insulators as the charge degrees of freedom become inactive and the low energy physics is determined by the spin degrees of freedom. In contrast, spin Hamiltonians in metals are phenomenologically motivated. Exceptions exist in metals that consist of a subsystem of localized magnetic moments interacting with conduction band. The RKKY model is a famous example in this category[33–37]. Explanation of skyrmion-like spin textures relies on the presence of DM interactions[38–42]. While such anisotropic terms have been motivated by invoking the effect of spin-orbit coupling (SOC) in a two-site setting, a derivation on lattice for the metallic case does not exist[30,43].

In this work, we present a closed form expression for a spin Hamiltonian for Rashba coupled double-exchange (DE) magnets. The resulting model consists of anisotropic terms resembling DM and pseudo-dipolar interactions on nearest neighbor (nn) sites with inhomogeneous coupling parameter. After presenting the derivation, we explicitly test the validity of the pure spin model by comparing results against exact diagonalization based simulations on the starting electronic model. The magnetic phase diagram of the spin model is obtained via large-scale Monte Carlo simulations. The model supports, in addition to a ferromagnetic (FM) phase, (i) single-Q (SQ) spiral states, (ii) diagonally-oriented flux (d-Flux) state, (iii) multiple-Q (MQ) states with noncoplanar skyrmion crystal (SkX) patterns, and (iv) a classical spin liquid (CSL) state characterized by diffuse ring patterns in the spin structure factor (SSF). The CSL state shows filamentary domain wall structure of remarkable similarity to the experimental data on thin

films and multilayers of B20 compounds and transition metals[20,26,27]. The spin model introduced here has wide range of applicability as it originates from the FM Kondo lattice model (FKLM) – a generic model for metals with local moments. Some of the well known families of materials where FKLM is realized are, manganites, doped magnetic semiconductors and Heusler compounds[44–51]. The key ingredient in the model is the Rashba SOC, which requires breaking of inversion symmetry. Such inversion symmetry breaking is naturally achieved for the emergent conduction layers at interfaces, or in thin films of magnetic metals[52].

3.2 Derivation of the spin Hamiltonian

Our starting point is the FKLM in the presence of Rashba SOC on a square lattice, described by the Hamiltonian,

$$\begin{aligned} H &= -t\sum_{\langle ij\rangle,\sigma}(c^{\dagger}_{i\sigma}c_{j\sigma}+\text{H.c.})+\lambda\sum_{i}[(c^{\dagger}_{i\downarrow}c_{i+x\uparrow}-c^{\dagger}_{i\uparrow}c_{i+x\downarrow}) \\ &\quad +\mathrm{i}(c^{\dagger}_{i\downarrow}c_{i+y\uparrow}+c^{\dagger}_{i\uparrow}c_{i+y\downarrow})+\text{H.c.}]-J_H\sum_{i}\mathbf{S}_i\cdot\mathbf{s}_i. \end{aligned} \tag{3.1}$$

Here, $c_{i\sigma}(c^{\dagger}_{i\sigma})$ annihilates (creates) an electron at site i with spin σ, $\langle ij\rangle$ implies that i and j are nn sites. λ and J_H denote the strengths of Rashba coupling and ferromagnetic Kondo (or Hund's) coupling, respectively. $\mathbf{s_i}$ is the electronic spin operator at site i, and $\mathbf{S}_i$, with $|\mathbf{S}_i|=1$, denotes the localized spin at that site. We parameterize $t=(1-\alpha)t_0$ and $\lambda=\alpha t_0$ in order to connect the weak and the strong Rashba limits, $\alpha=0$ and $\alpha=1$, respectively. $t_0=1$ sets the reference energy scale.

Note that coupling between localized spins $\mathbf{S}_i$ is mediated via the conduction electrons. In the limit of weak Kondo coupling, this leads to a modified RKKY Hamiltonian which is discussed in a recent work[53]. To clarify the physics of the above Hamiltonian in the $J_H\to\infty$ limit, also known as the DE limit, we rewrite the Hamiltonian in a basis where the spin-quantization axes are site dependent and align with the direction of the local magnetic moment according to the canonical $SU(2)$ transformation,

$$\begin{bmatrix} c_{i\uparrow} \\ c_{i\downarrow} \end{bmatrix} = \begin{bmatrix} \cos(\frac{\theta_i}{2}) & -\sin(\frac{\theta_i}{2})e^{-\mathrm{i}\phi_i} \\ \sin(\frac{\theta_i}{2})e^{\mathrm{i}\phi_i} & \cos(\frac{\theta_i}{2}) \end{bmatrix} \begin{bmatrix} d_{ip} \\ d_{ia} \end{bmatrix}.$$

Here, $d_{ip}(d_{ia})$ annihilates an electron at site i with spin parallel (antiparallel) to the localized spin and θ_i, ϕ_i are the polar and azimuthal angles describing the direction

of the local spin $\mathbf{S}_i$. Since antiparallel orientations are strongly suppressed for large J_H, the low energy physics is determined by effectively spinless fermions with the spin quantization axis parallel to the local moments. Projecting onto the parallel subspace, we obtain the Rashba DE (RDE) Hamiltonian,

$$H_{\rm RDE} = \sum_{\langle ij\rangle,\gamma} [g_{ij}^{\gamma} d_{ip}^{\dagger} d_{jp} + {\rm H.}c.], \tag{3.2}$$

where, $d_{ip}^{\dagger}$ creates an electron at site i with spin parallel to the localized spin. Site $j = i+\gamma$ is the nn of site i along spatial direction $\gamma = x, y$. The projected hopping $g_{ij}^{\gamma} = t_{ij}^{\gamma} + \lambda_{ij}^{\gamma}$ have contributions from the standard hopping integral t and the Rashba coupling λ, and depend on the orientations of the local moments. The two contributions to g_{ij}^{γ} are given by,

$$\begin{aligned}
t_{ij}^{\gamma} &= -t\left[\cos\left(\frac{\theta_i}{2}\right)\cos\left(\frac{\theta_j}{2}\right) + \sin\left(\frac{\theta_i}{2}\right)\sin\left(\frac{\theta_j}{2}\right)e^{-{\rm i}(\phi_i-\phi_j)}\right], \\
\lambda_{ij}^{x} &= \lambda\left[\sin\left(\frac{\theta_i}{2}\right)\cos\left(\frac{\theta_j}{2}\right)e^{-{\rm i}\phi_i} - \cos\left(\frac{\theta_i}{2}\right)\sin\left(\frac{\theta_j}{2}\right)e^{{\rm i}\phi_j}\right], \\
\lambda_{ij}^{y} &= {\rm i}\lambda\left[\sin\left(\frac{\theta_i}{2}\right)\cos\left(\frac{\theta_j}{2}\right)e^{-{\rm i}\phi_i} + \cos\left(\frac{\theta_i}{2}\right)\sin\left(\frac{\theta_j}{2}\right)e^{{\rm i}\phi_j}\right].
\end{aligned} \tag{3.3}$$

We can write the real and imaginary parts of g_{ij}^{γ} as:

$$\begin{aligned}
{\rm Re}(g_{ij}^{x}) = & -t(\cos(\frac{\theta_i}{2})\cos(\frac{\theta_j}{2}) + \sin(\frac{\theta_i}{2})\sin(\frac{\theta_j}{2})\cos(\phi_i-\phi_j)) \\
& + \lambda(\sin(\frac{\theta_i}{2})\cos(\frac{\theta_j}{2})\cos\phi_i - \cos(\frac{\theta_i}{2})\sin(\frac{\theta_j}{2})\cos\phi_j), \\
{\rm Im}(g_{ij}^{x}) = & \, t(\sin(\frac{\theta_i}{2})\sin(\frac{\theta_j}{2})\sin(\phi_i-\phi_j)) - \lambda(\sin(\frac{\theta_i}{2})\cos(\frac{\theta_j}{2})\sin\phi_i + \cos(\frac{\theta_i}{2})\sin(\frac{\theta_j}{2})\sin\phi_j), \\
{\rm Re}(g_{ij}^{y}) = & -t(\cos(\frac{\theta_i}{2})\cos(\frac{\theta_j}{2}) + \sin(\frac{\theta_i}{2})\sin(\frac{\theta_j}{2})\cos(\phi_i-\phi_j)) \\
& - \lambda(\cos(\frac{\theta_i}{2})\sin(\frac{\theta_j}{2})\sin\phi_j - \sin(\frac{\theta_i}{2})\cos(\frac{\theta_j}{2})\sin\phi_i), \\
{\rm Im}(g_{ij}^{y}) = & \, t(\sin(\frac{\theta_i}{2})\sin(\frac{\theta_j}{2})\sin(\phi_i-\phi_j)) + \lambda(\sin(\frac{\theta_i}{2})\cos(\frac{\theta_j}{2})\cos\phi_i + \cos(\frac{\theta_i}{2})\sin(\frac{\theta_j}{2})\cos\phi_j).
\end{aligned} \tag{3.4}$$

Writing g_{ij}^{γ} in the polar form, $g_{ij}^{\gamma} = f_{ij}^{\gamma} e^{{\rm i}h_{ij}^{\gamma}}$, the phase angles, h_{ij}^{γ}, are easily obtained via,

$$h_{ij}^{\gamma} = \arctan\left(\frac{{\rm Im}(g_{ij}^{\gamma})}{{\rm Re}(g_{ij}^{\gamma})}\right), \tag{3.5}$$

and closed form expressions for f_{ij}^{x} and f_{ij}^{y} :

$$\begin{aligned} f_{ij}^{x} &= \sqrt{\frac{1}{2}[t^2(1+S_i^xS_j^x+S_i^yS_j^y+S_i^zS_j^z)+\lambda^2(1-S_i^xS_j^x+S_i^yS_j^y-S_i^zS_j^z)-2t\lambda(S_i^xS_j^z-S_i^zS_j^x)]} \\ &= \sqrt{\frac{1}{2}[t^2(1+\mathbf{S}_i\cdot\mathbf{S}_j)+\lambda^2(1-\mathbf{S}_i\cdot\mathbf{S}_j+2S_i^yS_j^y)+2t\lambda\hat{\mathbf{y}}\cdot(\mathbf{S}_i\times\mathbf{S}_j)]}, \end{aligned}$$

$$\begin{aligned} f_{ij}^{y} &= \sqrt{\frac{1}{2}[t^2(1+S_i^xS_j^x+S_i^yS_j^y+S_i^zS_j^z)+\lambda^2(1+S_i^xS_j^x-S_i^yS_j^y-S_i^zS_j^z)+2t\lambda(S_i^zS_j^y-S_i^yS_j^z)]} \\ &= \sqrt{\frac{1}{2}[t^2(1+\mathbf{S}_i\cdot\mathbf{S}_j)+\lambda^2(1-\mathbf{S}_i\cdot\mathbf{S}_j+2S_i^xS_j^x)-2t\lambda\hat{\mathbf{x}}\cdot(\mathbf{S}_i\times\mathbf{S}_j)]}. \end{aligned} \tag{3.6}$$

We define the ground state expectation values $D_{ij}^{\gamma}=\langle[e^{ih_{ij}^{\gamma}}d_{ip}^{\dagger}d_{jp}+\text{H.}c.]\rangle_{gs}$ as coupling constants, we obtain the low-energy approximate spin Hamiltonian,

$$\begin{aligned} H_{\text{S}} &= -\sum_{\langle ij\rangle,\gamma} D_{ij}^{\gamma}f_{ij}^{\gamma}, \\ \sqrt{2}f_{ij}^{\gamma} &= \left[t^2(1+\mathbf{S}_i\cdot\mathbf{S}_j)+2t\lambda\,\hat{\boldsymbol{\gamma}}'\cdot(\mathbf{S}_i\times\mathbf{S}_j)+\lambda^2(1-\mathbf{S}_i\cdot\mathbf{S}_j+2(\hat{\boldsymbol{\gamma}}'\cdot\mathbf{S}_i)(\hat{\boldsymbol{\gamma}}'\cdot\mathbf{S}_j))\right]^{1/2} \end{aligned} \tag{3.7}$$

with $\hat{\boldsymbol{\gamma}}'=\hat{z}\times\hat{\boldsymbol{\gamma}}$. We note that the functional form f_{ij}^{γ} was motivated in an earlier work by considering a two-site problem[43]. However, the key argument of performing link-dependent SU(2) rotations to gauge away the Rashba term works only for two isolated sites and cannot be generalized to a lattice. Our derivation is free from such limitations, and provides a model where D_{ij}^{γ} in Eq. (3.7) need not be uniform.

3.3 Comparison with the exact electronic model

The key question is, how well does H_{S} Eq. (3.7) describe the low energy magnetic states of the spin-fermion model H_{RDE}? We directly address this by comparing energetics of the two models in the low temperature regime. Hybrid simulations combining exact diagonalization and Monte Carlo (EDMC) are carried out for H_{RDE} at electronic filling fraction of $n=0.3$[44,55]. Results are compared with simulations on H_{S} using D_{ij}^{γ} as coupling constants. Energy per site E is defined as statistical average $\overline{H_{\text{S}}}/N$ for the pure spin model, and as quantum statistical average $\overline{\langle H_{\text{RDE}}\rangle}/N$ for the spin-fermion model, where the bar denotes the averaging over Monte Carlo steps and N is the number of lattice sites. Comparison of energy per site with varying temperature is shown for representative values of α (see Fig. 3.1) (a)-(b)).

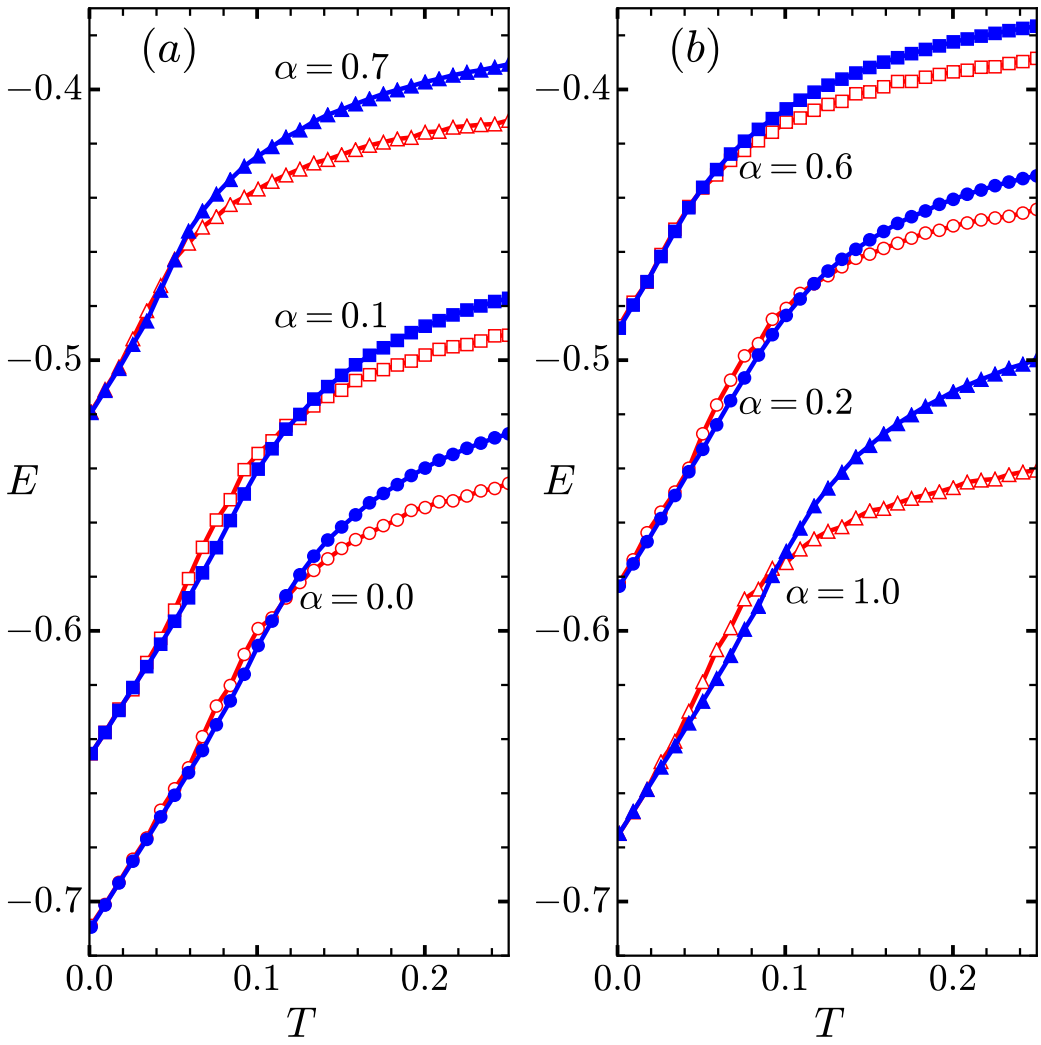

Figure 3.1 (a)-(b) Temperature dependence of energy per site obtained via EDMC simulations of H_{RDE} (open symbols) and that obtained via classical Monte Carlo on H_{S} (filled symbols) for the values of α indicated in the panels. Simulations are carried out on 8×8 lattices.

Ground states are correctly captured by H_{S} for all choices of α, and the energies between H_{RDE} and H_{S} match very well in the low temperature regime. The quantitative agreement can be further improved by using simulation techniques already known for DE systems[56,57]. We can simulate H_{S} using uniform $D_{ij}^{\gamma} \equiv 1$ as an approximation because of the narrow distributions of D_{ij}^{γ} which is illustrated below.

3.4 Distribution of coupling constants

We calculate the distributions of D_{ij}^{γ} for the pairs of nearest neighbor sites in different magnetic ground states obtained by simulating the model with $D_{ij}^{\gamma} \equiv 1$. The D_{ij}^{γ} are

obtained at a generic average filling of 0.3 electrons per site using $D_{ij}^{\gamma} = \langle [e^{ih_{ij}^{\gamma}} d_{ip}^{\dagger} d_{jp} + \text{H.}c.] \rangle_{gs}$. The density of D_{ij}^{γ} is then defined as,

$$\mathcal{N}(D) = 1/N \sum_{\langle ij \rangle} \delta(D - D_{ij}^{\gamma}) \approx 1/N \sum_{\langle ij \rangle} \frac{\eta/\pi}{\eta^2 + (D - D_{ij}^{\gamma})^2},$$

where, η is Lorentzian broadening parameters which is set to 0.001 for calculations.

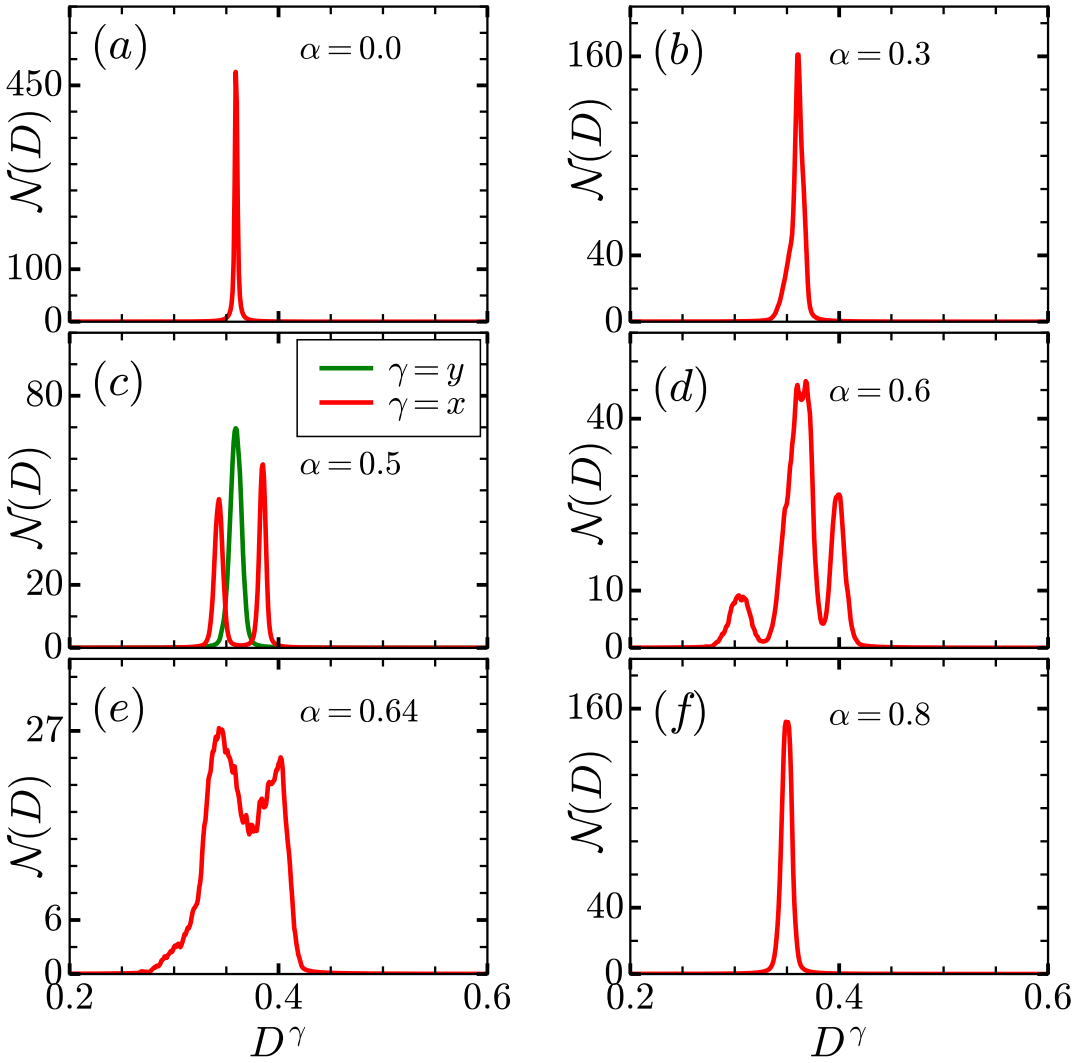

Figure 3.2 Distributions of D_{ij}^{γ} for different ground states, (a) ferromagnet, (b) classical spin liquid, (c) single-Q spiral, (d)-(e) skyrmion crystals, and (f) diagonal-flux, obtained at an average electron filling of $n = 0.3$ per site.

The density of D_{ij}^{γ} is shown in Fig. (3.2) for different values of α. We find that typically the D_{ij}^{γ} distributions are narrow. The D_{ij}^{γ} calculated from EDMC simulations on smaller lattices also lead to similar distributions. This justifies that using a single coupling constant in the effective spin Hamiltonian is a reasonable approximation. However, for the

non-trivial skyrmion states we note multi-peak distributions. This makes it important to perform consistency check on all the ground states obtained in the simulations. We have performed this consistency check now in order to verify the stability of our phase diagram. In the consistency check we calculate D_{ij}^{γ} for the ground state configurations and re-simulate the model with new inhomogeneous parameters. We find all the states to be consistent ground states of the exact spin model $H_S = -\sum D_{ij}^{\gamma} f_{ij}^{\gamma}$. Incidentally, most of the ground states obtained in EDMC on $H_{\rm RDE}$ lead to narrow distributions of D_{ij}^{γ}. This motivates a simplified approximate spin Hamiltonian with $D_{ij}^{\gamma} \equiv D_0$ in Eq. (3.7).

3.5 Magnetic phases of the new spin Hamiltonian

In order to investigate the magnetic phase diagram of the spin Hamiltonian Eq. (3.7) with $D_{ij}^{\gamma} \equiv D_0 = 1$, we use classical Monte Carlo simulations with the standard Metropolis algorithm. The simulations are carried out on lattice sizes varying from $N = 40^2$ to $N = 200^2$, and $\sim 5 \times 10^4$ Monte Carlo steps are used for equilibration and averaging at each temperature point. A consistency check on the stability of ground states is performed simulations on the exact spin Hamiltonian Eq. (3.7) by re-calculating D_{ij}^{γ}. We emphasize that the exact match of ground state energies between the electronic and the effective spin Hamiltonian, as shown in (see Fig. 3.1), is achieved only when inhomogeneities in D_{ij}^{γ} are retained. The different magnetic phases are characterized with the help of component resolved SSF,

$$S_f^{\mu}(\mathbf{q}) \quad = \quad \frac{1}{N^2} \sum_{ij} \overline{S_i^{\mu} S_j^{\mu}} \; e^{-i\mathbf{q}\cdot(\mathbf{r}_i - \mathbf{r}_j)}, \tag{3.8}$$

where, $\mu = x, y, z$ denotes the component of the spin vector and $\mathbf{r}_i$ is the position vector for spin $\mathbf{S}_i$. The total structure factor can be computed as, $S_f(\mathbf{q}) = \sum_{\mu} S_f^{\mu}(\mathbf{q})$. (see Fig. 3.3) shows the temperature variations of characteristic features in the SSF for different values of α. In the small α regime, the ground state is FM (characterized by $S_f(\mathbf{q})$ at $\mathbf{q} = (0,0)$ in Fig. 3.3(a)) and the Curie temperature reduces with increasing α. In the large α limit, d-Flux state characterized by simultaneous appearance of peaks at $\mathbf{q} = (\pi, 0)$ and $\mathbf{q} = (0, \pi)$ in SSF is stabilized (see Fig. 3.4(f)). The corresponding ordering temperature increases with increasing α (see Fig. 3.3(d)). We find two other ordered states at intermediate values of α: SQ spiral states with SSF peaks either at $\mathbf{q} = (q, 0)$ or at $\mathbf{q} = (0, q)$ (see Fig. 3.3(b) and Fig. 3.4(d)), and noncoplanar MQ states with all three components, $\mu = x, y, z$, contributing to total SSF at different $\mathbf{q}$. For

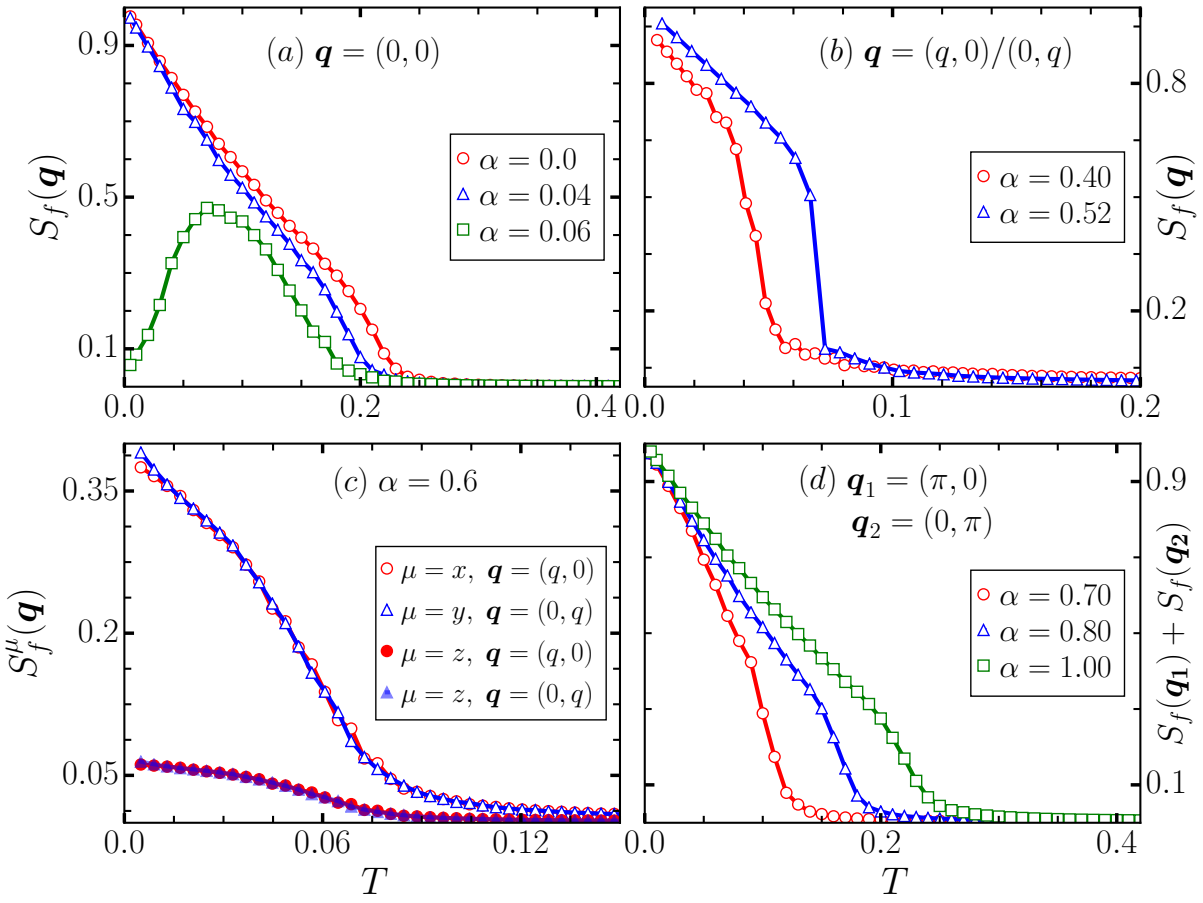

Figure 3.3 (a)-(d) Temperature dependence of different components of SSF for representative values of α. Results are obtained on 60×60 lattice.

$0.06 \leq \alpha \leq 0.34$, the SSF displays a circular pattern without any prominent peaks, suggestive of a liquid-like magnetic state[58–60]. The detailed form of SSF for these unusual phases is discussed below.

We summarize the simulation results in the form of a phase diagram in Fig. 3.4(g). The ground state changes from a FM at small α to a d-Flux at large α, via three non-trivial phases for intermediate values of α. The evolution of the ground state SSF is displayed in Fig. 3.4 (a)-(f).

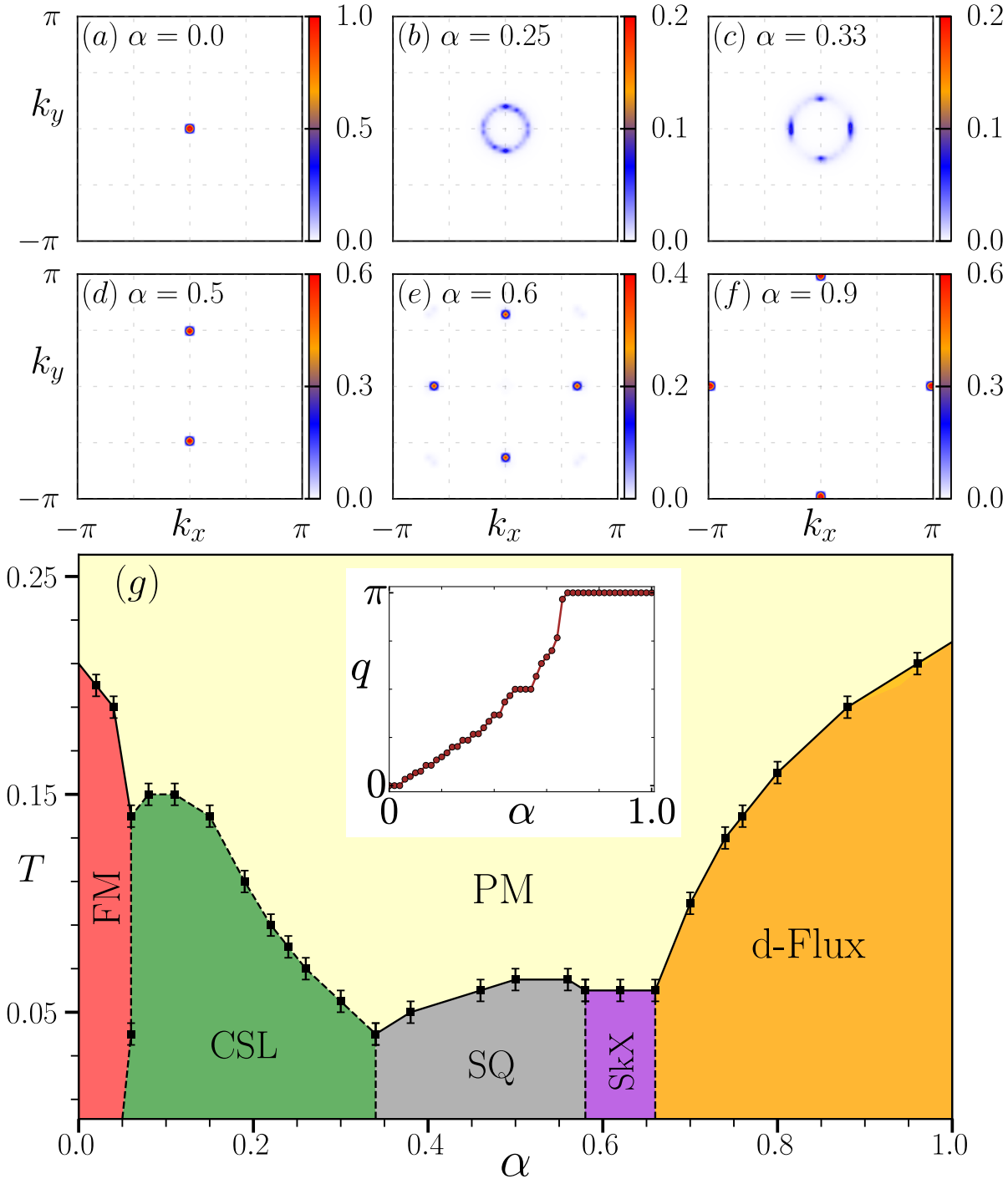

Figure 3.4 (a)-(f) Color map of SSF at $T = 0.001$ for different values of α. (g) Phase diagram for the new spin Hamiltonian in the $T - \alpha$ plane. The boundaries are based on the temperature dependence of the relevant components of the SSF. Inset in (g) shows variation in the magnitude q of the relevant wave-vector $\mathbf{q}$ with α.

As the FM state is destabilized upon increasing α, we do not find any ordered phase. Instead, the SSF shows a diffuse circular pattern (see Fig. 3.4(b)) characteristic of a disordered liquid-like state. The radius of the ring increases upon increasing α, and the intensity near the axial points, $(\pm q, 0)$ and $(0, \pm q)$, becomes relatively large (see Fig. 3.4(c)). For $0.34 < \alpha < 0.58$, we find SQ spiral states with either horizontal or vertical FM stripes (see Fig. 3.4(d) and Fig. 3.5(c)). In a narrow window, $0.58 < \alpha < 0.66$, MQ noncoplanar states are stabilized. Finally the planar d-Flux state is obtained as the ground state for $\alpha > 0.66$. Inflexion point in the temperature dependence of relevant components of SSF are used to identify the boundaries between the paramagnet (PM) and ordered phases. Note that, in case of CSL state a well defined order parameter does not exist, and dashed line indicates the temperature at which the diffuse ring pattern appears in the SSF.

We provide a clear understanding of the ground state evolution in terms of typical low temperature spin configurations in (see Fig. 3.5). Upon increasing α, the FM state is destabilized and typical configurations consist of filamentary structures of domain walls (see Fig. 3.5(a)-(b)). The stability of the filamentary structures is related to an unusual degeneracy of spiral states (Box 1). The fact that domain walls can turn in arbitrary direction with negligible energy cost is responsible for the presence of the diffuse circular pattern in the SSF (see Fig. 3.4 (b)). For larger values of α, the width of domain walls decreases and a preference for horizontal or vertical orientations of the domain walls is found (see Fig. 3.5 (b)). This is reflected in the appearance of arc features in SSF near the axial points (see Fig. 3.4 (c)). For $\alpha > 0.58$ we obtain long-range ordered MQ states. The MQ states can be non-coplanar (see Fig. 3.5 (d)-(e)) or coplanar (see Fig. 3.5 (f)). The noncoplanar patterns in the MQ states are identical to lattices of smallest skyrmions[62].

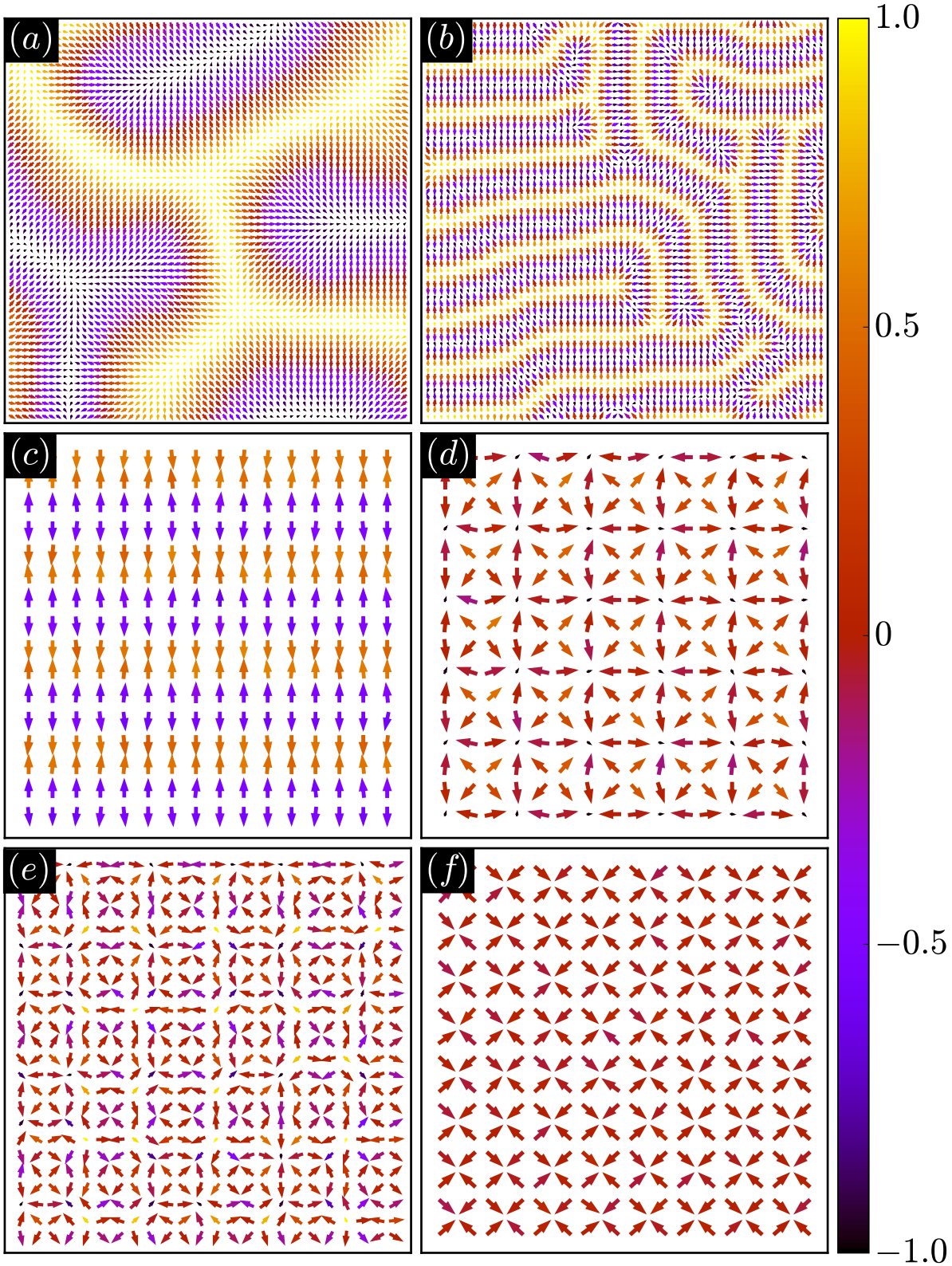

Figure 3.5 Snapshots of spin configurations obtained at low temperature for, (a) $\alpha = 0.10$, (b) $\alpha = 0.34$, (c) $\alpha = 0.50$, (d) $\alpha = 0.60$, (e) $\alpha = 0.64$, and (f) $\alpha = 0.80$. The x and y components of the spins are indicated by the arrow while the z component is color coded. For (a)-(b) we show 60×60 lattice. For the ordered states we display for clarity only a smaller section, 16×16 for (c), (d) and (f) and 24×24 for (e), of the full lattice. The configurations are shown at $T = 0.001$.

Box 1: Origin of classical spin liquid (CSL) behavior

We provide a simple description of CSL states observed in the small α regime. A careful look at the form of the Hamiltonian Eq. (3.7) suggests that for small values of α, terms proportional to λ^2 may be ignored. The only non-trivial effect then comes from terms proportional to $t\lambda$. These terms prefer spiral states with competing orientations of the spiral planes. Along x-direction, a spiral in xz plane is preferred and along y-direction a spiral in yz plane is preferred. This motivates us to construct the following variational ansatz where the plane of the spiral is one of the variational parameters:

$$\begin{aligned} S_i^x &= S_0 \sin(\boldsymbol{q}.\boldsymbol{r}_i)\cos(\Phi_p), \\ S_i^y &= S_0 \sin(\boldsymbol{q}.\boldsymbol{r}_i)\sin(\Phi_p), \\ S_i^z &= S_0 \cos(\boldsymbol{q}.\boldsymbol{r}_i). \end{aligned} \tag{3.9}$$

In the above, S_0 is the unit magnitude of the classical spin vectors, Φ_p is the orientation of the spiral plane ($\Phi_p = 0$ for xz plane and $\Phi_p = \frac{\pi}{2}$ for yz plane) and $\boldsymbol{q} = q(\cos\beta, \sin\beta)$ is the spiral wave-vector. In the CSL state, we find that the energy of a spiral is independent of the spiral plane angle Φ_p, provided the wave-vector angle β is related to Φ_p via $\beta - \Phi_p = \pi$. This explains the stability of filamentary domain wall structure in the CSL regime: the domain walls can freely reorient as long as the spiral plane also undergoes a reorientation in such a way that the spiral plane is oriented perpendicular to the local orientation of the domain wall. While the re-orientations of domain walls are energetically free, change in their width does cost energy. This leads to an intermediate degeneracy with $O(e^{\sqrt{N}})$ configurations, as opposed to a true macroscopic degeneracy with $O(e^N)$ ground states. This peculiar nature of the degeneracy may effect how a specific Monte Carlo update dynamics explores the configuration space.

In order to quantify the degeneracy of spiral states, we define $\Delta E = \max[E_{min}(\Phi_p)] - \min[E_{min}(\Phi_p)]$. $E_{min}(\Phi_p)$ represents the minimum energy obtained for a given orientation of the spiral plane, marked by a square symbol Fig. 3.6. Exact degeneracy is characterized by $\Delta E = 0$. We show the variation of ΔE with the coupling constant α as an inset in Fig. 3.6 (b). The degree of degeneracy clearly reduces near $\alpha = 0.35$, which coincides with the crossover point between CSL and SQ spiral states.

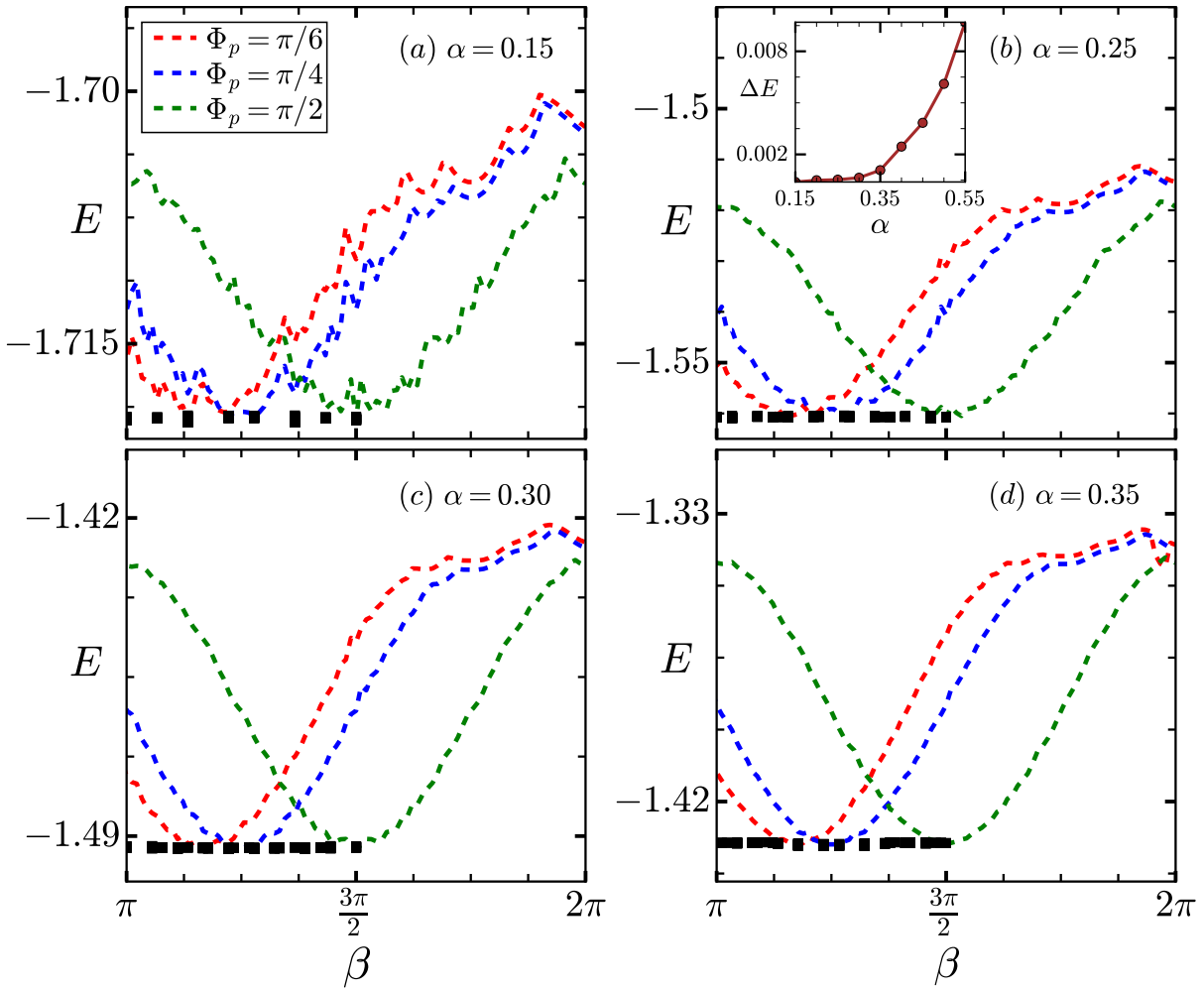

Figure 3.6 Energy per site E as a function of wave-vector direction β, for (a) α = 0.15, (b) α = 0.25, (c) α = 0.30 and (d) α = 0.35, obtained for states defined via variational ansatz Eq. (3.9). Energy is minimized over the magnitude q of $\boldsymbol{q}$. Square symbols represent the minimum value, E_{min}, of E for each choice of Φ_p. Inset in panel (b) shows the variation with α of the width ΔE of E_{min}.

3.6 Finite size effects

We now discuss the finite size effects that lead to minor changes in the phase diagram shown in Fig. 3.4(g). We plot below the variation in magnitude q of the ordering wave vector $\mathbf{q}$ as a function of α (also shown in inset of Fig. 3.4(g)) obtained at low temperature ($T = 0.001$) for different lattice sizes. In general, the competition between FM and DM interactions leads to spiral phases. However, the possible spiral wave vectors depend on the linear dimension of the lattice. For example, the smallest non-zero spiral wave vector for SQ states with $\mathbf{q} = (q,0)/(0,q)$ is $q = 2\pi/\sqrt{N}$ for an N site square lattice. This suggests that the FM state described by $q = 0$ will remain stable over a wider

range of α on smaller lattice sizes. This is indeed true as shown in (see Fig. 3.7(a)-(c)) . Similarly, the state at $q = \pi/2$ has an extra range of stability due to finite lattice sizes. We extract the discontinuity in q, δq, near $q = 0$ and $q = \pi/2$ and plot these δq values as a function of inverse linear dimension. The data simply falls on the expected $\delta q = 2\pi/\sqrt{N}$ line (see Fig. 3.7(d)). Hence, we conclude that the FM phase as well as the $q = \pi/2$ spiral phase will not have extended window of stability and hence disappear in the thermodynamic limit.

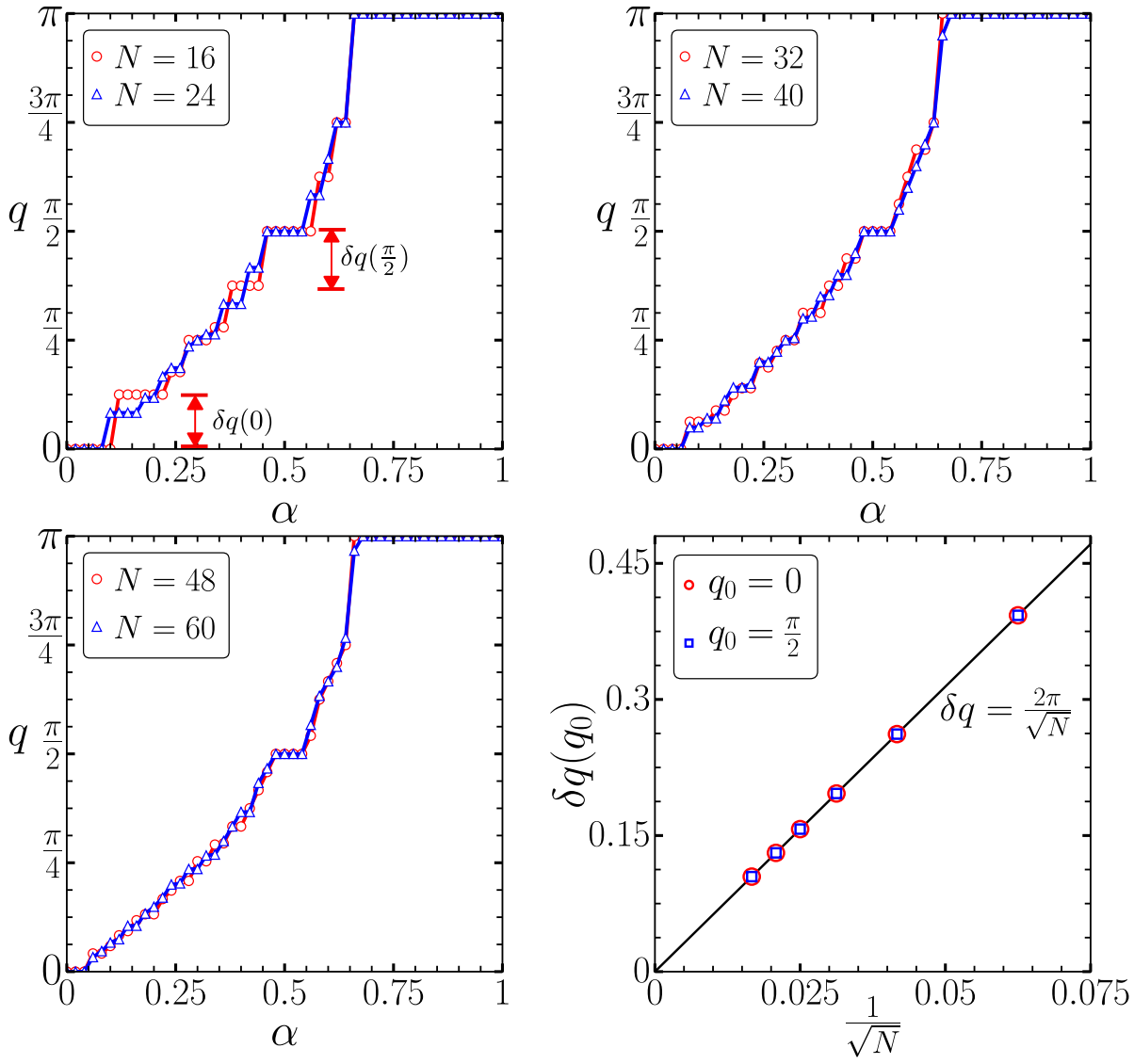

Figure 3.7 (a)-(c) Variation of the magnitude q of the ordering wave vector $\mathbf{q}$ with α for simulations performed on different lattice sizes. (d) Discontinuity δq near $\mathbf{q} = (0,0)$ and $\mathbf{q} = (q,0)/(0,q)$ states as a function of $1/\sqrt{N}$. Red circles (blue squares) denote the value of δq near the FM (spiral) state. Black solid line is the expected behavior showing that δq will extrapolate to zero as $N \to \infty$

3.7 Conclusion

We have derived a spin Hamiltonian on a lattice for DE metals in the presence of Rashba SOC. The model, in general, has inhomogeneous coupling constants and anisotropic DM and pseudo-dipolar interactions, similar to those required for stabilizing exotic spin textures. We explicitly compare the energetics in the low temperature regime between the exact Hamiltonian and our spin model in order to prove the validity of the latter. Increasing the relative strength of Rashba term w.r.t. the hopping generates CSL, SQ spiral and MQ SkX states, starting from the trivial FM phase. An elegant description of this evolution emerges from the ground state degeneracy analysis. Our spin model provides a consistent description of spin textures in itinerant magnets. In particular, the filamentary domain wall structures obtained in our simulations are in excellent agreement with the experimental observations in thin films and multilayers of transition metals[20,26,27,29,63]. Typically, one would associate such irregular spin textures to impurities or defects in the samples. However, our microscopic analysis without including any ad hoc term in the Hamiltonian shows that these are intrinsic features of the electronic system. While quenched disorder in a real sample may lead to the pinning of these filamentary domains, we predict that in a disorder free sample a re-orientation dynamics of the domain walls should be observed. Interestingly, similar domain patterns were noticed many years back in FM garnet films[64].

The weak coupling approach to understand magnetism in spin orbit coupled itinerant magnets is via RKKY type effective models[53]. Such models are long ranged and strongly depend on the filling fraction of the conduction band. In contrast, the form of the spin Hamiltonian discussed here is independent of the electronic filling fraction. Therefore, in our description, the exotic magnetic states do not originate from Fermi surface nesting features. Consequently, such states are expected without fine-tuning of electron density. This is consistent with the fact that such spin textures are experimentally observed in a variety of thin films and multilayers of transition metals. While the model is derived starting from the FKLM, at the mean-field level similar physics should hold for the Hubbard model where localized and itinerant electrons are associated with the same band[65,66].

Bibliography

[1] S. Woo, K. Litzius, B. Krüger, M. Y. Im, L. Caretta, K. Richter, M. Mann, A. Krone, R. M. Reeve, M. Weigand, P. Agrawal, I. Lemesh, M. A. Mawass, P. Fischer, M. Kläui, and G. S. Beach, Nat. Mater. **15** (2016), 10.1038/nmat4593, arXiv:1502.07376 .

[2] X. Z. Yu, W. Koshibae, Y. Tokunaga, K. Shibata, Y. Taguchi, N. Nagaosa, and Y. Tokura, Nature **564**, 95 (2018).

[3] X. Z. Yu, Y. Onose, N. Kanazawa, J. H. Park, J. H. Han, Y. Matsui, N. Nagaosa, and Y. Tokura, Nature **465**, 901 (2010).

[4] M. Hoffmann, B. Zimmermann, G. P. Müller, D. Schürhoff, N. S. Kiselev, C. Melcher, and S. Blügel, Nat. Commun. **8**, 308 (2017).

[5] A. K. Nayak, V. Kumar, T. Ma, P. Werner, E. Pippel, R. Sahoo, F. Damay, U. K. Rößler, C. Felser, and S. S. P. Parkin, Nature **548**, 561 (2017).

[6] T. Kurumaji, T. Nakajima, V. Ukleev, A. Feoktystov, T. H. Arima, K. Kakurai, and Y. Tokura, Phys. Rev. Lett. **119** (2017), 10.1103/PhysRevLett.119.237201, arXiv:1710.04000 .

[7] N. Kanazawa, J.-H. Kim, D. S. Inosov, J. S. White, N. Egetenmeyer, J. L. Gavilano, S. Ishiwata, Y. Onose, T. Arima, B. Keimer, and Y. Tokura, Phys. Rev. B **86**, 134425 (2012).

[8] A. Fert, N. Reyren, and V. Cros, Nat. Rev. Mater. **2**, 17031 (2017).

[9] N. J. Laurita, G. G. Marcus, B. A. Trump, J. Kindervater, M. B. Stone, T. M. McQueen, C. L. Broholm, and N. P. Armitage, Phys. Rev. B **95**, 235155 (2017).

[10] R. Wiesendanger, Nat. Rev. Mater. **1**, 16044 (2016).

[11] A. Fert, V. Cros, and J. Sampaio, Nat. Nanotechnol. **8**, 152 (2013).

[12] N. Nagaosa and Y. Tokura, Nat. Nanotechnol. **8**, 899 (2013).

[13] B. Göbel, A. Mook, J. Henk, and I. Mertig, Phys. Rev. B **99**, 020405 (2019).

[14] T. Zhou, N. Mohanta, J. E. Han, A. Matos-Abiague, and I. Žutić, Phys. Rev. B **99**, 134505 (2019).

[15] J. Kindervater, I. Stasinopoulos, A. Bauer, F. X. Haslbeck, F. Rucker, A. Chacon, S. Mühlbauer, C. Franz, M. Garst, D. Grundler, and C. Pfleiderer, Phys. Rev. X **9**, 041059 (2019).

[16] J. Zang, M. Mostovoy, J. H. Han, and N. Nagaosa, Phys. Rev. Lett. **107**, 136804 (2011).

[17] S. Sorn, S. Divic, and A. Paramekanti, Phys. Rev. B **100**, 174411 (2019).

[18] T. Gao, A. Qaiumzadeh, H. An, A. Musha, Y. Kageyama, J. Shi, and K. Ando, Phys. Rev. Lett. **121**, 017202 (2018).

[19] A. Barcza, Z. Gercsi, K. S. Knight, and K. G. Sandeman, Phys. Rev. Lett. **104**, 247202 (2010).

[20] S. Woo, K. M. Song, X. Zhang, Y. Zhou, M. Ezawa, X. Liu, S. Finizio, J. Raabe, N. J. Lee, S.-I. Kim, S.-Y. Park, Y. Kim, J.-Y. Kim, D. Lee, O. Lee, J. W. Choi, B.-C. Min, H. C. Koo, and J. Chang, Nat. Commun. **9**, 959 (2018).

[21] S. M. Stishov, A. E. Petrova, S. Khasanov, G. K. Panova, A. A. Shikov, J. C. Lashley, D. Wu, and T. A. Lograsso, Phys. Rev. B **76**, 052405 (2007).

[22] X. Z. Yu, N. Kanazawa, Y. Onose, K. Kimoto, W. Z. Zhang, S. Ishiwata, Y. Matsui, and Y. Tokura, Nat. Mater. **10**, 106 (2011).

[23] X. Zhao, C. Jin, C. Wang, H. Du, J. Zang, M. Tian, R. Che, and Y. Zhang, Proc. Natl. Acad. Sci. U. S. A. **113**, 4918 (2016).

[24] C. Pfleiderer, D. Reznik, L. Pintschovius, H. v. Löhneysen, M. Garst, and A. Rosch, Nature **427**, 227 (2004).

[25] B. Dupé, M. Hoffmann, C. Paillard, and S. Heinze, Nat. Commun. **5**, 4030 (2014).

[26] S. D. Pollard, J. A. Garlow, J. Yu, Z. Wang, Y. Zhu, and H. Yang, Nat. Commun. **8**, 14761 (2017).

[27] A. Soumyanarayanan, M. Raju, A. L. Gonzalez Oyarce, A. K. C. Tan, M.-Y. Im, A. Petrović, P. Ho, K. H. Khoo, M. Tran, C. K. Gan, F. Ernult, and C. Panagopoulos, Nat. Mater. **16**, 898 (2017).

[28] S. Meyer, M. Perini, S. von Malottki, A. Kubetzka, R. Wiesendanger, K. von Bergmann, and S. Heinze, Nat. Commun. **10**, 3823 (2019).

[29] T. Nagase, M. Komatsu, Y. G. So, T. Ishida, H. Yoshida, Y. Kawaguchi, Y. Tanaka, K. Saitoh, N. Ikarashi, M. Kuwahara, and M. Nagao, Phys. Rev. Lett. **123**, 137203 (2019).

[30] A. Farrell and T. Pereg-Barnea, Phys. Rev. B **89**, 035112 (2014).

[31] J. P. Chen, D.-W. Zhang, and J. M. Liu, Sci. Rep. **6**, 29126 (2016).

[32] U. K. Rößler, A. A. Leonov, and A. N. Bogdanov, J. Phys. Conf. Ser. **200**, 022029 (2010).

[33] M. A. Ruderman and C. Kittel, Phys. Rev. **96**, 99 (1954).

[34] T. Kasuya, Prog. Theor. Phys. **16**, 45 (1956).

[35] K. Yosida, Phys. Rev. **106**, 893 (1957).

[36] S. Hayami and Y. Motome, Phys. Rev. Lett. **121**, 137202 (2018).

[37] A. V. Bezvershenko, A. K. Kolezhuk, and B. A. Ivanov, Phys. Rev. B **97**, 054408 (2018).

[38] S. Seki, J.-H. Kim, D. S. Inosov, R. Georgii, B. Keimer, S. Ishiwata, and Y. Tokura, Phys. Rev. B **85**, 220406 (2012).

[39] S. Seki, X. Z. Yu, S. Ishiwata, and Y. Tokura, Science **336**, 198 (2012).

[40] I. Dzyaloshinsky, J. Phys. Chem. Solids **4**, 241 (1958).

[41] T. Moriya, Phys. Rev. **120**, 91 (1960).

[42] U. K. Rößler, A. N. Bogdanov, and C. Pfleiderer, Nature **442**, 797 (2006).

[43] S. Banerjee, J. Rowland, O. Erten, and M. Randeria, Phys. Rev. X **4**, 031045 (2014).

[44] E. Dagotto, *Nanoscale Phase Separation and Collosal Magnetoresistance* (Springer Berlin/Heidelberg, Berlin, 2002).

[45] G. Alvarez, M. Mayr, and E. Dagotto, Phys. Rev. Lett. **89**, 277202 (2002).

[46] M. Berciu and R. N. Bhatt, Phys. Rev. Lett. **87**, 107203 (2001).

[47] K. Pradhan and S. K. Das, Sci. Rep. **7**, 9603 (2017).

[48] A. Yaouanc, P. Dalmas de Réotier, B. Roessli, A. Maisuradze, A. Amato, D. Andreica, and G. Lapertot, Phys. Rev. Res. **2**, 013029 (2020).

[49] D. Bombor, C. G. F. Blum, O. Volkonskiy, S. Rodan, S. Wurmehl, C. Hess, and B. Büchner, Phys. Rev. Lett. **110**, 066601 (2013).

[50] C. Felser, L. Wollmann, S. Chadov, G. H. Fecher, and S. S. P. Parkin, APL Mater. **3**, 041518 (2015).

[51] E. Şaşıoğlu, L. M. Sandratskii, and P. Bruno, Phys. Rev. B **77**, 064417 (2008).

[52] A. Manchon, H. C. Koo, J. Nitta, S. M. Frolov, and R. A. Duine, Nat. Mater. **14**, 871 (2015).

[53] K. N. Okada, Y. Kato, and Y. Motome, Phys. Rev. B **98**, 224406 (2018).

[54] "See supplemental material for further details." .

[55] S. Yunoki, J. Hu, A. L. Malvezzi, A. Moreo, N. Furukawa, and E. Dagotto, Phys. Rev. Lett. **80**, 845 (1998).

[56] S. Kumar and P. Majumdar, Eur. Phys. J. B **46**, 315 (2005).

[57] M. J. Calderón and L. Brey, Phys. Rev. B **58**, 3286 (1998).

[58] Y. Tokiwa, J. J. Ishikawa, S. Nakatsuji, and P. Gegenwart, Nat. Mater. **13**, 356 (2014).

[59] H. Okabe, M. Hiraishi, A. Koda, K. M. Kojima, S. Takeshita, I. Yamauchi, Y. Matsushita, Y. Kuramoto, and R. Kadono, Phys. Rev. B **99**, 041113 (2019).

[60] S. Nakatsuji, Y. Machida, Y. Maeno, T. Tayama, T. Sakakibara, J. van Duijn, L. Balicas, J. N. Millican, R. T. Macaluso, and J. Y. Chan, Phys. Rev. Lett. **96**, 087204 (2006).

[61] J. W. F. Venderbos, M. Daghofer, J. van den Brink, and S. Kumar, Phys. Rev. Lett. **107**, 076405 (2011).

[62] B. F. McKeever, D. R. Rodrigues, D. Pinna, A. Abanov, J. Sinova, and K. Everschor-Sitte, Phys. Rev. B **99**, 054430 (2019).

[63] S. Woo, K. M. Song, H.-S. Han, M.-S. Jung, M.-Y. Im, K.-S. Lee, K. S. Song, P. Fischer, J.-I. Hong, J. W. Choi, B.-C. Min, H. C. Koo, and J. Chang, Nat. Commun. **8**, 15573 (2017).

[64] M. Seul and D. Andelman, Science **267**, 476 (1995).

[65] I. Martin and C. D. Batista, Phys. Rev. Lett. **101**, 156402 (2008).

[66] K. Pasrija and S. Kumar, Phys. Rev. B **93**, 195110 (2016).

4

Electronic mechanism for nanoscale skyrmions and topological metals

---

Adapted from the work :

Deepak. S. Kathyat, Arnob Mukherjee, and Sanjeev Kumar

PHYSICAL REVIEW B **103**, 035111 (2021)

4.1 Introduction

Magnetic skyrmions are being envisioned as building blocks of next-generation data storage and processing devices[1–6]. This has led to a surge in research activity geared towards identifying candidate materials[7–18]. Such textures in metals are particularly important since they can be manipulated by ultra-low electrical currents[10,11,19,20]. Appearance of skyrmions has been reported in bulk as well as in thin films of a variety of chiral metallic magnets[12–15,21–26]. However, the current understanding of skyrmion formation in magnets is via spin Hamiltonians that either include Dzyaloshinskii-Moriya (DM) interactions or geometrical frustration[27–31]. Such studies have also shown formation of three dimensional lattices of skyrmions, relevant for skyrmions in bulk[32,33]. This approach is inconsistent for metals as the aforementioned terms are usually understood as arising from the effect of spin-orbit coupling in Mott insulators[34]. Therefore, the importance of electronic Hamiltonian based understanding of skyrmion formation in metals has been recognized and a mechanism based on RKKY interactions has recently been put forward[35,36]. Furthermore, most theoretical studies describe states that are periodic arrangement of skyrmions. Whereas, experiments on certain thin films or on constricted samples also support a phase with sparse skyrmions[9,26,37,38].

Introduction of double exchange (DE) mechanism by Zenger represents a milestone in our understanding of ferromagnetic metals[39–41]. The mechanism has played a key role in the description of magnetic and magneto-transport phenomena across families of materials, such as, perovskite manganites, dilute magnetic semiconductors and Heusler metals[42–45]. Surprisingly, the role of DE physics in skyrmion formation has largely remained unexplored. On the other hand, DE mechanism is commonly invoked when studying the effect of magnetic textures, including skyrmions, on transport properties in metals. The implication of spin-orbit modified DE physics on transport properties has recently been discussed[46].

In this work, we show that the Rashba DE (RDE) model in the presence of Zeeman field leads to states hosting nano-skyrmions. We explicitly demonstrate the appearance of skyrmions using the state-of-the-art hybrid Monte Carlo (HMC) simulations. An effective spin Hamiltonian is studied for a comprehensive understanding of the origin as well as stability of these spin textures. A filamentary domain wall (fDW) phase is identified as the parent of sparse skyrmions (sSk), which are found to be stable only at finite temperatures and metastable in the ground state, and a single-Q (SQ) spiral state leads to packed skyrmions (pSk). Our findings are consistent with small angle neutron scattering (SANS) and Lorentz transmission electron microscopy (LTEM) data on thin films of

Co-Zn-Mn alloys, FeGe and MnSi, and transition metal multilayers[10–13,25,26,47,48]. Furthermore, we explicitly demonstrate by calculating Bott index and the topological Hall conductivity that the skyrmion phases are a natural realizations of amorphous topological metals. This is particularly important in view of recent attempts to engineer tight-binding models for the realization of amorphous topological phases[49–51]. We also present LDOS calculations to show the importance of consistent treatment of spin-orbit coupling for the skyrmion formation and for electronic transport aspects. A combination of dI/dV measurements and LDOS analysis can be a useful alternate to the existing methods for estimating the strength of Rashba coupling in real materials.

4.2 Skyrmions in the RDE model

We start with the ferromagnetic Kondo lattice model (FKLM) in the presence of Rashba SOC, described by the Hamiltonian,

$$\begin{aligned} H &= -t\sum_{\langle ij\rangle,\sigma}(c^{\dagger}_{i\sigma}c_{j\sigma}+\text{H.c.})+\lambda\sum_{i}[(c^{\dagger}_{i\downarrow}c_{i+x\uparrow}-c^{\dagger}_{i\uparrow}c_{i+x\downarrow}) \\ &\quad +\mathrm{i}(c^{\dagger}_{i\downarrow}c_{i+y\uparrow}+c^{\dagger}_{i\uparrow}c_{i+y\downarrow})+\text{H.c.}]-J_H\sum_{i}\mathbf{S}_i\cdot\mathbf{s}_i. \end{aligned} \tag{4.1}$$

Here, $c_{i\sigma}(c^{\dagger}_{i\sigma})$ annihilates (creates) an electron at site i with spin σ, $\langle ij\rangle$ implies that i and j are nearest neighbor (nn) sites. λ and J_H denote the strengths of Rashba and Hund's coupling, respectively. $\mathbf{s_i}$ is the electronic spin operator at site i, and $\mathbf{S}_i$, with $|\mathbf{S}_i|=1$, denotes the localized spin at that site. We parameterize $t=(1-\alpha)t_0$ and $\lambda=\alpha t_0$ and set $t_0=1$ as the reference energy scale. Assuming large J_H and taking the double-exchange approximation, we obtain the RDE Hamiltonian[52],

$$H_{\text{RDE}} = \sum_{\langle ij\rangle,\gamma}[g^{\gamma}_{ij}d^{\dagger}_i d_j+\text{H.c.}]-h_z\sum_i S^z_i, \tag{4.2}$$

where, $d_i(d^{\dagger}_i)$ annihilates (creates) an electron at site i with spin parallel to the localized spin. The second term represents the Zeeman coupling of local moments to external magnetic field of strength h_z. Site $j=i+\gamma$ is the nn of site i along spatial direction $\gamma=x,y$. The projected hopping $g^{\gamma}_{ij}=t^{\gamma}_{ij}+\lambda^{\gamma}_{ij}$ depend on the orientations of the local

moments $\mathbf{S}_i$ and $\mathbf{S}_j$[52],

$$\begin{aligned} t_{ij}^{\gamma} &= -t\left[\cos(\frac{\theta_i}{2})\cos(\frac{\theta_j}{2}) + \sin(\frac{\theta_i}{2})\sin(\frac{\theta_j}{2})e^{-\mathrm{i}(\phi_i-\phi_j)}\right], \\ \lambda_{ij}^{x} &= \lambda\left[\sin(\frac{\theta_i}{2})\cos(\frac{\theta_j}{2})e^{-\mathrm{i}\phi_i} - \cos(\frac{\theta_i}{2})\sin(\frac{\theta_j}{2})e^{\mathrm{i}\phi_j}\right], \\ \lambda_{ij}^{y} &= \mathrm{i}\lambda\left[\sin(\frac{\theta_i}{2})\cos(\frac{\theta_j}{2})e^{-\mathrm{i}\phi_i} + \cos(\frac{\theta_i}{2})\sin(\frac{\theta_j}{2})e^{\mathrm{i}\phi_j}\right], \end{aligned} \tag{4.3}$$

where, θ_i (ϕ_i) denotes the polar (azimuthal) angle for localized spin $\mathbf{S}_i$.

We study the RDE Hamiltonian using numerically exact hybrid Monte Carlo (HMC) simulations as discussed in Section 2.7.3. Presence of skyrmions is inferred via local skyrmion density[28],

$$\chi_i = \frac{1}{8\pi}[\mathbf{S}_i \cdot (\mathbf{S}_{i+x} \times \mathbf{S}_{i+y}) + \mathbf{S}_i \cdot (\mathbf{S}_{i-x} \times \mathbf{S}_{i-y})]. \tag{4.4}$$

Total skyrmion density is defined as, $\chi = \sum_i \chi_i$. We also compute the spin structure factor (SSF),

$$S_f(\mathbf{q}) = \frac{1}{N^2}\sum_{ij} \mathbf{S}_i \cdot \mathbf{S}_j \; e^{-\mathrm{i}\mathbf{q}\cdot(\mathbf{r}_i-\mathbf{r}_j)}, \tag{4.5}$$

and the relevant component of vector chirality η as,

$$\eta = \frac{1}{N}\sum_i (\mathbf{S}_i \times \mathbf{S}_{i+x}) \cdot \hat{y} - (\mathbf{S}_i \times \mathbf{S}_{i+y}) \cdot \hat{x}. \tag{4.6}$$

Averaging of all quantities over MC steps is implicitly assumed, unless stated otherwise.

Results obtained via HMC simulations for two representative values of α are shown in Fig. 4.1. Upon increasing h_z, Magnetization, $M_z = \frac{1}{N}\sum_i S_i^z$, increases and η decreases. The magnitude of χ initially increases with applied field, and then decreases on approach to the saturated ferromagnetic (sFM) state (see circles in Fig. 4.1(a), (d)). The qualitative behavior appears to be similar between $\alpha = 0.25$ and $\alpha = 0.45$. The negative sign of χ reveals that the polarity of skyrmions is opposite to the orientation of the background magnetization.

The existence of skyrmions in the RDE Hamiltonian is explicitly demonstrated via the spin configurations as well as skyrmion density maps in the ground state. We find that small values of α lead to sparse skyrmions within the zero field cooled (ZFC) protocol (see Fig. 4.1(b)), and the packing (size) of skyrmions increases (decreases) with increasing α (see Fig. 4.1(e)). The negative polarity is consistent with the fact that the

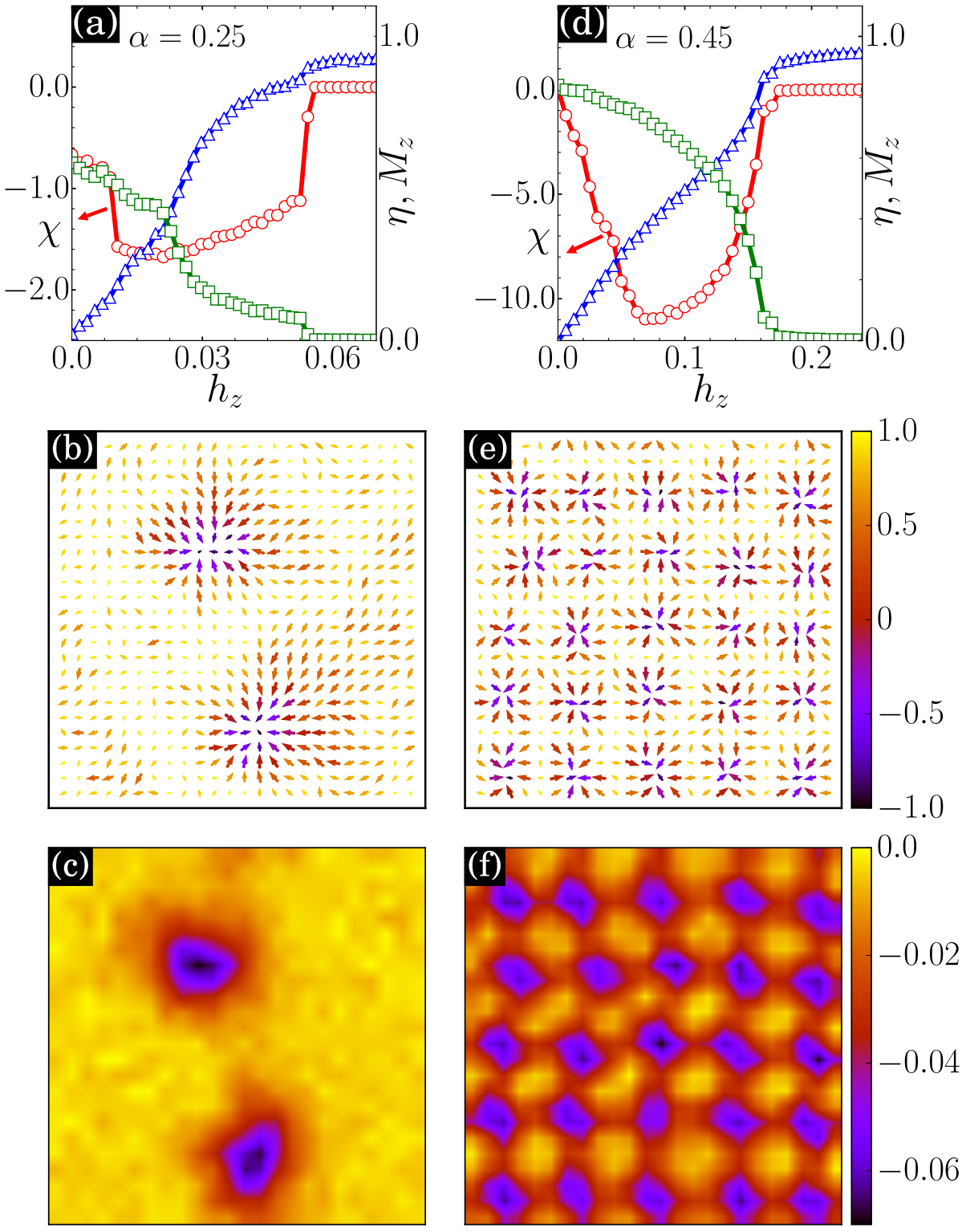

Figure 4.1 Magnetization M_z (triangles), total skyrmion density χ (circles) and vector chirality η (squares) as a function of applied Zeeman field for, (a) $\alpha = 0.25$, and (d) $\alpha = 0.45$. Snapshots of spin configurations, (b), (e), and the local skyrmion density, (c), (f), at $T = 0.01$ for representative values of α and h_z: (b)-(c) $\alpha = 0.25$, $h_z = 0.03$; (e)-(f) $\alpha = 0.45$, $h_z = 0.09$.

central spin in the skyrmion texture is oriented opposite to the magnetization direction (see Fig. 4.1(c), (f)). We also note that the skyrmions obtained here are of Neel type with negative effective magnetic monopole charge. In order to understand the origin and stability of sSk and pSk, we present results on an effective spin model derived from the RDE Hamiltonian.

4.3 Origin and stability of sparse and packed skyrmions

Including the Zeeman coupling term in the recently derived effective spin model for $H_{\rm RDE}$[52], we obtain,

$$\begin{aligned} H_{\rm eff} &= -\sum_{\langle ij\rangle,\gamma} D_{ij}^{\gamma} f_{ij}^{\gamma} - h_z \sum_i S_i^z, \\ \sqrt{2} f_{ij}^{\gamma} &= \big[t^2(1+\mathbf{S}_i\cdot\mathbf{S}_j) + 2t\lambda\hat{\gamma}'\cdot(\mathbf{S}_i\times\mathbf{S}_j) \\ &\quad +\lambda^2(1-\mathbf{S}_i\cdot\mathbf{S}_j+2(\hat{\gamma}'\cdot\mathbf{S}_i)(\hat{\gamma}'\cdot\mathbf{S}_j))\big]^{1/2}, \\ D_{ij}^{\gamma} &= \langle[e^{ih_{ij}^{\gamma}} d_i^{\dagger} d_j + \text{H.c.}]\rangle_{gs}. \end{aligned} \tag{4.7}$$

In the above, $\hat{\gamma}' = \hat{z}\times\hat{\gamma}$, f_{ij}^{γ} (h_{ij}^{γ}) is the modulus (argument) of complex number g_{ij}^{γ} and $\langle\hat{O}\rangle_{gs}$ denotes expectation values of operator $\hat{O}$ in the ground state. It has been shown that using a constant value of D_{ij}^{γ} captures the essential physics of the Hamiltonian Eq. (4.7), therefore we set $D_{ij}^{\gamma} \equiv D_0 = 1$ in our simulations[52]. Note that a derivation starting with a simple two-site picture also leads to an identical functional form for the effective spin model[55].

We simulate $H_{\rm eff}$ using the conventional classical MC scheme as discussed in Section 2.7.1. We find that the field-dependence of magnetization, η and χ for $H_{\rm eff}$ is similar to that obtained via HMC (compare Fig. 4.1 (a), (d) and Fig. 4.2). For small values of α, magnetization increases linearly for small h_z, followed by a slower than linear rise. This change to non-linear behaviour is accompanied by a sharp increase in the magnitude of χ (see Fig. 4.2(a), (b)). A simple understanding is that the emergence of skyrmions arrests the ease with which spins align along the direction of external magnetic field. A finite value of η in the absence of magnetic field originates from the DM-like terms present in the effective Hamiltonian. Variation of η is anticorrelated with that of magnetization and the former shows a sharp decrease accompanying the increase in magnitude of χ (see Fig. 4.2(a), (b)). Finally, for still larger values of applied field, system approaches sFM state, with both χ and η vanishing. For $\alpha = 0.5$, the change in χ near $h_z = 0.25$ is sharper, and is accompanied by a weak discontinuity in

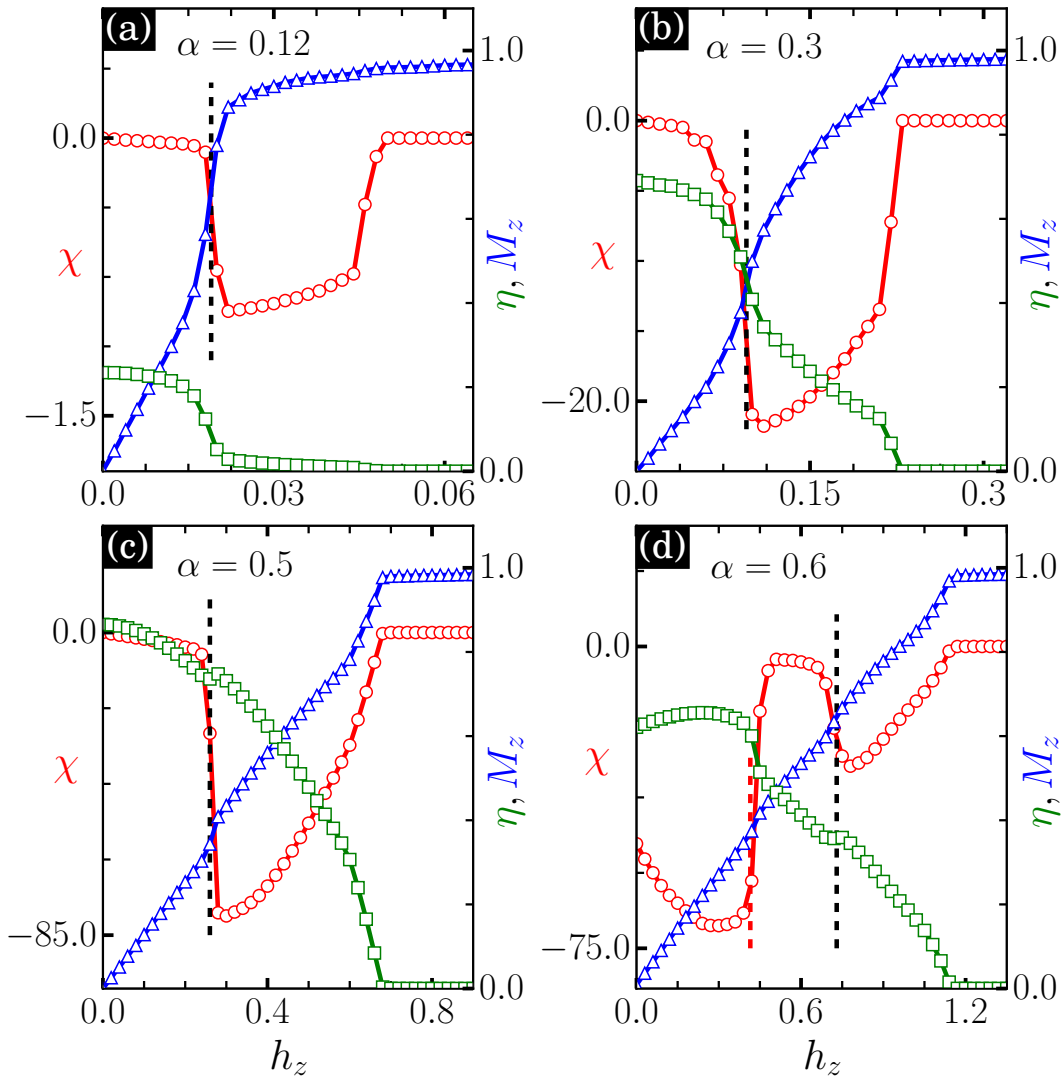

Figure 4.2 (a) - (d) Magnetization (triangles), total skyrmion density (circles) and vector chirality (squares) as a function of h_z for different values of α. Left y-axis scale is for χ.

both magnetization and η (see Fig. 4.2(c)). This qualitatively different behavior is an indicator of the pSk state, as will be illustrated below with the help of real space spin configurations. For $\alpha = 0.6$, χ is finite even at $h_z = 0$. This is consistent with our results reported for Rashba FKLM[52]. Interestingly, the magnitude of χ reduces with increasing h_z, and then again increases before finally vanishing on approach to the sFM state (see Fig. 4.2(d)). The re-entrant behavior of χ shows that the SkX state does not directly lead to sFM state via isolated skyrmions, instead a SQ spiral phase is stabilized at intermediate h_z before the sFM state appears in the strong field limit. This suggests that in contrast to the pSk phase, which can be viewed as a packed arrangement of isolated skyrmions, the SkX phase should be interpreted as a fully cooperative ordered arrangement of spins stable only in the low-field regime. Note that square lattice of skyrmions has also been reported in experiments[56,57]

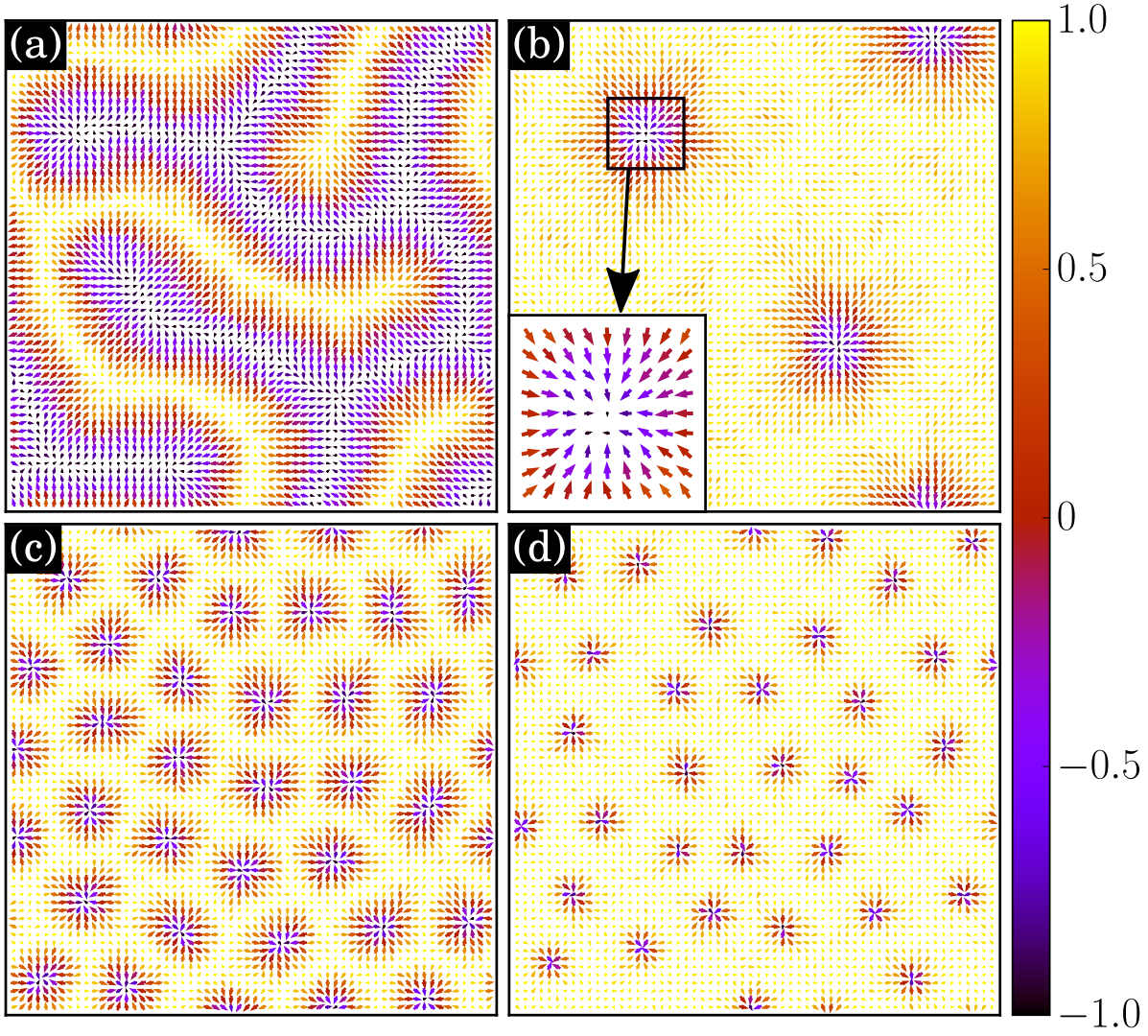

Figure 4.3 Low temperature snapshots of spin configurations for representative values of α and h_z. (a) fDW state at $\alpha = 0.16$, $h_z = 0$, (b) sparse skyrmions at $\alpha = 0.16$, $h_z = 0.036$, (c) pSk at $\alpha = 0.32$, $h_z = 0.13$ and (d) pSk at $\alpha = 0.32$, $h_z = 0.21$.

We find that, within the ZFC protocol at finite temperatures, the domain junctions in the fDW states for small α (see Fig. 4.3(a)) become nucleation centers for skyrmions when magnetic field is applied (see Fig. 4.3(b)). For larger values of α, SQ spiral state gives way to the pSk phase (see Fig. 4.3(c)). For a given α, increasing h_z leads, initially, to a reduction of the size (compare Fig. 4.3 (c) and (d)) and then to a reduction of the number of skyrmions. We have also confirmed that the skyrmion formation in the model is not an artifact of the ZFC protocol, by verifying their existence using the field cooled protocol. However, an important question is whether sSk phase is a thermodynamically stable ground state phase. By comparing energies between increasing- and decreasing-h_z simulations at low temperatures we find that a saturated ferromagnet has lower energy compared to sSk phase. Therefore, sSk is not a stable ground state phase.

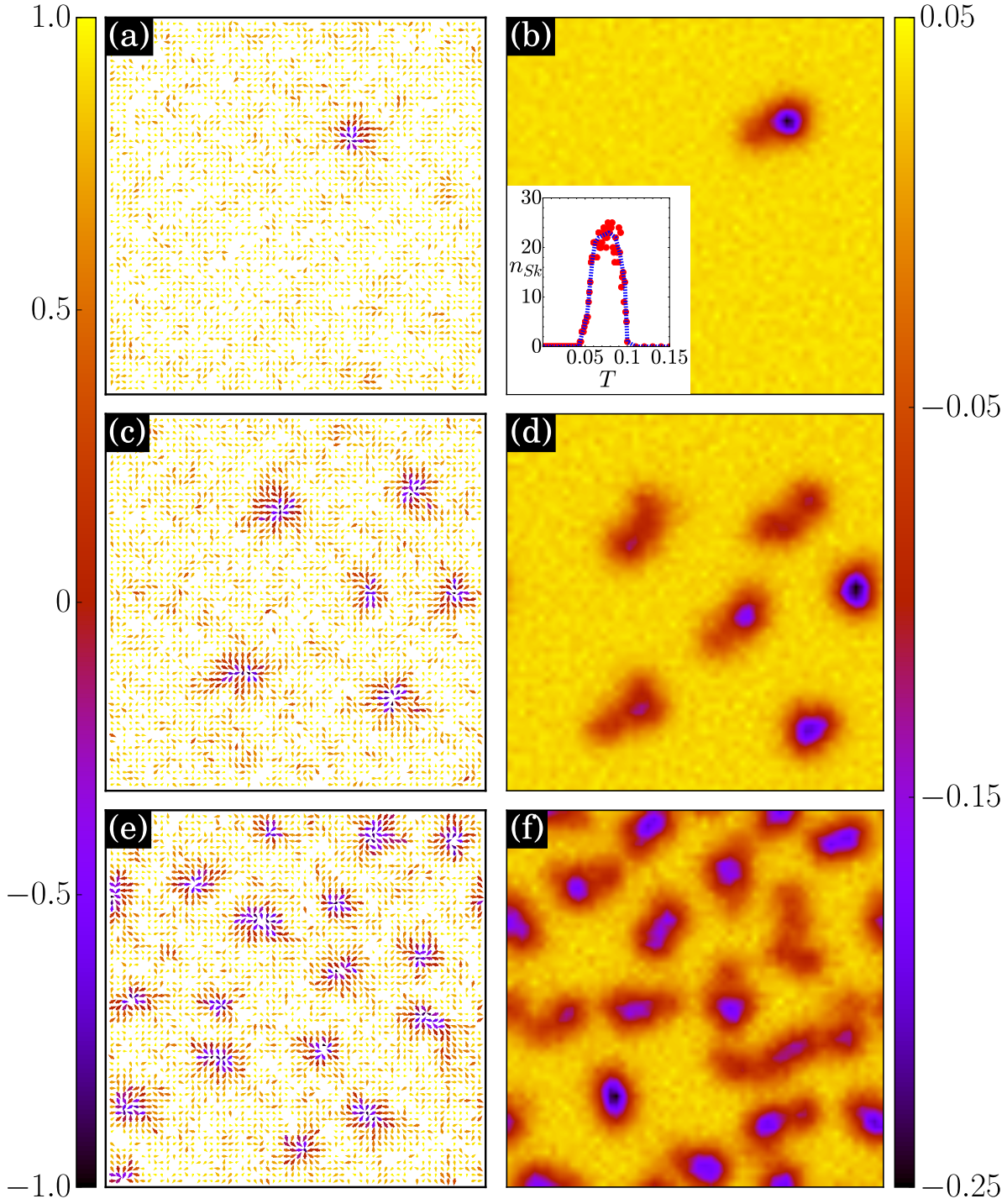

Figure 4.4 Snapshots of typical spin configurations (left column) and corresponding skyrmion density map (right column) taken from Monte Carlo simulations with increasing temperature starting from sFM state at $T = 0.001$. (a)-(b): $T = 0.044$, (c)-(d): $T = 0.052$, (e)-(f): $T = 0.058$. Inset in (b) shows the variation in skyrmion count n_{Sk} with temperature confirming the existence of isolated skyrmions in the ferromagnetic background as finite-T excitations. The calculations are performed on a 60×60 lattice at $\alpha = 0.25$ and $h_z = 0.1$.

We perform additional simulations starting at low temperatures with a sFM con-

figuration and find that isolated skyrmions spontaneously form by simply increasing temperature in simulations (see Fig. 4.4). This suggests that sSk phase is entropically favored over sFM and hence it should be relevant to real systems. We show how the skyrmion count, n_{Sk}, first increases and then decreases upon increasing T (see inset in Fig. 4.4(b)). A possible interpretation is that isolated skyrmions exist as thermal excitations in the ferromagnetic background. However, a confirmation of this requires more systematic exploration of the model at finite temperatures which will be taken up in a separate study. The reduction of n_{Sk} with increasing temperature correlates with the transition of the parent ferromagnetic state into a paramagnetic state.

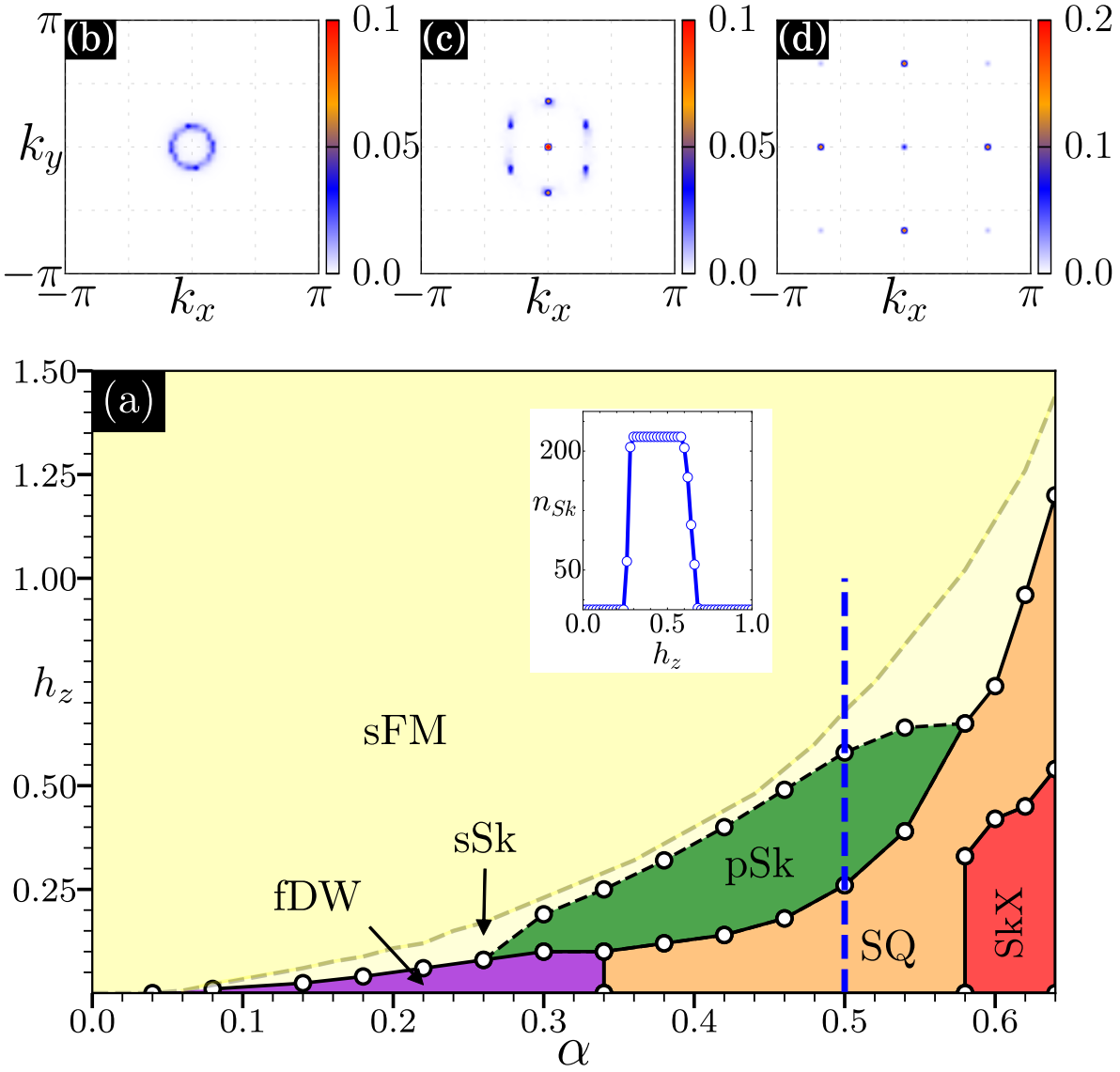

Figure 4.5 (a) Low-temperature phase diagram in the α-h_z plane. SSF for, (b) fDW at $\alpha = 0.22$, $h_z = 0$ (c) pSk at $\alpha = 0.4$, $h_z = 0.16$, and (d) SkX at $\alpha = 0.6$, $h_z = 0.3$. Inset in (a) shows an explicit count of skyrmion centers, n_{Sk}, as a function of h_z along the vertical dashed line at $\alpha = 0.5$. The sSk phase is metastable and sFM is the true groundstate in that parameter regime.

We now summarize the results discussed above in the form of a phase diagram in Fig. 4.5(a). We identify, in addition to the trivial sFM state, (i) a fDW state, (ii) a SQ spiral with peaks in the spin structure factor at $(0,Q)$ or $(Q,0)$, (iii) a pSk state, and (iv) a SkX with square geometry. Furthermore, a metastable sSk region is also indicated in the ground state phase diagram. The boundary between fDW/SQ and sSk/pSk is determined from the sharp increase in the magnitude of χ with increasing h_z (see dashed black lines in Fig. 4.2(a)-(d)). Similarly, the boundary between SkX and SQ is inferred from the variation in χ (see dashed red line in Fig. 4.2(d)). Note that the sharp change in χ is accompanied by a weak but noticeable change in h_z-dependence in magnetization and chirality. The sFM boundary is defined by the saturation of magnetization together with a complete vanishing of chirality and skyrmion density. It is important to mention that the finite-T sSk phase can only be characterized by real-space images showing the presence of isolated skyrmions. Since these isolated skyrmions exist in the ferromagnetic background any bulk indicators, such as SSF, will identify this phase as a ferromagnet. Since the definition of sSk state as a true thermodynamic phase is not possible, we indicate this as a metastable region just below the sFM phase boundary. This is to be understood as the region where isolated skyrmions will emerge at finite temperatures. The boundary between pSk and sSk states is obtained from the h_z dependence of explicit skyrmion count n_{Sk}. In the pSk phase, number of skyrmions do not change upon changing external magnetic field (see inset in Fig. 4.5(a)). Strictly at $T = 0$, the skyrmion count should exhibit a step-like jump to zero. However, at finite T there is a narrow region in h_z displaying a steep decrease in the skyrmion count. A similar gradual decrease in the skyrmion count is expected upon increasing temperature close to the paramagnetic phase boundary. This can be interpreted as a melting of skyrmion lattice via sSk state[58].

The SSF for fDW, pSk and SkX states are displayed in Fig. 4.5(b)-(d), in that order. Circular diffuse pattern for small α (see Fig. 4.5(b)-(c)) matches well with SANS experiments and Fourier transform of LTEM images on MnSi and Co-Zn-Mn alloys[11,15]. We also characterize the pSk state by plotting the number of skyrmions, n_{Sk}, as a function of applied field. A plateau in n_{Sk} is an indicator of the pSk state (see inset in Fig. 4.5(a)).

The SSF in the pSk phase seems to have an hexagonal symmetry. This is expected as close packing of disk-shaped particles will naturally lead to the formation of a triangular lattice. However, on a closer look one finds that the points on the k_y axis are more intense than those located close to the diagonals. We have identified the origin of this asymmetry in the SSF of the $h_z = 0$ state. As mentioned earlier, the spirals in the $h_z = 0$ SQ phase are doubly degenerate with the $(0,Q)$ and $(Q,0)$ having identical energies. In simulations, one of these spirals is spontaneously stablized at low tempera-

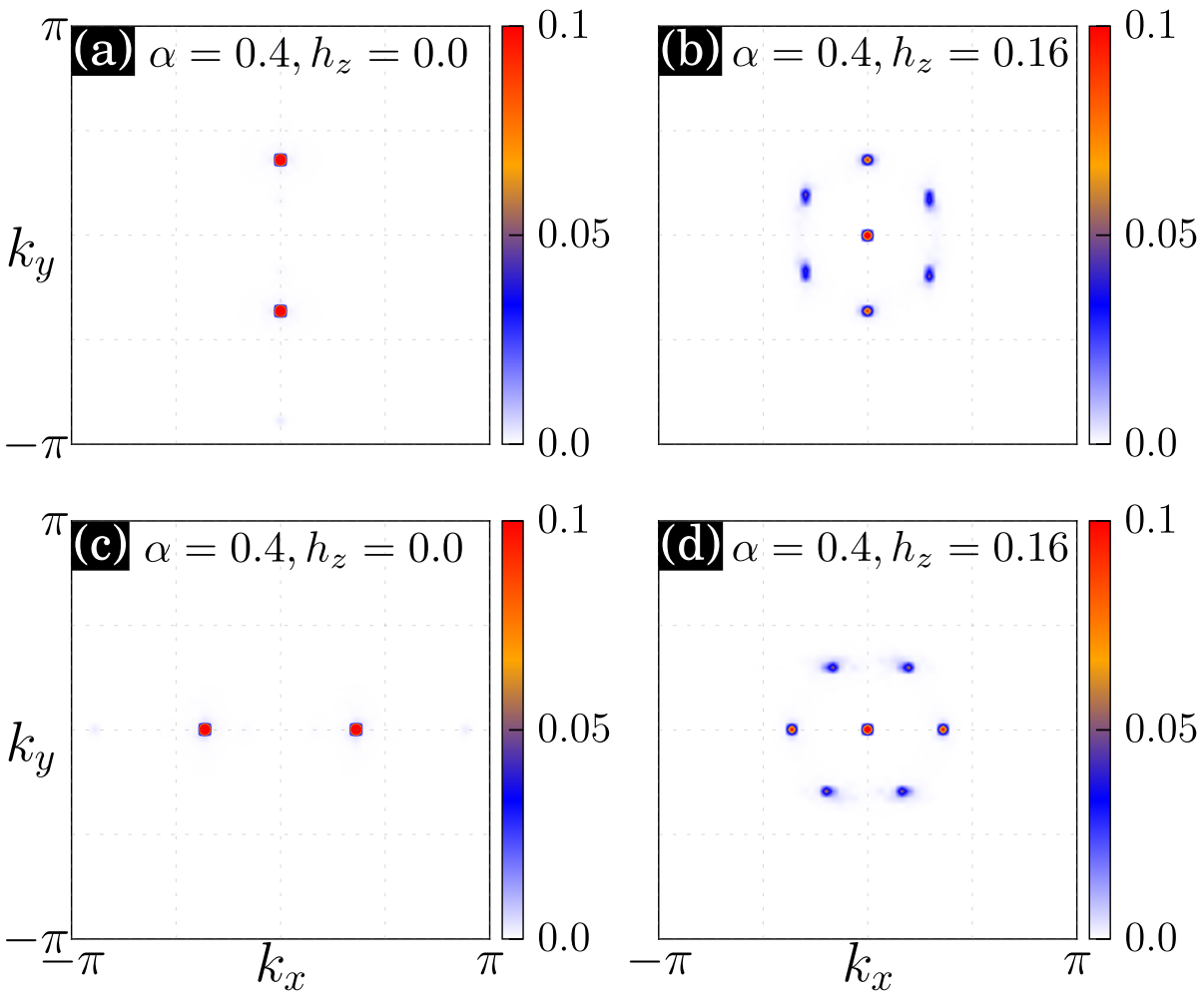

Figure 4.6 SSF for, (a),(c) $h_z = 0$ and (b),(d) $h_z = 0.16$ in two independent simulations. The ground state in the absence of magnetic field is doubly degenerate with $(0, Q)$ and $(Q, 0)$ spirals having equal energy. The hexagonal pattern in SSF at finite magnetic field displaying a slight asymmetry related to the $h_z = 0$ spiral state.

tures. By selecting two such simulations where different SQ states were stabilized, and by increasing h_z in the ZFC protocol we obtain pSk phases characterized by SSF pattern that has a relative 90° rotation (compare Fig. 4.6(b) and (d)). In either case, the peaks located on the k_x or k_y axis are relatively intense. Observation of these asymmetries suggest that formation of an emergent lattice of extended particles residing on, and defined from, the sites of a square lattice cannot form a perfect hexagonal structure. Clearly, in continuum a triangular lattice can spontaneously form with an arbitrary orientations of the three defining axes. On a square lattice, however, the x or y direction becomes a natural choice for one of the axes of the triangular lattice leading to a stronger intensity in the SSF along that direction.

In section Section 4.2. we have shown that the RDE model can account for forma-

tion of skyrmions within an electronic Hamiltonian without the need to write a spin-only model. In section Section 4.3. we explicitly verified that the connection of the electronic Hamiltonian approach to the standard DM interaction based approach to skyrmion formation is understood via the effective spin Hamiltonian derived in our earlier work[52]. While it is well known that itinerant electrons strongly coupled to a magnetic skyrmion background generate anomalous response in transport[59,60], the influence of Rashba coupling on transport properties has been pointed out only recently[46]. For consistency and completeness, in the next section we discuss the effect of magnetic skyrmion states on the electronic properties. This is important to emphasize as in the existing literature it is common practice to use the standard DE model for studying the response of itinerant electrons to unconventional spin textures[29,59,61,62]. The fact that spin-orbit interactions play a crucial role in stabilizing skyrmion textures is commonly ignored when analysing the response of itinerant electrons to skyrmions and the resulting anomalous Hall physics.

4.4 Bott index and topological metalicity

The possibility of finding amorphous analogs of translationally invariant topological insulators has attracted much attention in recent years. Models for disordered topological metallic or insulating states have been proposed[49,63]. A crucial feature of these models is a spatially-dependent pattern of hopping parameters which may not be easy to realize. It is well known that electrons coupled to noncoplanar magnetic patterns experience an effective magnetic field and generate anomalous Hall effect[59,60]. We study how the presence of Rashba coupling in the DE model affects this anomalous response. We present topological characterization of the sSk and pSk states by computing the Bott index $\mathscr{B}$ and the Hall conductivity σ_{xy}. Loring and Hastings first introduced the concept of Bott index in condensed matter systems[64,65]. It is a measure of the incapability of the system to form localized Wannier orbitals from the occupied states[65]. Our motivation to compute the Bott index here is to mathematically confirm the topological aspect of the band structure of electrons in the presence of magnetic skyrmion states. The implementation details of the Bott index calculation can be found in literature[49–51,66]. Nevertheless, for completeness we outline the key steps below. First step is to construct a projection operator out of all the occupied states.

$$P = \sum_{k=1}^{Nel} |\psi_k\rangle\langle\psi_k|, \tag{4.8}$$

where, $|\psi_k\rangle$ is the occupied eigenstate corresponding to the kth eigenvalue E_k, and Nel is the number of electrons in the system. The position coordinates (x_i , y_i) of any lattice site i can be mapped into the spherical co-ordinates (Θ_i , Φ_i) on a torus where $0 \leq \Theta_i < 2\pi$ and $0 \leq \Phi_i < 2\pi$. The next step is to define the projected position operators,

$$\begin{aligned} U &= Pe^{i\Theta}P, \\ V &= Pe^{i\Phi}P, \end{aligned} \tag{4.9}$$

where, Θ and Φ are the diagonal matrices with Θ_i and Φ_i as diagonal elements respectively. The Bott index is given by

$$\mathscr{B} = \frac{1}{2\pi}\mathrm{Im}\Big\{\mathrm{tr}\big[\log(VUV^{\dagger}U^{\dagger})\big]\Big\}, \tag{4.10}$$

For numerical stability of the algorithm, we perform singular value decomposition of the projected position operators U and V following Huang and Liu[50,51]. The Hall conductivity, σ_{xy}, is computed using Kubo-Greenwood formalism as discussed in Section 2.6. Both sSk and pSk states support finite values of σ_{xy} as well as $\mathscr{B}$ (see Fig. 4.7(a), (e)). Both quantities display a change of sign as Fermi level crosses zero. Since the Bott index is an analog of the Chern index for inhomogeneous systems, the aforementioned correspondence between Hall conductivity and Bott index confirms the topological aspect of the skyrmion phases in the RDE model in the same manner as finite Chern index confirms the topological nature of states in translationally invariant systems. Therefore, metallic systems with few or many skyrmions can be classified as topological metals in close analogy with recently proposed hopping-pattern engineered tight-binding models[49,63]. Further, the larger magnitude of σ_{xy} in Fig. 4.7(e) compared to that in Fig. 4.7(a) is due to the increase in the number of skyrmions. In the sparse skyrmion regime, the Hall conductivity increases linearly with the number of skyrmions. The dependence becomes sub-linear on approach to a pSk phase. On the other hand, in pSk phase increasing the number of skyrmions necessarily leads to a decrease in the size of skyrmions. The consequence is larger gauge fields and hence a smaller and quantized Hall conductivity.

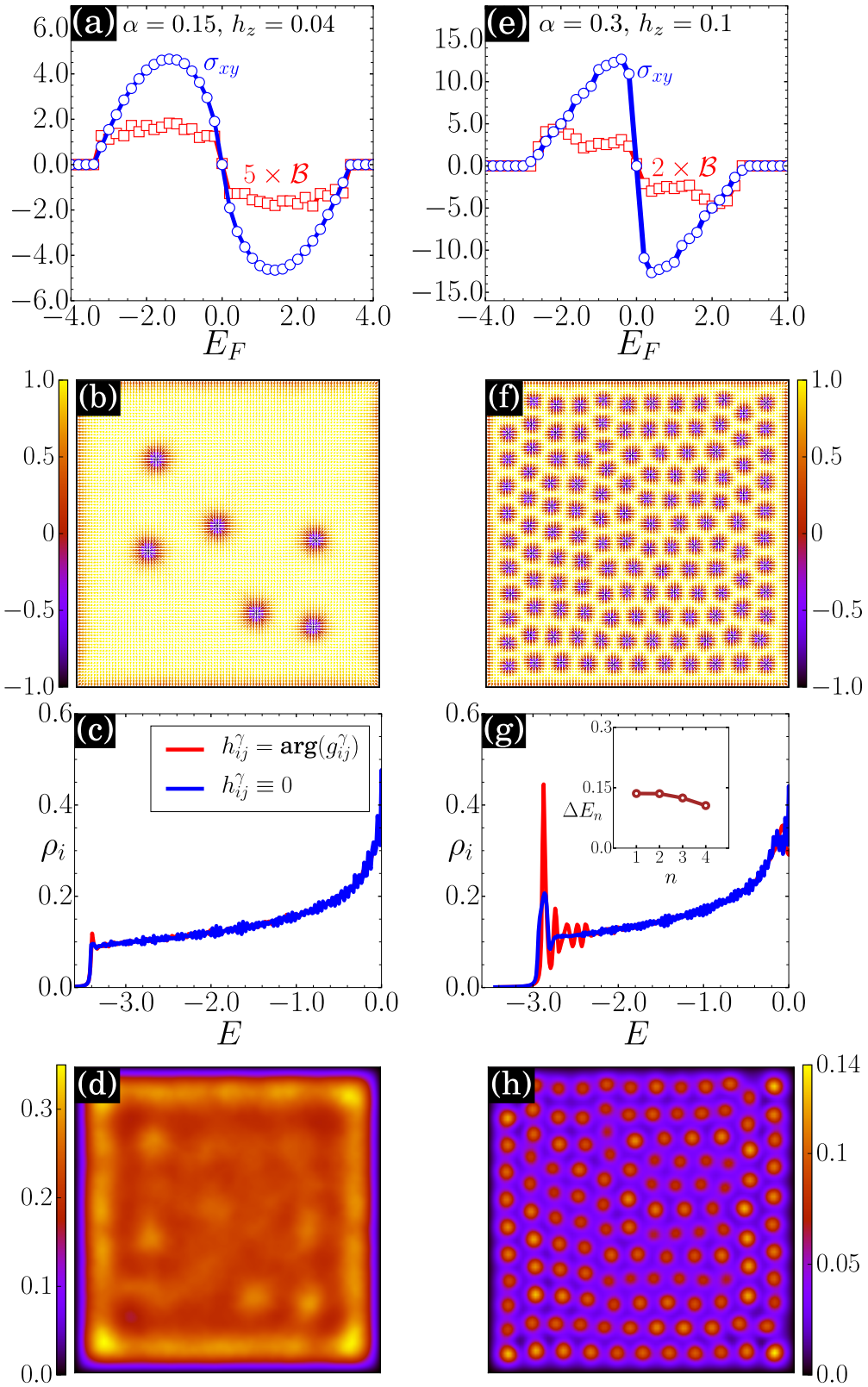

Figure 4.7 (a) Bott index, $\mathscr{B}$, and Hall conductivity, σ_{xy} (in units of e^2/h) as a function of Fermi level E_F, (b) low temperature magnetic configuration obtained via simulations with open boundary conditions, (c) LDOS at skyrmion cores with (red lines) and without (blue lines) local gauge fields, and (d) real space map of LDOS at $E = -3.38$ in absence of local gauge fields ($h_{ij}^{\gamma} \equiv 0$). Panels (a)-(d) display results for $\alpha = 0.15$. (e)-(h) Same quantities as shown in (a)-(d), in that order, for $\alpha = 0.30$. LDOS in panel (h) is shown for $E = -2.87$. The results are obtained on 100×100 lattice using open boundary conditions.

In order to further differentiate between the Rashba modified DE mechanism from the standard DE physics, we calculate local density of states (LDOS), $\rho_i(E) = 1/N \sum_k |\psi_i^k|^2 \delta(E - E_k)$, where ψ_i^k is the amplitude on site i of the single particle eigenstate $|\psi_k\rangle$ corresponding to eigenvalue E_k of the RDE Hamiltonian Eq. (4.2). Lorentzian with broadening parameter 0.01 is used to approximate the Dirac delta function. We find that the skyrmion textures in magnetization have strong implications for the electronic wavefunctions in this unusual metallic phase. We use open boundary conditions for LDOS calculations in order to illustrate the presence of edge modes due to skyrmion-induced gauge fields. Note that the open boundary condition results lead to visible textures in magnetization along the edges. These are a simple consequence of competition between DM-like and ferromagnetic terms in the spin Hamiltonian along the edges and is unrelated to the presence of skyrmions in the bulk. We focus on the LDOS for sites located in skyrmion cores. In the sparse skyrmion case, there is a weak enhancement in LDOS near the band edge (see Fig. 4.7(c)). The effect becomes much pronounced for the packed skyrmion state. Furthermore, periodic modulations as a function of energy become clear (see Fig. 4.7(g)). Inset in Fig. 4.7(g) show the energy difference of two consecutive peaks, ΔE_n, as a function of peak index. There are two possible interpretations of the spikes in LDOS. They can appear either due to the confinement effect, similar to those reported in metallic nanoislands and carbon nanotubes with defect[67,68], or due to effective magnetic flux hidden in the gauge fields. We find a clear approach to disentangle these two effects. Ignoring the phases in the complex hopping parameters g_{ij}^{γ} in the RDE Hamiltonian sets the gauge fields to zero and the resulting model with real hopping parameters contains pure confinement effects. The results of LDOS calculation using $h_{ij}^{\gamma} \equiv 0$ in Eq. (4.2)(blue lines in Fig. 4.7(c), (g)) show that the periodic modulations vanish and only a single peak near the band edge survives. In Fig. 4.7 (d), (h), we plot lattice maps of LDOS for the energy fixed at peak location. The resulting maps display inhomogeneities, and a clear localization of electronic wavefunctions at skyrmion cores for the pSk state (see Fig. 4.7(h)). Note that the depletion of LDOS along the edges visible in Fig. 4.7(d) is related to the magnetic texture along the edges in Fig. 4.7(b), and is not a topological feature. The above analysis proves that, although the confinement effects are present due to change in the magnitude of g_{ij}^{γ}, the oscillations can only be explained by Landau level physics arising from effective magnetic flux hidden in complex g_{ij}^{γ}. This is further confirmed by performing LDOS calculations on ideal skyrmion lattices in next section where we explicitly show quantization of σ_{xy}.

4.5 Emergent gauge fields and Landau levels

In order to confirm this, we set up a calculation where we reduce the disorder effects by designing ideal skyrmion lattice configurations. The elementary skyrmion unit is constructed by defining azimuthal and polar angles for localized spins as[69], $\phi_i = \pi + \tan^{-1}(y_i/x_i)$ and $\theta_i = 2\tan^{-1}(r_s/r_i)e^{\beta(r_s-r_i)}\ \Theta(2r_s - r_i)$, respectively. In the above, $x_i(y_i)$ denote the x (y) coordinate of the site i located at distance r_i from the skyrmion core site, $2r_s$ is the skyrmion radius and Θ denotes the Heaviside step function. We fix $\beta = 0.04$ to ensure similarity of ideal skyrmions with those obtained in HMC and effective Hamiltonian simulations.

We show LDOS calculations for the ideal skyrmion crystals with $r_s = 1.5$ (Fig. 4.8(a)) and $r_s = 2.5$ (Fig. 4.8(e)). We obtain a very clear Landau level distribution for smaller skyrmions (Fig. 4.8(b)), whereas the Landau levels are not well separated for larger skyrmions. Therefore, smaller skyrmions generate stronger effective magnetic fields. As a consequence, quantization of Hall conductivity at integer values is clearly visible in Fig. 4.8(c). Presence of disorder can further effect the separation of Landau levels, leading to an oscillatory behaviour only near the band edges as obtained for simulated skyrmion textures (see Fig. 7(g) in main text). In Fig. 4.8(d) and (h) we show the LDOS maps calculated for the two locations of Fermi energies, corresponding to completely filled first and second Landau levels, marked by the vertical dotted lines in Fig. 4.8(b). LDOS calculations explicitly show the presence of one (Fig. 4.8(d)) and two (Fig. 4.8(h)) edge modes in the two cases. Inset in Fig. 4.8(b) show the energy difference of two consecutive Landau levels as a function of Landau level index. Note that in continuum ΔE_n is independent of n, however in a tight binding model the energy dependence of the density of states leads to an n-dependence in ΔE_n. The dashed line shows ΔE_n for a two dimensional tight-binding model with applied magnetic flux of strength $1/40$ flux quanta per square plaquette. This explicitly confirms that the gauge fields due to skyrmions play the same role as the external magnetic flux. Since the features discussed in this section are unique to the RZ mechanism proposed in this work, they serve as testable predictions for the presence of the mechanism in thin films of magnetic metals.

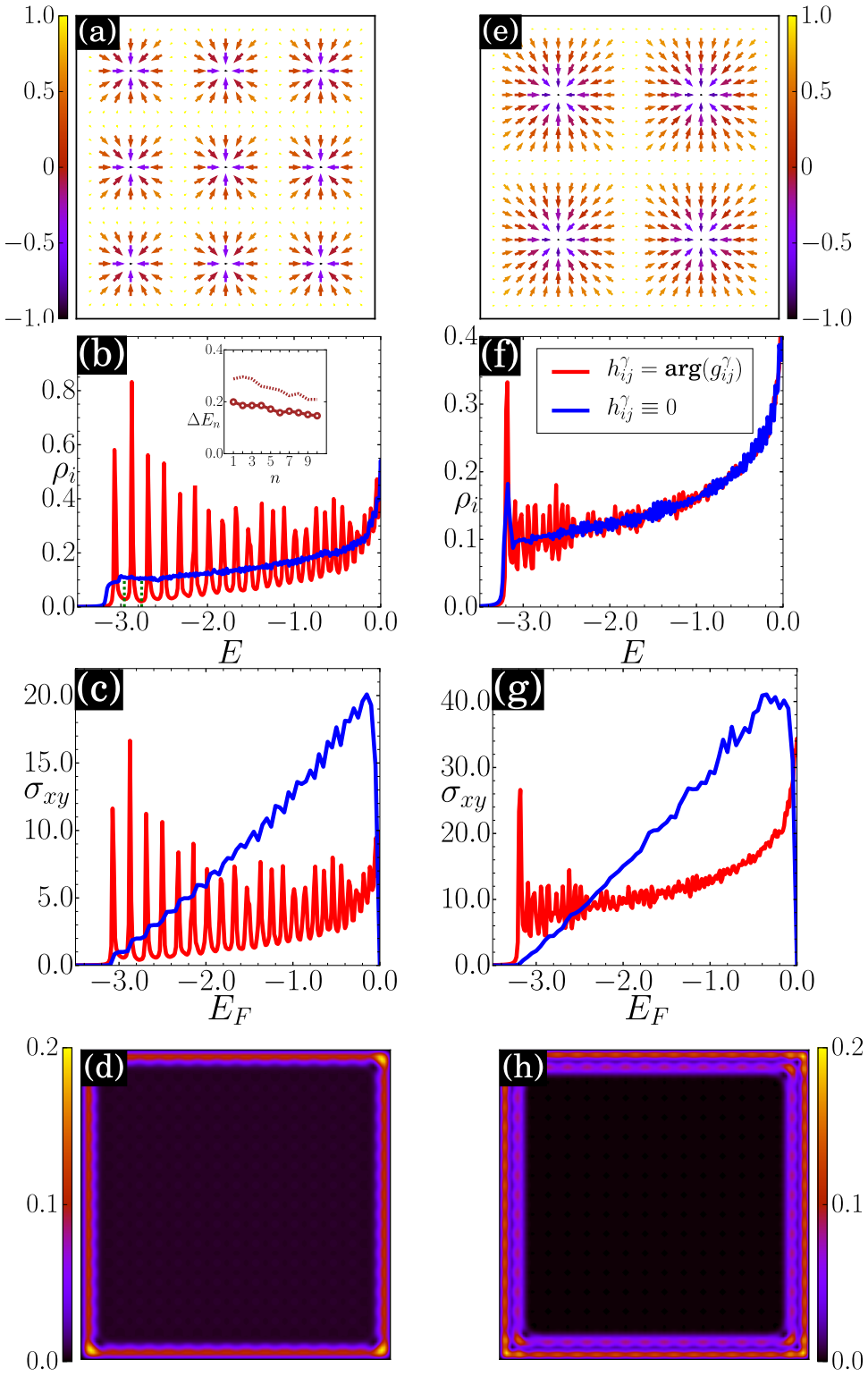

Figure 4.8 Perfect skyrmion crystal configuration with, (a) $r_s = 1.5$ and (e) $r_s = 2.5$. Panels (b) and (f) display LDOS in skyrmion cores, with (red lines) and without (blue lines) gauge fields, for configurations shown in (a) and (e), respectively. Panels (c) and (g) show the variation of Hall conductivity with Fermi energy for configurations displayed in (a) and (e), respectively. LDOS maps at $E_F = -2.95$ (panel (d)) and $E_F = -2.75$ (panel (h)) (marked by green dotted lines in panel (b)). One edge mode per filled Landau level is easily identified in panels (d) and (h). The calculations are performed on lattice sizes 112×112 (for $r_s = 1.5$) and $N = 110 \times 110$ (for $r_s = 2.5$). We use $\alpha = 0.2$ for all calculations shown in this figure.

4.6 Importance of consistent treatment

In order to clearly emphasize the importance of a consistent treatment of Rashba coupling in the DE mechanism of skyrmion formation, we demonstrate the qualitative difference between LDOS maps obtained without and with the Rashba term. Once again we take the typical configurations from sSk and pSk phases for this demonstration. For both sSk and pSk states, LDOS maps calculated by setting $\alpha = 0$ display a depletion of electron density near skyrmion cores (see Fig. 4.9 (a),(c)). When the consistent calculations are performed by setting the value of α equal to that used for obtaining the skyrmion textures an opposite qualitative picture emerges. The skyrmion cores tend to behave as attraction centers for the electronic charge (see Fig. 4.9 (b),(d)). This change of qualitative behaviour is a clear sign of caution for the calculations performed within conventional DE approach.

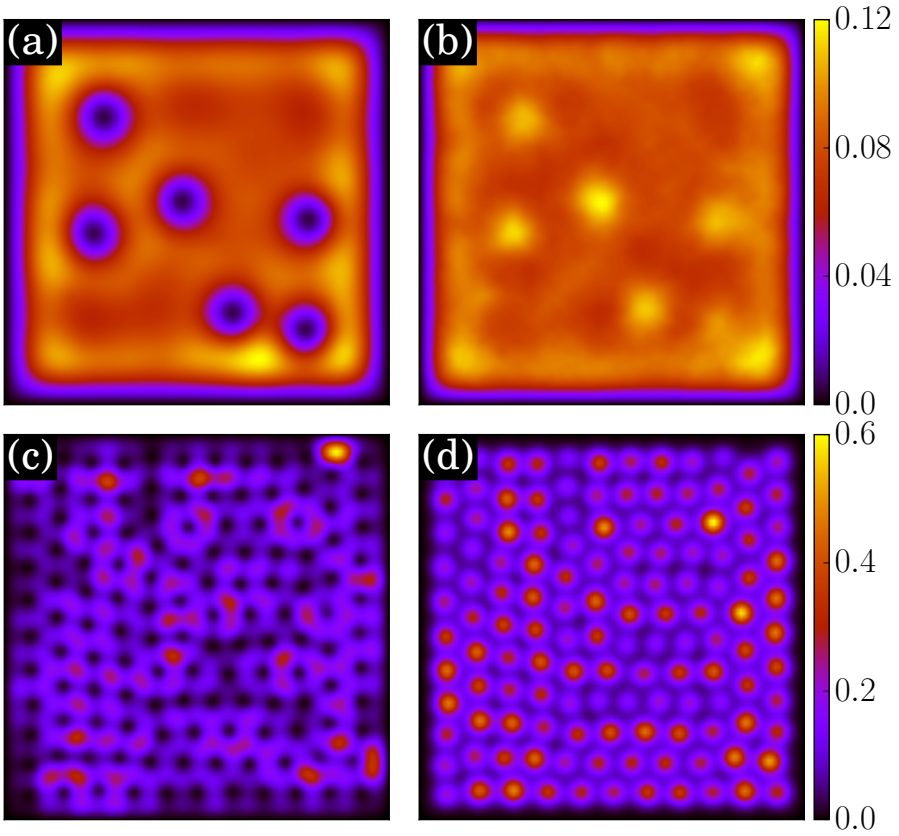

Figure 4.9 For sSk configuration obtained at $\alpha = 0.15$ and $h_Z = 0.04$ (shown in Fig. 4.7(b)): LDOS map for energy near the band edge, (a) in an inconsistent electronic model with $\alpha = 0.0$ and (b) for the consistent calculation with $\alpha = 0.15$ in the itinerant model. For pSk configuration shown in Fig. 4.7(f): LDOS maps within, (c) inconsistent calculation with $\alpha = 0.0$ and (d) the consistent calculation with $\alpha = 0.30$. Note the qualitative difference between the left and right columns: while the skyrmion cores behave as repulsive centers for electrons in $\alpha = 0$ calculations, they become attractive centers in the consistent calculations.

4.7 Conclusion

Double exchange mechanism provides a basis for understanding ferromagnetism in a variety of metallic magnets. We have uncovered a new aspect associated with the classic DE mechanism by including the effect of Rashba SOC and Zeeman field in the DE model. An explicit demonstration of the existence of nanoscale skyrmions in an electronic model with no direct spin-spin interactions is presented. In the presence of magnetic field, at finite temperatures, phases with sparse as well as packed skyrmions are stabilized. While the pSk states are shown to be true ground states of the model, the sparse skyrmions are metastable in the ground state but occur at finite temperature as excitations of the ferromagnet. The circular patterns in the SSF are remarkably similar to those reported in the SANS experiments on Co-Zn-Mn alloys and MnSi[15]. The corresponding real-space images, representative of fDW states, are also in agreement with the LTEM images on FeGe, Co-Zn-Mn and transition metal multilayers[8–10,12,13,15,26,47,48]. In order to emphasize the similarity, we show below representative images from LTEM and SANS experiments and compare with the images obtained in our calculations.

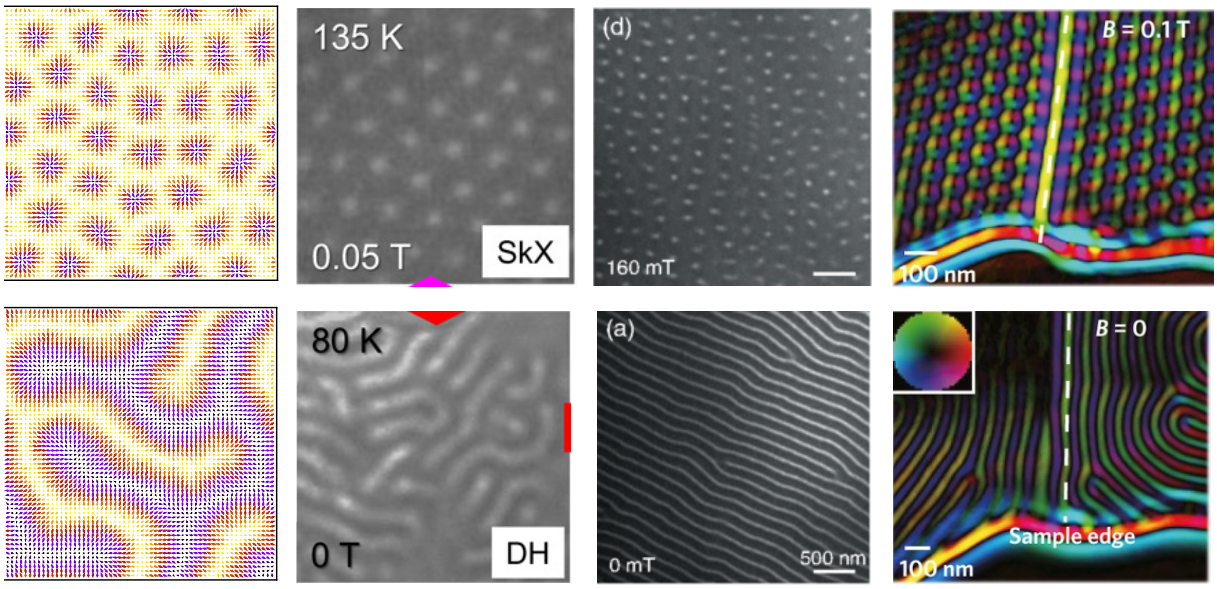

Figure 4.10 Qualitative comparison between spin configurations from our simulations (first column) with LTEM images from different experimental papers (Column 2[47], Column 3[26], column 4[12]. The lower (upper) row is in absence (presence) of the external magnetic field.

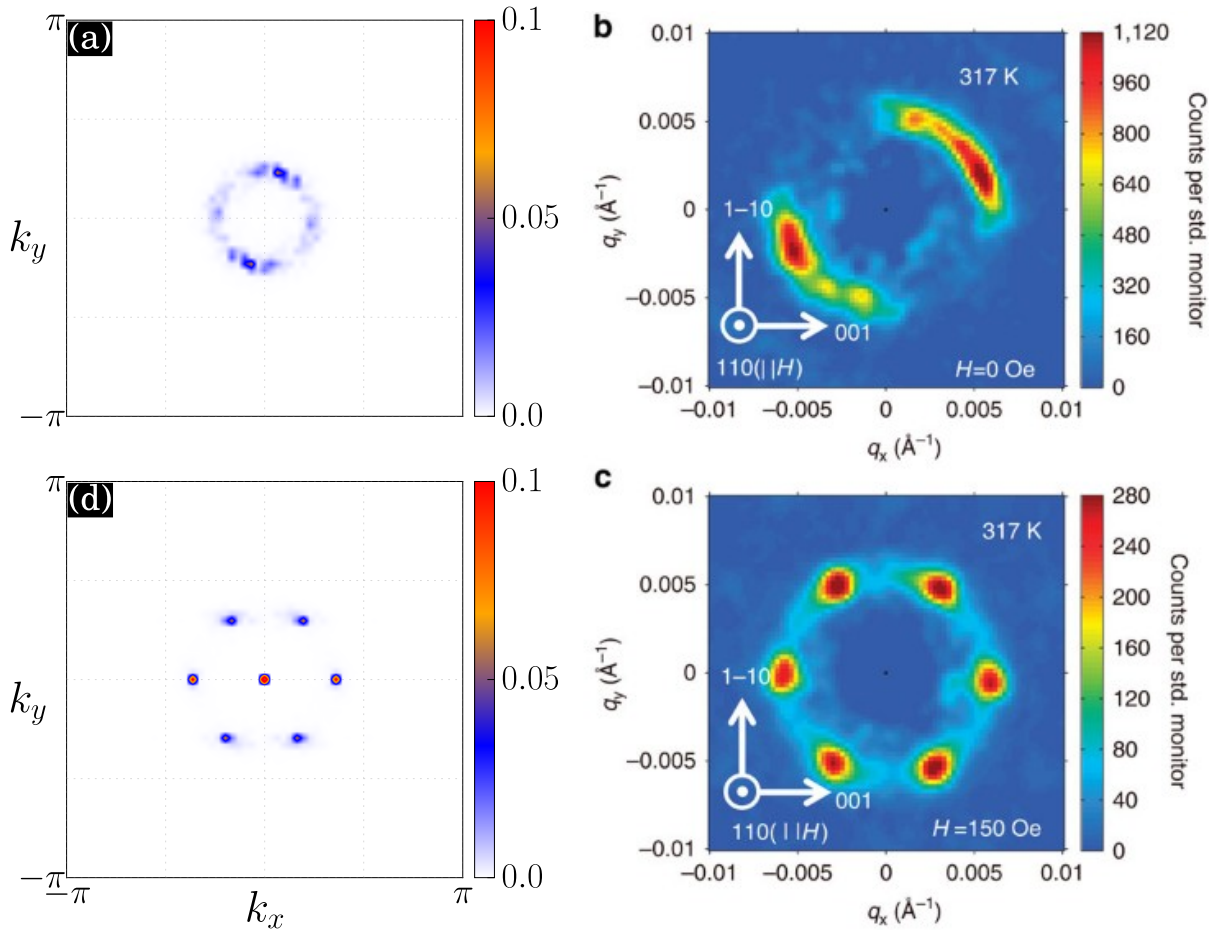

Figure 4.11 Comparison between spin structure factor obtained in our simulations (left column) with SANS image from experimental study[48] (right column).

The origin of the skyrmion states lies in the anisotropy terms of the DM and pseudo-dipolar form that become apparent in the effective Hamiltonian derived from the RDE model. In addition to a hexagonal packed lattice of skyrmions, we also find a qualitatively different square lattice skyrmion crystal stable for larger values of α. Hall conductivity and Bott index calculations are presented to explicitly demonstrate that the skyrmion states are examples of amorphous topological metals. Analogy with recently proposed tight-binding models for amorphous topological metals and insulators is also discussed. The LDOS calculations are presented in order to emphasize the importance of Rashba coupling in the DE mechanism that is commonly used for analysing the influence of magnetic textures on electronic transport. The characteristic oscillations in LDOS as a function of energy can be directly measured in experiments via dI/dV spectra. Such dI/dV measurements can also be used to estimate the strength of Rashba coupling in a metal with the help of a careful modelling of the data.

Bibliography

[1] A. Fert, N. Reyren, and V. Cros, Nat. Rev. Mater. **2**, 17031 (2017).

[2] R. Wiesendanger, Nat. Rev. Mater. **1**, 16044 (2016).

[3] A. Fert, V. Cros, and J. Sampaio, Nat. Nanotechnol. **8**, 152 (2013).

[4] N. Nagaosa and Y. Tokura, Nat. Nanotechnol. **8**, 899 (2013).

[5] B. Göbel, A. Mook, J. Henk, and I. Mertig, Phys. Rev. B **99**, 020405 (2019).

[6] A. N. Bogdanov and C. Panagopoulos, Phys. Today **73**, 44 (2020).

[7] B. Dupé, M. Hoffmann, C. Paillard, and S. Heinze, Nat. Commun. **5**, 4030 (2014).

[8] S. D. Pollard, J. A. Garlow, J. Yu, Z. Wang, Y. Zhu, and H. Yang, Nat. Commun. **8**, 14761 (2017).

[9] A. Soumyanarayanan, M. Raju, A. L. Gonzalez Oyarce, A. K. C. Tan, M.-Y. Im, A. Petrović, P. Ho, K. H. Khoo, M. Tran, C. K. Gan, F. Ernult, and C. Panagopoulos, Nat. Mater. **16**, 898 (2017).

[10] N. Romming, C. Hanneken, M. Menzel, J. E. Bickel, B. Wolter, K. von Bergmann, A. Kubetzka, and R. Wiesendanger, Science **341**, 636 (2013).

[11] X. Z. Yu, N. Kanazawa, W. Z. Zhang, T. Nagai, T. Hara, K. Kimoto, Y. Matsui, Y. Onose, and Y. Tokura, Nat. Commun. **3**, 988 (2012).

[12] X. Z. Yu, N. Kanazawa, Y. Onose, K. Kimoto, W. Z. Zhang, S. Ishiwata, Y. Matsui, and Y. Tokura, Nat. Mater. **10**, 106 (2011).

[13] X. Zhao, C. Jin, C. Wang, H. Du, J. Zang, M. Tian, R. Che, and Y. Zhang, Proc. Natl. Acad. Sci. U. S. A. **113**, 4918 (2016).

[14] S. Meyer, M. Perini, S. von Malottki, A. Kubetzka, R. Wiesendanger, K. von Bergmann, and S. Heinze, Nat. Commun. **10**, 3823 (2019).

[15] A. Tonomura, X. Yu, K. Yanagisawa, T. Matsuda, Y. Onose, N. Kanazawa, H. S. Park, and Y. Tokura, Nano Lett. **12**, 1673 (2012).

[16] M. Hirschberger, T. Nakajima, S. Gao, L. Peng, A. Kikkawa, T. Kurumaji, M. Kriener, Y. Yamasaki, H. Sagayama, H. Nakao, K. Ohishi, K. Kakurai, Y. Taguchi, X. Yu, T.-h. Arima, and Y. Tokura, Nat. Commun. **10**, 5831 (2019).

[17] C. Jin, Z.-A. Li, A. Kovács, J. Caron, F. Zheng, F. N. Rybakov, N. S. Kiselev, H. Du, S. Blügel, M. Tian, Y. Zhang, M. Farle, and R. E. Dunin-Borkowski, Nat. Commun. **8**, 15569 (2017).

[18] S. Mühlbauer, B. Binz, F. Jonietz, C. Pfleiderer, A. Rosch, A. Neubauer, R. Georgii, and P. Böni, Science **323**, 915 (2009).

[19] K. M. Song, J.-S. Jeong, B. Pan, X. Zhang, J. Xia, S. Cha, T.-E. Park, K. Kim, S. Finizio, J. Raabe, J. Chang, Y. Zhou, W. Zhao, W. Kang, H. Ju, and S. Woo, Nat. Electron. **3**, 148 (2020).

[20] J. Sampaio, V. Cros, S. Rohart, A. Thiaville, and A. Fert, Nat. Nanotechnol. **8**, 839 (2013).

[21] A. K. Nayak, V. Kumar, T. Ma, P. Werner, E. Pippel, R. Sahoo, F. Damay, U. K. Rößler, C. Felser, and S. S. P. Parkin, Nature **548**, 561 (2017).

[22] C. Pfleiderer, D. Reznik, L. Pintschovius, H. v. Löhneysen, M. Garst, and A. Rosch, Nature **427**, 227 (2004).

[23] J. Jena, B. Göbel, T. Ma, V. Kumar, R. Saha, I. Mertig, C. Felser, and S. S. P. Parkin, Nat. Commun. **11**, 1115 (2020).

[24] P.-J. Hsu, L. Rózsa, A. Finco, L. Schmidt, K. Palotás, E. Vedmedenko, L. Udvardi, L. Szunyogh, A. Kubetzka, K. von Bergmann, and R. Wiesendanger, Nat. Commun. **9**, 1571 (2018).

[25] X. Z. Yu, W. Koshibae, Y. Tokunaga, K. Shibata, Y. Taguchi, N. Nagaosa, and Y. Tokura, Nature **564**, 95 (2018).

[26] T. Nagase, M. Komatsu, Y. G. So, T. Ishida, H. Yoshida, Y. Kawaguchi, Y. Tanaka, K. Saitoh, N. Ikarashi, M. Kuwahara, and M. Nagao, Phys. Rev. Lett. **123**, 137203 (2019).

[27] U. K. Rößler, A. N. Bogdanov, and C. Pfleiderer, Nature **442**, 797 (2006).

[28] J. P. Chen, D.-W. Zhang, and J. M. Liu, Sci. Rep. **6**, 29126 (2016).

[29] N. Mohanta, E. Dagotto, and S. Okamoto, Phys. Rev. B **100** (2019), 10.1103/PhysRevB.100.064429.

[30] J. Zang, M. Mostovoy, J. H. Han, and N. Nagaosa, Phys. Rev. Lett. **107**, 136804 (2011).

[31] J. Iwasaki, A. J. Beekman, and N. Nagaosa, Phys. Rev. B **89**, 064412 (2014).

[32] S. G. Yang, Y. H. Liu, and J. H. Han, Phys. Rev. B **94**, 054420 (2016), arXiv:1512.04153 .

[33] X. X. Zhang, A. S. Mishchenko, G. De Filippis, and N. Nagaosa, Phys. Rev. B **94**, 174428 (2016), arXiv:1608.05902 .

[34] A. Farrell and T. Pereg-Barnea, Phys. Rev. B **89**, 035112 (2014).

[35] R. Ozawa, S. Hayami, and Y. Motome, Phys. Rev. Lett. **118**, 147205 (2017).

[36] Z. Wang, Y. Su, S.-Z. Lin, and C. D. Batista, Phys. Rev. Lett. **124**, 207201 (2020).

[37] W. Jiang, P. Upadhyaya, W. Zhang, G. Yu, M. B. Jungfleisch, F. Y. Fradin, J. E. Pearson, Y. Tserkovnyak, K. L. Wang, O. Heinonen, S. G. Te Velthuis, and A. Hoffmann, Science (80-.). **349**, 283 (2015).

[38] N. Mathur, M. J. Stolt, and S. Jin, APL Mater. **7**, 120703 (2019).

[39] C. Zener, Phys. Rev. **82**, 403 (1951).

[40] P. W. Anderson and H. Hasegawa, Phys. Rev. **100**, 675 (1955).

[41] P. G. de Gennes, Phys. Rev. **118**, 141 (1960).

[42] E. Dagotto, *Nanoscale Phase Separation and Collosal Magnetoresistance* (Springer Berlin/Heidelberg, Berlin, 2002).

[43] K. Pradhan and S. K. Das, Sci. Rep. **7**, 9603 (2017).

[44] A. Yaouanc, P. Dalmas de Réotier, B. Roessli, A. Maisuradze, A. Amato, D. Andreica, and G. Lapertot, Phys. Rev. Res. **2**, 013029 (2020).

[45] D. Bombor, C. G. F. Blum, O. Volkonskiy, S. Rodan, S. Wurmehl, C. Hess, and B. Büchner, Phys. Rev. Lett. **110**, 066601 (2013).

[46] S.-S. Zhang, H. Ishizuka, H. Zhang, G. B. Halász, and C. D. Batista, Phys. Rev. B **101**, 024420 (2020).

[47] K. Karube, J. S. White, D. Morikawa, C. D. Dewhurst, R. Cubitt, A. Kikkawa, X. Yu, Y. Tokunaga, T.-h. Arima, H. M. RΩ*nnow*, *Y. Tokura*, *and Y. Taguchi*, *Sci.Adv.* **4**, *eaar*7043(2018).*Y. Tokunaga*, *X. Z. Yu*, *J. S. White*, *H*

[48] A. Agarwala and V. B. Shenoy, Phys. Rev. Lett. **118**, 236402 (2017).

[50] H. Huang and F. Liu, Phys. Rev. Lett. **121**, 126401 (2018).

[51] H. Huang and F. Liu, Phys. Rev. B **98**, 125130 (2018).

[52] D. S. Kathyat, A. Mukherjee, and S. Kumar, Phys. Rev. B **102**, 075106 (2020).

[53] S. Kumar and P. Majumdar, Eur. Phys. J. B **50**, 571 (2006).

[54] A. Mukherjee, N. D. Patel, C. Bishop, and E. Dagotto, Phys. Rev. E **91**, 063303 (2015).

[55] S. Banerjee, J. Rowland, O. Erten, and M. Randeria, Phys. Rev. X **4**, 031045 (2014).

[56] N. D. Khanh, T. Nakajima, X. Yu, S. Gao, K. Shibata, M. Hirschberger, Y. Yamasaki, H. Sagayama, H. Nakao, L. Peng, K. Nakajima, R. Takagi, T. hisa Arima, Y. Tokura, and S. Seki, Nat. Nanotechnol. **15**, 444 (2020), arXiv:2003.00626 .

[57] T. Tanigaki, K. Shibata, N. Kanazawa, X. Yu, Y. Onose, H. S. Park, D. Shindo, and Y. Tokura, Nano Lett. **15**, 5438 (2015).

[58] Y. Nishikawa, K. Hukushima, and W. Krauth, Phys. Rev. B **99**, 064435 (2019), arXiv:1710.11095 .

[59] B. Göbel, A. Mook, J. Henk, and I. Mertig, Eur. Phys. J. B **91**, 179 (2018), arXiv:1806.06958 .

[60] J. Zang, M. Mostovoy, J. H. Han, and N. Nagaosa, Phys. Rev. Lett. **107**, 136804 (2011).

[61] K. Hamamoto, M. Ezawa, and N. Nagaosa, Phys. Rev. B - Condens. Matter Mater. Phys. **92**, 115417 (2015).

[62] B. Göbel, A. Mook, J. Henk, and I. Mertig, Phys. Rev. B **95**, 094413 (2017), arXiv:1702.06727 .

[63] Y.-B. Yang, T. Qin, D.-L. Deng, L.-M. Duan, and Y. Xu, Phys. Rev. Lett. **123**, 076401 (2019).

[64] T. A. Loring and M. B. Hastings, EPL (Europhysics Lett. **92**, 67004 (2010).

[65] M. B. Hastings and T. A. Loring, Ann. Phys. (N. Y). **326**, 1699 (2011).

[66] D. Toniolo, Phys. Rev. B **98**, 235425 (2018), arXiv:1708.05916 .

[67] H.-T. Yang, J.-W. Chen, L.-F. Yang, and J. Dong, 10.1103/PhysRevB.71.085402.

[68] M. V. Rastei, B. Heinrich, L. Limot, P. A. Ignatiev, V. S. Stepanyuk, P. Bruno, and J. P. Bucher, Phys. Rev. Lett. **99**, 246102 (2007).

[69] F. Tejo, A. Riveros, J. Escrig, K. Y. Guslienko, and O. Chubykalo-Fesenko, Sci. Rep. **8**, 6280 (2018).

5

Antiskyrmions and Bloch skyrmions in Dresselhaus double exchange metals

In this chapter, we explicitly show that inclusion of Dresselhaus spin orbit coupling and Zeeman field stabilizes sparse and packed antiskyrmions in the paradigmatic double exchange model. We provide a simple understanding of antiskyrmion phases with the help of an effective spin model derived from the microscopic electronic Hamiltonian. We emphasize the role of electronic band structure in deciding the type of skyrmion textures in the spin-orbit modified double exchange model.

5.1 Introduction

Topological magnetic textures like skyrmions and antiskyrmions characterized by opposite winding numbers of ± 1 can carry different, but complementary binary information that can be used for building future information storage and processing devices[1–5]. Achieving small size and increasing the stability of these magnetic textures over a wide temperature-magnetic field phase space are also future challenges. These textures can be stabilized in systems with antisymmetric exchange, i.e., Dzyaloshinskii Moriya interaction (DMI) due to large spin-orbit coupling (SOC)[6–10]. Other than DMI, frustrated interactions due to long-ranged exchange mediated by itinerant electrons[11–14] can also lead to such magnetic states. Current theories suggest that while skyrmions are stabilized by isotropic DMI, stabilization of antiskyrmions require anisotropic DMI[15–17] or dipolar interactions[18]. Appearance of skyrmions has been observed with various techniques, such as small angle neutron scattering (SANS) and Lorentz transmission electron microscopy (LTEM) in bulk as well as in thin films of a variety of chiral magnets[19–27]. On the other hand, antiskyrmions have been observed in bulk materials[28–30] but not in thin films. Antiskyrmions offer some advantage over skyrmions in that they can under some conditions move in the direction of an applied spin polarized current, while skyrmions necessarily move at an angle[16]. Lifetime of antiskyrmions at room temperature is found to be longer than the skyrmions[31,32].

We have shown in previous chapters that the Rashba Double Exchange (RDE) model in the presence of Zeeman field leads to states hosting nano-skyrmions[33,34]. Materials hosting antiskyrmions like $Mn_{1.4}Pt_{0.9}Pd_{0.1}Sn$, $Mn_{1.4}PtSn$, $Mn_2Rh_{0.95}Ir_{0.05}Sn$ are usually inverse Heusler metals lacking a center of inversion. In addition there is large spin-orbit coupling associated with heavy elements, such as Pt and Sn, in these compounds. Therefore an appropriate description of these metallic magnets can be in terms of a double exchange model modified by Dresselhaus SOC. Here, we show that the Dresselhaus DE (DDE) model in the Zeeman field's presence leads to stabilization of antiskyrmion states. We explicitly demonstrate the appearance of antiskyrmions using the state-of-the-art hybrid Monte Carlo (HMC) simulations. For the comprehensive understanding of the origin as well as stability of these spin textures, we also study an effective spin Hamiltonian. We compare and differentiate between the filamentary domain wall (fDW) phases arising in Rashba and Dresselhaus metals.

5.2 Spin-fermion model and hybrid Monte Carlo results

We start with the ferromagnetic Kondo lattice model (FKLM) in the presence of Dresselhaus SOC, described by the Hamiltonian,

$$\begin{aligned} H &= -t\sum_{\langle ij\rangle,\sigma}(c^{\dagger}_{i\sigma}c_{j\sigma}+\text{H.}c.)+\lambda\sum_{i}[\text{i}(c^{\dagger}_{i\downarrow}c_{i+x\uparrow}+c^{\dagger}_{i\uparrow}c_{i+x\downarrow}) \\ &\quad +(c^{\dagger}_{i\downarrow}c_{i+y\uparrow}-c^{\dagger}_{i\uparrow}c_{i+y\downarrow})+\text{H.}c.]-J_H\sum_{i}\mathbf{S}_i\cdot\mathbf{s}_i. \end{aligned} \tag{5.1}$$

Here, $c_{i\sigma}(c^{\dagger}_{i\sigma})$ annihilates (creates) an electron at site i with spin σ, $\langle ij\rangle$ implies that i and j are nearest neighbor (nn) sites. λ and J_H denote the strengths of Dresselhaus and Hund's coupling, respectively. $\mathbf{s_i}$ is the electronic spin operator at site i, and $\mathbf{S}_i$, with $|\mathbf{S}_i|=1$, denotes the localized spin at that site. We parameterize $t=(1-\alpha)t_0$ and $\lambda=\alpha t_0$ and set $t_0=1$ as the reference energy scale. Assuming large J_H and taking the double-exchange approximation, we obtain the DDE Hamiltonian,

$$H_{\text{DDE}} = \sum_{\langle ij\rangle,\gamma}[g^{\gamma}_{ij}d^{\dagger}_i d_j+\text{H.c.}]-h_z\sum_i S^z_i, \tag{5.2}$$

where, $d_i(d^{\dagger}_i)$ annihilates (creates) an electron at site i with spin parallel to the localized spin. The second term represents the Zeeman coupling of local moments to external magnetic field of strength h_z. Site $j=i+\gamma$ is the nn of site i along spatial direction $\gamma=x,y$. The projected hopping $g^{\gamma}_{ij}=t^{\gamma}_{ij}+\lambda^{\gamma}_{ij}$ depend on the orientations of the local moments $\mathbf{S}_i$ and $\mathbf{S}_j$,

$$\begin{aligned} t^{\gamma}_{ij} &= -t\left[\cos(\frac{\theta_i}{2})\cos(\frac{\theta_j}{2})+\sin(\frac{\theta_i}{2})\sin(\frac{\theta_j}{2})e^{-\text{i}(\phi_i-\phi_j)}\right], \\ \lambda^{x}_{ij} &= \text{i}\lambda\left[\sin(\frac{\theta_i}{2})\cos(\frac{\theta_j}{2})e^{-\text{i}\phi_i}+\cos(\frac{\theta_i}{2})\sin(\frac{\theta_j}{2})e^{\text{i}\phi_j}\right], \\ \lambda^{y}_{ij} &= \lambda\left[\sin(\frac{\theta_i}{2})\cos(\frac{\theta_j}{2})e^{-\text{i}\phi_i}-\cos(\frac{\theta_i}{2})\sin(\frac{\theta_j}{2})e^{\text{i}\phi_j}\right], \end{aligned} \tag{5.3}$$

where, θ_i (ϕ_i) denotes the polar (azimuthal) angle for localized spin $\mathbf{S}_i$.

Comparing Eq.(5.1) with the Hamiltonian in Chapter 4 we can see that the form of the Hamiltonians is same, only difference is the interchange of the SOC terms along x and y directions. As a consequence of that we get same Eq. (5.2) as in Eq. (4.2) but notice the interchange of λ^{x}_{ij} and λ^{y}_{ij} expressions in Eq.(5.3) as compared to Eq. (4.3) in Chapter 4. We can anticipate that the phase diagram and the ground states in DDE model will be similar as obtained in Chapter 4 but nature of the magnetic textures could be different.

We study the DDE Hamiltonian using numerically exact hybrid Monte Carlo (HMC) simulations as discussed in Section 2.7.3. Presence of skyrmions or antiskyrmions is inferred via local skyrmion density[6],

$$\chi_i = \frac{1}{8\pi}[\mathbf{S}_i \cdot (\mathbf{S}_{i+x} \times \mathbf{S}_{i+y}) + \mathbf{S}_i \cdot (\mathbf{S}_{i-x} \times \mathbf{S}_{i-y})]. \tag{5.4}$$

Total skyrmion density is defined as, $\chi = \sum_i \chi_i$. We also compute the spin structure factor (SSF),

$$S_f(\mathbf{q}) = \frac{1}{N^2} \sum_{ij} \mathbf{S}_i \cdot \mathbf{S}_j \; e^{-i\mathbf{q}\cdot(\mathbf{r}_i - \mathbf{r}_j)}, \tag{5.5}$$

and the relevant component of vector chirality η as,

$$\eta = \frac{1}{N} \sum_i -(\mathbf{S}_i \times \mathbf{S}_{i+x}) \cdot \hat{x} + (\mathbf{S}_i \times \mathbf{S}_{i+y}) \cdot \hat{y}. \tag{5.6}$$

Averaging of all quantities over MC steps is implicitly assumed, unless stated otherwise.

Results obtained via HMC simulations for two representative values of α are shown in Fig. 5.1. Upon increasing h_z, Magnetization, $M_z = \frac{1}{N}\sum_i S_i^z$, increases and η decreases. The magnitude of χ initially increases with applied field, and then decreases on approach to the saturated ferromagnetic (sFM) state (see circles in Fig. 5.1(a), (d)). The qualitative behavior is similar between $\alpha = 0.25$ and $\alpha = 0.4$. The positive sign of χ that is opposite to sign of the polarity (defined by magnetization of the central spin of the texture) reveals that the the ground states are antiskyrmions.

The existence of antiskyrmions in the DDE Hamiltonian is explicitly demonstrated via the spin configurations as well as skyrmion density maps in the ground state. We find that small values of α lead to sparse antiskyrmions within the zero field cooled (ZFC) protocol (see Fig. 5.1(b)), and the packing (size) of antiskyrmions increases (decreases) with increasing α (see Fig. 5.1(e)). The negative polarity is consistent with the fact that the central spin in the antiskyrmion texture is oriented opposite to the magnetization direction (see Fig. 5.1(c), (f)). In order to understand the origin and stability of sASk and pASk, we present results on an effective spin model derived from the DDE Hamiltonian.

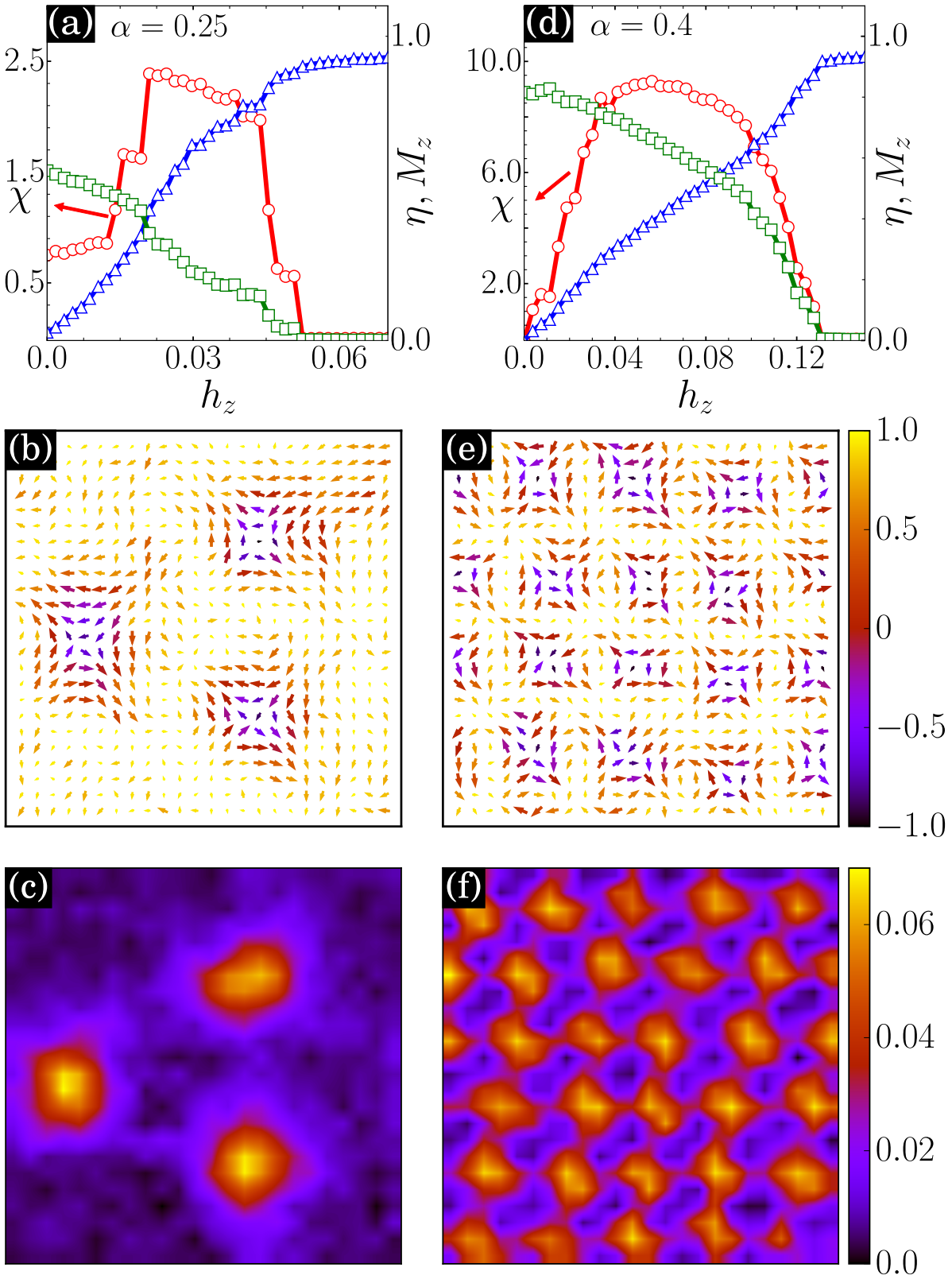

Figure 5.1 Magnetization M_z (triangles), total skyrmion density χ (circles) and vector chirality η (squares) as a function of applied Zeeman field for, (a) $\alpha = 0.25$, and (d) $\alpha = 0.4$. Snapshots of spin configurations, (b), (e), and the local skyrmion density, (c), (f), at $T = 0.01$ for representative values of α and h_z: (b)-(c) $\alpha = 0.25$, $h_z = 0.0298$; (e)-(f) $\alpha = 0.4$, $h_z = 0.06$.

5.3 Origin and stability of sparse and packed antiskyrmions

We derive an effective spin model for $H_{\rm DDE}$ in similar way as derived for $H_{\rm RDE}$ in Chapter 4, we obtain,

$$\begin{aligned} H_{\rm eff} &= -\sum_{\langle ij\rangle,\gamma} D_{ij}^{\gamma} f_{ij}^{\gamma} - h_z \sum_i S_i^z, \\ \sqrt{2} f_{ij}^{\gamma} &= \big[t^2(1+\mathbf{S}_i\cdot\mathbf{S}_j) + (-1)^{\hat{\gamma}} 2t\lambda\hat{\gamma}\cdot(\mathbf{S}_i\times\mathbf{S}_j) \\ &\quad +\lambda^2(1-\mathbf{S}_i\cdot\mathbf{S}_j + 2(\hat{\gamma}\cdot\mathbf{S}_i)(\hat{\gamma}\cdot\mathbf{S}_j))\big]^{1/2}, \\ D_{ij}^{\gamma} &= \langle [e^{ih_{ij}^{\gamma}} d_i^{\dagger} d_j + \text{H.}c.]\rangle_{gs}. \end{aligned} \tag{5.7}$$

In the above, $\hat{\gamma} = \hat{x}\cdot\hat{\gamma}$, f_{ij}^{γ} (h_{ij}^{γ}) is the modulus (argument) of complex number g_{ij}^{γ} and $\langle\hat{O}\rangle_{gs}$ denotes expectation values of operator $\hat{O}$ in the ground state. It has been shown that using a constant value of D_{ij}^{γ} captures the essential physics of the Hamiltonian Eq. (5.7), therefore we set $D_{ij}^{\gamma} \equiv D_0 = 1$ in our simulations.

We simulate $H_{\rm eff}$ using the conventional classical MC scheme as discussed in Section 2.7.1. Similar to the RDE model[33], we find classical spin liquid states with filamentary domain wall structure characterized by the diffuse ring pattern in the spin structure factor in the absence of external field for small α. These states can be viewed as the parent state for the exotic skyrmion- and antiskyrmion-like spin textures. Although the filamentary domain walls are randomly oriented in these states and look similar for Rashba and Dresselhaus systems. We differentiate between these two by plotting the corresponding relevant component of vector chirality maps for each respectively (see Fig. 5.2). Compare the vector chirality definitions Eq. (4.6) and Eq. (5.6) for each. The relevant components of $(\mathbf{S}_i\times\mathbf{S}_j)$ in each definitions are nothing but the components occur in $H_{\rm eff}$ derived for each model. Physically it means that unlike Rashba system in which along x-direction, a spiral in xz plane and along y-direction a spiral in yz plane is preferred; here in Dresselhaus metals a spiral in yz plane is preferred along x-direction and along y-direction a spiral in xz plane is preferred.

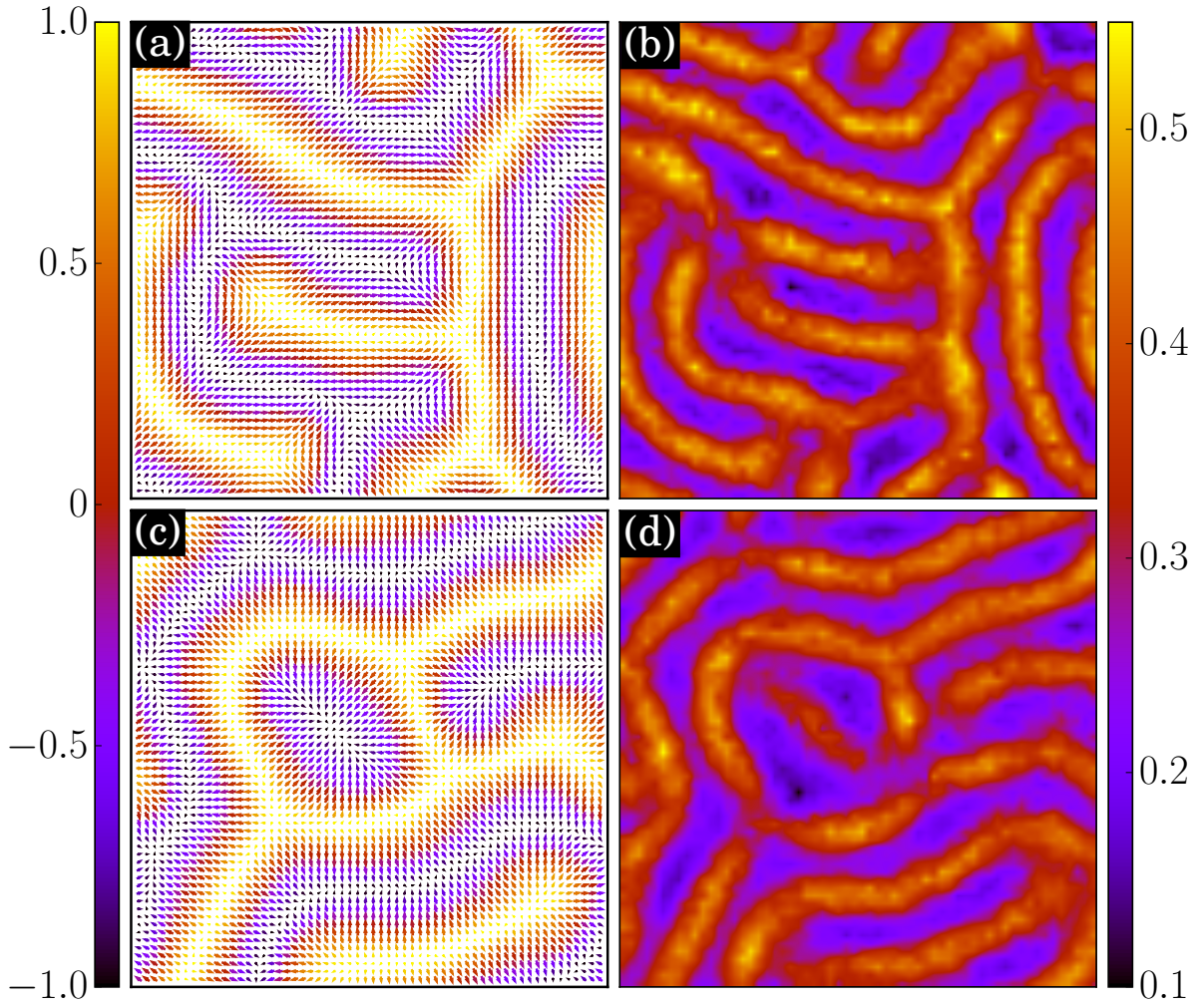

Figure 5.2 Snapshots of fDW states (left column) and corresponding vector chirality map (right column) taken from Monte Carlo simulationsa at $\alpha = 0.16$ and $h_z = 0.0$. (a)-(b) for H_{eff} from DDE model, (c)-(d) for H_{eff} from RDE model.

In Fig. 5.3 we show the field-dependence of magnetization, η and χ for H_{eff} which is very similar to that obtained via HMC (compare Fig. 5.1 (a), (d) and Fig. 5.3). For small values of α, magnetization increases linearly for small h_z, followed by a slower than linear rise. This change to non-linear behaviour is accompanied by a sharp increase in the magnitude of χ (see Fig. 5.3(a), (b)). A simple understanding is that the emergence of antiskyrmions arrests the ease with which spins align along the direction of the external magnetic field. A finite value of η in the absence of magnetic field originates from the DM-like terms present in the effective Hamiltonian. Variation of η is anticorrelated with that of magnetization and the former shows a sharp decrease accompanying the increase in magnitude of χ (see Fig. 5.3(a), (b)). Finally, for still larger values of applied field, system approaches sFM state, with both χ and η vanishing. For $\alpha = 0.5$, the change in χ near $h_z = 0.25$ is sharper, and is accompanied by a weak discontinuity

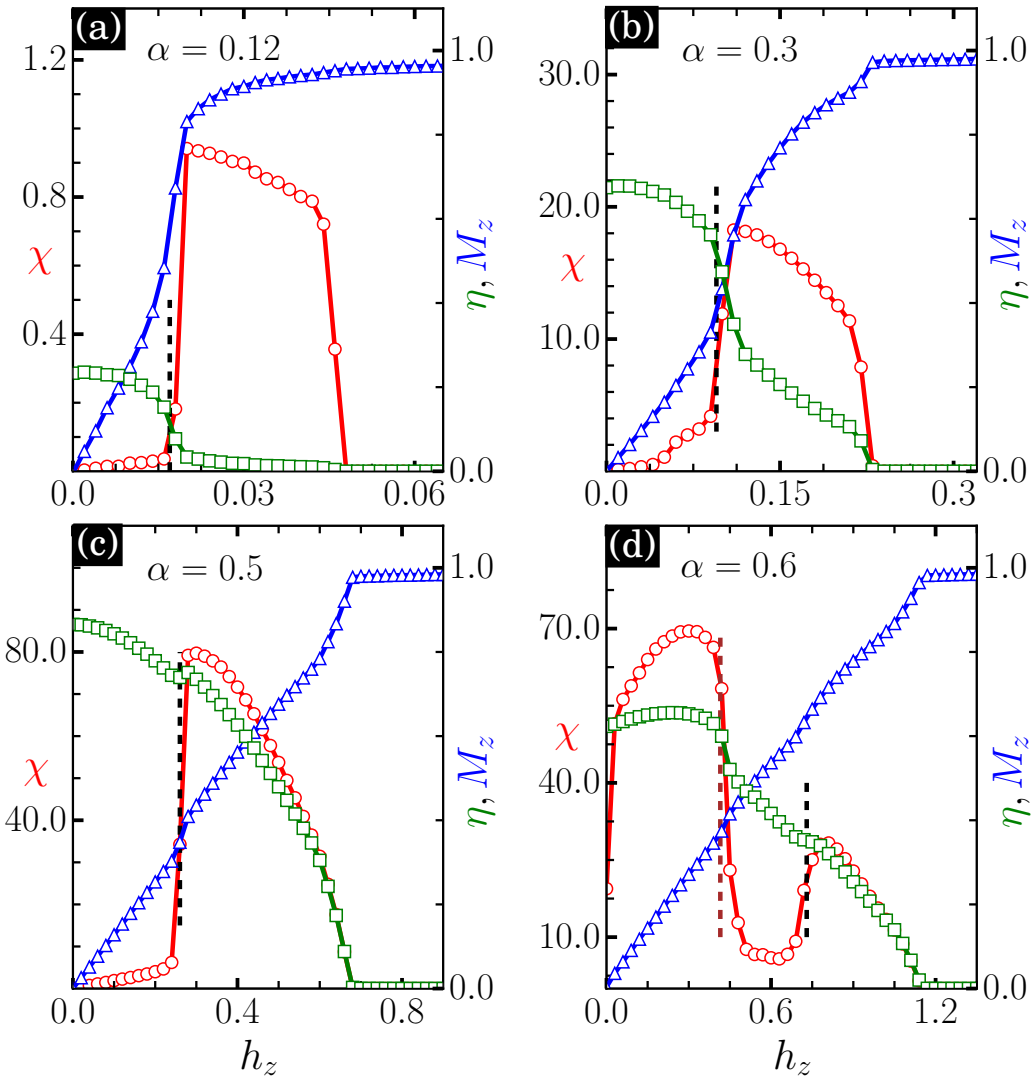

Figure 5.3 (a) - (d) Magnetization (triangles), total skyrmion density (circles) and vector chirality (squares) as a function of h_z for different values of α.

in both magnetization and η (see Fig. 5.3(c)). This qualitatively different behaviour is an indicator of the pASk state, as will be illustrated below with the help of real space spin configurations. For $\alpha = 0.6$, χ is finite even at $h_z = 0$. Interestingly, the magnitude of χ reduces with increasing h_z, and then again increases before finally vanishing on approach to the sFM state (see Fig. 5.3(d)). These results are consistent with our results reported for RDE model[34] which suggest that the phase diagram will look similar to Fig. 4.5.

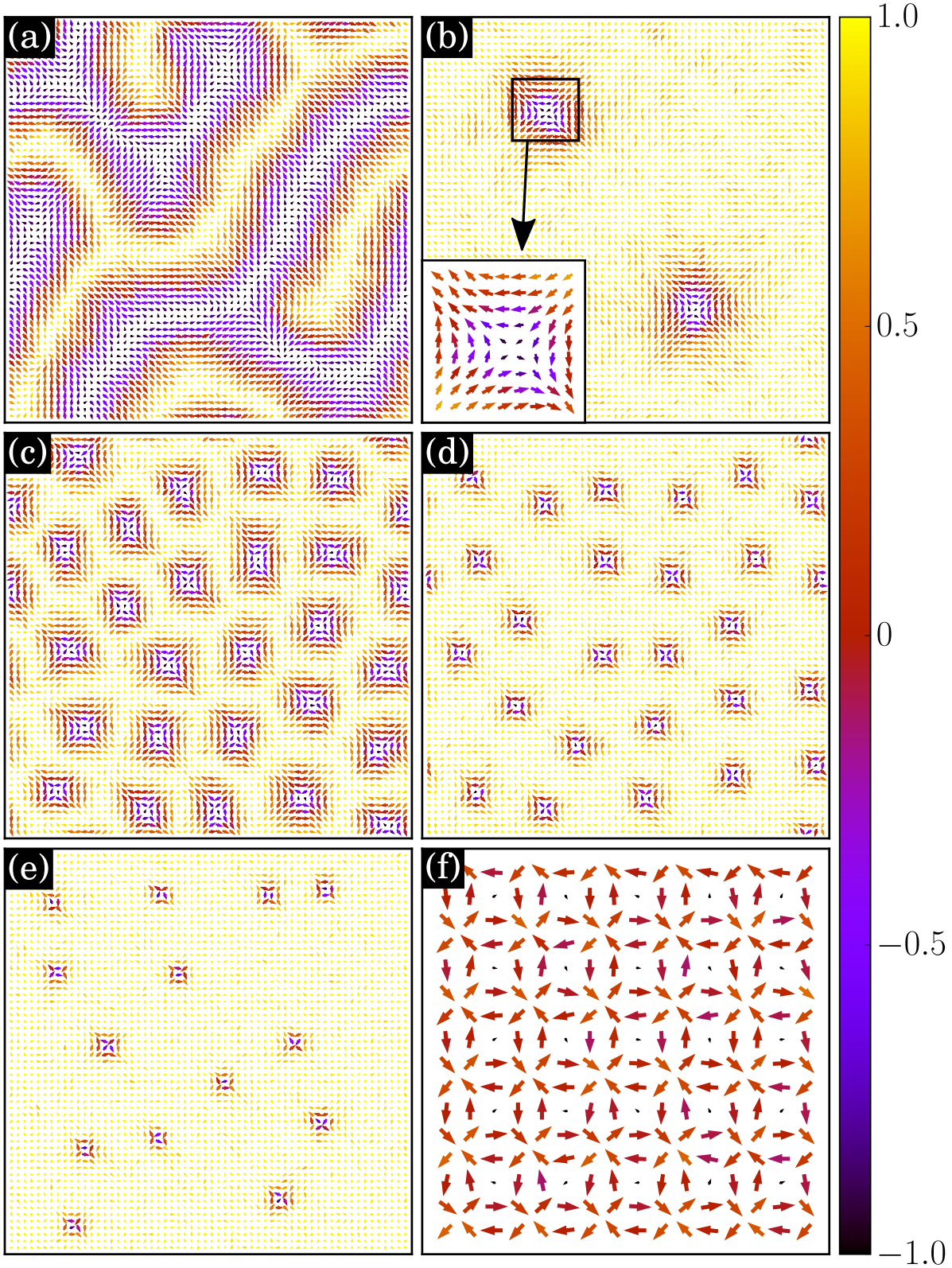

Figure 5.4 Low temperature snapshots of spin configurations for representative values of α and h_z. (a) fDW state at $\alpha = 0.15$, $h_z = 0$, (b) sparse antiskyrmions at $\alpha = 0.15$, $h_z = 0.036$, (c) pASk at $\alpha = 0.3$, $h_z = 0.11$, (d) ASk size reduction at $\alpha = 0.3$, $h_z = 0.18$, (e) number of ASk reduction at $\alpha = 0.3$, $h_z = 0.22$ and (f) ASkX at $\alpha = 0.6$, $h_z = 0.0$.

We show in Fig. 5.4 the evolution of magnetic textures with change in α and h_z within H_{eff}. We observe that within the ZFC protocol at finite temperatures, the domain junctions in the fDW states for small α (see Fig. 5.4(a)) become nucleation centers for antiskyrmions when magnetic field is applied (see Fig. 5.4(b)). For larger values of α, SQ spiral state gives way to the pASk phase (see Fig. 5.4(c)). For a given α, increasing h_z leads, initially, to a reduction of the size by polarizing the spins in the tail of skyrmions (compare Fig. 5.4 (c) and (d)) and then to a reduction of the number of skyrmions. (compare Fig. 5.4 (d) and (e)). A perfectly ordered crystal of smallest possible antiskyrmions on a square lattice is obtained in the absence of external field at $\alpha = 0.6$ (see Fig. 5.4 (f)). The pASk phase sits in proximity to the sASk phase and therefore, it can be viewed as a packed version of isolated skyrmions. This picture does not apply for the ASkX phase as upon increasing h_z, the phase is destabilized in favour of a SQ spiral state. Therefore, the key difference between pASk and ASkX is that in the pASk phase each antiskyrmion can be viewed as an individual entity, but the ASkX phase represents a truely cooperative order of spins. We have also confirmed that the skyrmion formation in the model is not an artifact of the ZFC protocol, by verifying their existence using the field cooled protocol.

5.4 Thermal stability of antiskyrmions

In this section we show the skyrmion density map in applied Zeeman field (h_z) vs temperature (T) plot for small Dresselhaus SOC regime. We find that at small but finite T the isolated antiskyrmions (finite skyrmion density) emerge in increating-T simulations starting with the sFM state (zero skyrmion density) at $T = 0.001$. A possible explanation for such an appearance of skyrmions is in terms of entropic contributions to free energy that become relevant only at finite temperatures. Therefore, while the sASk is not a stable ground state, it is still experimentally relevant as the isolated antiskyrmions appear as excitations in the sFM ground state at finite T. The number density of antiskyrmions and hence skyrmion density in this finite T phase depends on the values of T and h_z, in addition to α. At high enough temperature antiskyrmion state will have transition to paramagnetic state (zero skyrmion density).

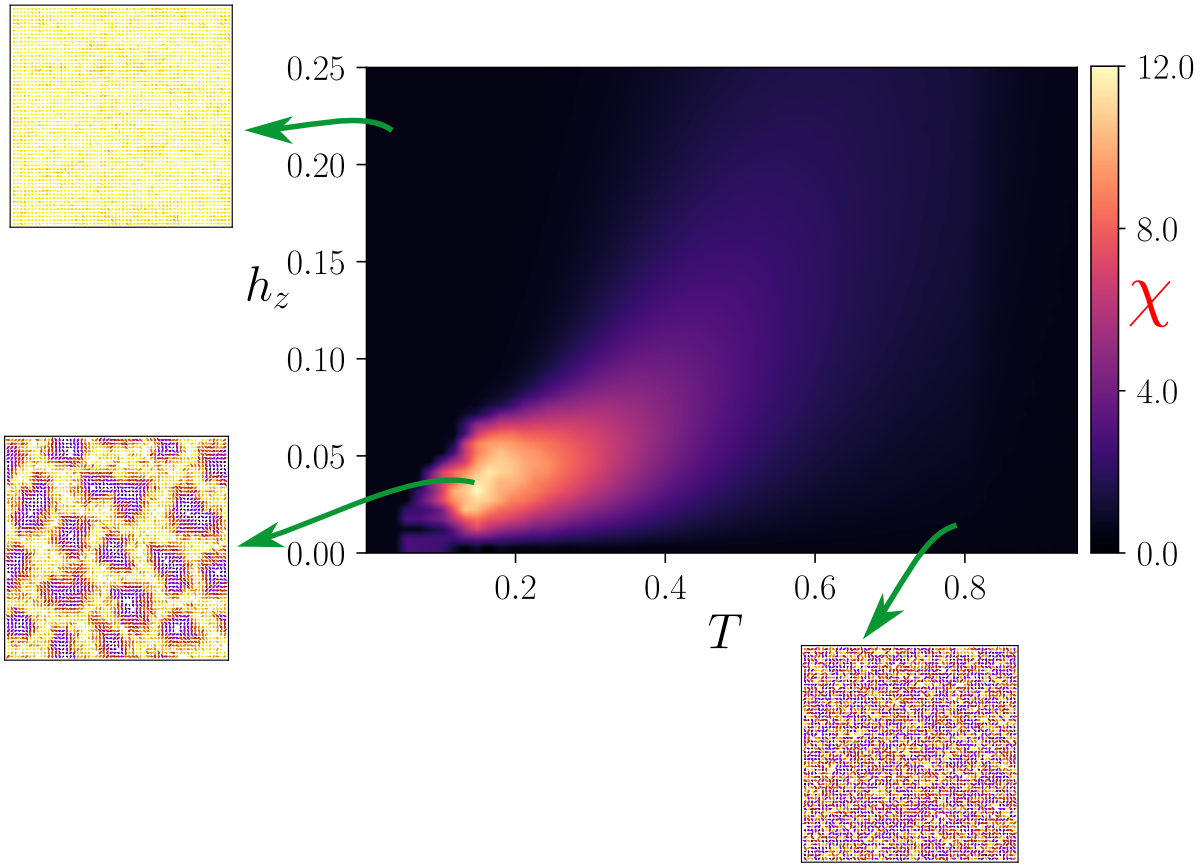

Figure 5.5 h_z - T plot with χ map at $\alpha = 0.2$. Various states like sFM, antiskyrmion state and paramagnet are found at various (h_z, T) regime.

5.5 Origin and stability of Bloch skyrmions

In effective spin model Eq. (5.7) if we modify f_{ij}^{γ} such that

$$\sqrt{2} f_{ij}^{\gamma} = \left[t^2 (1 + \mathbf{S}_i \cdot \mathbf{S}_j) + 2t\lambda \hat{\gamma} \cdot (\mathbf{S}_i \times \mathbf{S}_j) + \lambda^2 (1 - \mathbf{S}_i \cdot \mathbf{S}_j + 2(\hat{\gamma} \cdot \mathbf{S}_i)(\hat{\gamma} \cdot \mathbf{S}_j)) \right]^{1/2}, \quad (5.8)$$

which practically means that the sign of either t or λ along x direction is reversed relative to the y direction. We simulate the modified H_{eff} using the conventional classical MC and see the consequences. In Fig. 5.6 we show the evolution of magnetic textures with change in α and h_z within modified H_{eff}. We find that, the domain junctions in the fDW states for small α (see Fig. 5.6(a)) become nucleation centers for Bloch skyrmions when magnetic field is applied (see Fig. 5.6(b)). For larger values of α, packed Bloch skyrmions phase (see Fig. 5.6(c)) are stabilized as ground states. The triangular lattice of packed Skyrmions phase is obtained in the presence of external field, while at $\alpha = 0.6$ the square-lattice Bloch SkX is already present at $h_z = 0$ (see Fig. 5.6 (d)).

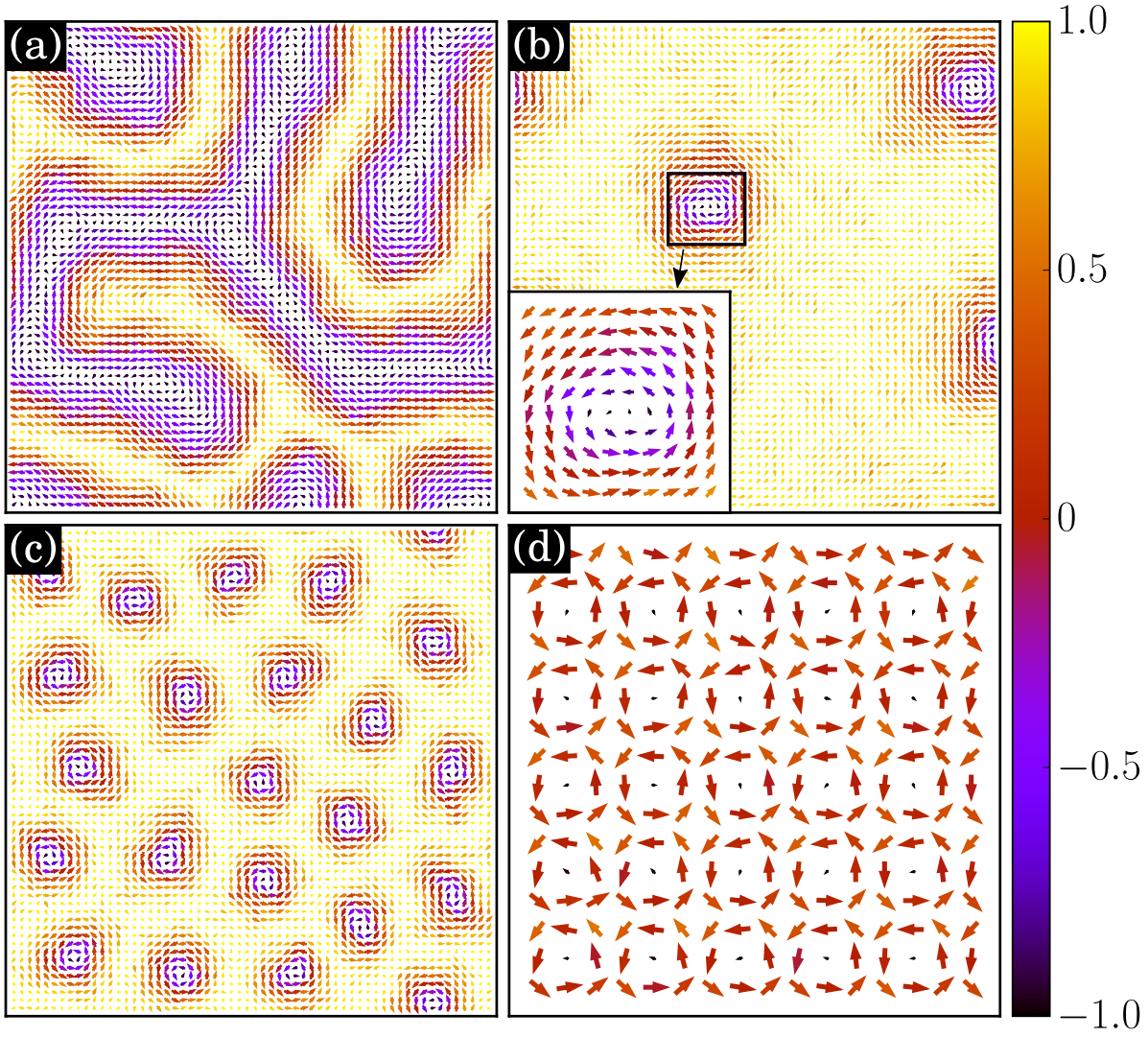

Figure 5.6 Low temperature snapshots of ground states in modified model for representative values of α and h_z. (a) fDW state at $\alpha = 0.16$, $h_z = 0$, (b) sparse Bloch skyrmions at $\alpha = 0.16$, $h_z = 0.036$, (c) packed Bloch skyrmions at $\alpha = 0.3$, $h_z = 0.12$ and (d) Bloch skyrmions crystal at $\alpha = 0.6$, $h_z = 0.0$.

5.6 Conclusion

We have explored the classic DE mechanism modified by Dresselhaus SOC in the presence of Zeeman field. An explicit demonstration of the existence of nanoscale antiskyrmions in an electronic model with no direct spin-spin interactions is presented. At small Dresselhaus SOC parameter the fDW states exist at low temperature, which are different from the fDW states found in Rashba metals[33]. As a consequence of that these fDW structures can be viewed as parent state for antiskyrmions unlike skyrmions in Rashba metals. While the pASk states are found to be true ground states of the model,

the sparse antiskyrmions are metastable in the ground state but occur at finite temperature as excitations of the ferromagnet in the presence of magnetic field. The reversal of sign of hopping parameter along x direction relative to the y direction leads to stabilization of Bloch skyrmion states. Similarly in RDE model, reversal of sign of hopping parameter along any direction will result in stabilization of antiskyrmions. We can design materials with appropriate electronic band structure that will host antiskyrmions in thin films. From these results we conclude that in addition to the type of spin orbit coupling (Rashba or Dresselhaus) the electron itineracy also plays very important role in deciding the type of skyrmion and the corresponding antiskyrmions textures in a metal.

Bibliography

[1] A. Fert, N. Reyren and V. Cros, *Nat. Rev. Mater.*, 2017, **2**, 17031.

[2] R. Wiesendanger, *Nature Reviews Materials*, 2016, **1**, 1–11.

[3] A. Fert, V. Cros and J. Sampaio, *Nat. Nanotechnol.*, 2013, **8**, 152–156.

[4] N. Nagaosa and Y. Tokura, *Nat. Nanotechnol.*, 2013, **8**, 899–911.

[5] A. N. Bogdanov and C. Panagopoulos, *Phys. Today*, 2020, **73**, 44–49.

[6] J. P. Chen, D.-W. Zhang and J. M. Liu, *Sci. Rep.*, 2016, **6**, 29126.

[7] U. K. Roessler, A. Bogdanov and C. Pfleiderer, *Nature*, 2006, **442**, 797–801.

[8] N. Mohanta, E. Dagotto and S. Okamoto, *Physical Review B*, 2019, **100**, 064429.

[9] J. Iwasaki, A. J. Beekman and N. Nagaosa, *Physical Review B*, 2014, **89**, 064412.

[10] S. D. Yi, S. Onoda, N. Nagaosa and J. H. Han, *Phys. Rev. B*, 2009, **80**, 054416.

[11] S. Hayami and Y. Motome, *Phys. Rev. Lett.*, 2018, **121**, 137202.

[12] S. Hayami and Y. Motome, *Phys. Rev. B*, 2019, **99**, 094420.

[13] Z. Wang, Y. Su, S.-Z. Lin and C. D. Batista, *Phys. Rev. Lett.*, 2020, **124**, 207201.

[14] A. V. Bezvershenko, A. K. Kolezhuk and B. A. Ivanov, *Phys. Rev. B*, 2018, **97**, 054408.

[15] M. Hoffmann, B. Zimmermann, G. P. Müller, D. Schürhoff, N. S. Kiselev, C. Melcher and S. Blügel, *Nature communications*, 2017, **8**, 1–9.

[16] S. Huang, C. Zhou, G. Chen, H. Shen, A. K. Schmid, K. Liu and Y. Wu, *Physical Review B*, 2017, **96**, 144412.

[17] L. Qiu, J. Xia, Y. Feng, L. Shen, F. J. Morvan, X. Zhang, X. Liu, L. Xie, Y. Zhou and G. Zhao, *Journal of Magnetism and Magnetic Materials*, 2020, **496**, 165922.

[18] W. Koshibae and N. Nagaosa, *Nature communications*, 2016, **7**, 1–8.

[19] X. Z. Yu, N. Kanazawa, Y. Onose, K. Kimoto, W. Z. Zhang, S. Ishiwata, Y. Matsui and Y. Tokura, *Nat. Mater.*, 2011, **10**, 106–109.

[20] S. Meyer, M. Perini, S. von Malottki, A. Kubetzka, R. Wiesendanger, K. von Bergmann and S. Heinze, *Nature communications*, 2019, **10**, 1–8.

[21] P.-J. Hsu, L. Rózsa, A. Finco, L. Schmidt, K. Palotás, E. Vedmedenko, L. Udvardi, L. Szunyogh, A. Kubetzka, K. von Bergmann *et al.*, *Nature communications*, 2018, **9**, 1–7.

[22] A. Tonomura, X. Yu, K. Yanagisawa, T. Matsuda, Y. Onose, N. Kanazawa, H. S. Park and Y. Tokura, *Nano Lett.*, 2012, **12**, 1673–1677.

[23] X. Yu, W. Koshibae, Y. Tokunaga, K. Shibata, Y. Taguchi, N. Nagaosa and Y. Tokura, *Nature*, 2018, **564**, 95–98.

[24] T. Nagase, M. Komatsu, Y. So, T. Ishida, H. Yoshida, Y. Kawaguchi, Y. Tanaka, K. Saitoh, N. Ikarashi, M. Kuwahara *et al.*, *Physical review letters*, 2019, **123**, 137203.

[25] N. Romming, C. Hanneken, M. Menzel, J. E. Bickel, B. Wolter, K. von Bergmann, A. Kubetzka and R. Wiesendanger, *Science*, 2013, **341**, 636–9.

[26] X. Yu, N. Kanazawa, W. Zhang, T. Nagai, T. Hara, K. Kimoto, Y. Matsui, Y. Onose and Y. Tokura, *Nature communications*, 2012, **3**, 1–6.

[27] X. Zhao, C. Jin, C. Wang, H. Du, J. Zang, M. Tian, R. Che and Y. Zhang, *Proc. Natl. Acad. Sci. U. S. A.*, 2016, **113**, 4918–23.

[28] A. K. Nayak, V. Kumar, T. Ma, P. Werner, E. Pippel, R. Sahoo, F. Damay, U. K. Rößler, C. Felser and S. S. P. Parkin, *Nature*, 2017, **548**, 561–566.

[29] P. Vir, N. Kumar, H. Borrmann, B. Jamijansuren, G. Kreiner, C. Shekhar and C. Felser, *Chemistry of Materials*, 2019, **31**, 5876–5880.

[30] J. Jena, R. Stinshoff, R. Saha, A. K. Srivastava, T. Ma, H. Deniz, P. Werner, C. Felser and S. S. P. Parkin, *Nano Letters*, 2020, **20**, 59–65.

[31] L. Camosi, N. Rougemaille, O. Fruchart, J. Vogel and S. Rohart, *Physical Review B*, 2018, **97**, 134404.

[32] M. Potkina, I. Lobanov, O. Tretiakov, H. Jónsson and V. Uzdin, *Physical Review B*, 2020, **102**, 134430.

[33] D. S. Kathyat, A. Mukherjee and S. Kumar, *Phys. Rev. B*, 2020, **102**, 075106.

[34] D. S. Kathyat, A. Mukherjee and S. Kumar, *Phys. Rev. B*, 2021, **103**, 035111.

6

Summary and Outlook

A brief summary of the work done in this thesis is presented.

This thesis presents a microscopic description of exotic magnetic states observed in thin films of a broad class of metallic magnets. Magnetic skyrmions are topological textures in magnetization that are envisioned as the building blocks of next-generation data storage and processing devices. The capacity of information storage of such devices is controlled by the density, and hence the size, of skyrmions. Therefore, new ideas for stabilizing nanoscale skyrmions are of immense research interest. More importantly, the current understanding of skyrmions in metals is highly inadequate as it relies on generalized Heisenberg models that are derived for Mott insulators. This is a serious conceptual flaw as no clear argument exists in the literature for ignoring electron itinerancy in metallic magnets. This thesis presents a significant advance on both these fronts.

In **chapter 2** We start with Rashba-Dresselhaus spin-orbit coupled ferromagnetic Kondo lattice model, which is relevant for metallic systems. We study the model in double exchange limit and from double exchange model we derive microscopic spin only Hamiltonian. In particular, the model is applicable to thin films of MnSi-type B20 metals and multilayers of transition metals and their alloys. In this model, Dzyaloshinskii-Moriya and Kitaev-type anisotropic interactions emerge naturally, in addition to the standard Heisenberg term. We studied Rashba and Dresselhaus systems separately in following chapters.

In **chapter 3** we explicitly test the validity of the effective spin model by comparing results against those obtained for the exact electronic model. We then map out the phase diagram of the effective spin model using large scale Monte Carlo simulations. The phase diagram consists of (i) planar spiral states, (ii) non-coplanar skyrmion crystal states, (iii) diagonally oriented planar flux state, and (iv) a classical spin liquid metallic state with filamentary domain wall structure characterized by the diffuse ring pattern in the spin structure factor. These filamentary structures display a remarkable similarity with the experimental observations on thin films of transition metals and B20 metals, and this state can be viewed as the parent state for the exotic skyrmion states. We identify the origin of this exotic filamentary state in an unusual ground state degeneracy present in the model because of the spiral states with competing orientations of the spiral planes. The model can be tuned across these states by varying the strength of Rashba coupling.

In **chapter 4** we show that the classic double exchange mechanism modified by Rashba spin-orbit coupling in the presence of Zeeman field provides all the necessary ingredients to stabilize Neel skyrmions with tunable size and density of skyrmions. The results are numerically exact as they are based on quantum mechanical hybrid Monte

Carlo simulations. An effective spin Hamiltonian is studied for a comprehensive understanding of the origin as well as stability of these spin textures. A filamentary domain wall (fDW) phase is identified as the parent of sparse skyrmions (sSk), which are found to be stable only at finite temperatures and metastable in the ground state, and a single-Q (SQ) spiral state leads to packed skyrmions (pSk). The similarity of our simulation results with, (i) circular pattern in the small angle neutron scattering (SANS) experiments, and (ii) filamentary textures in Lorentz transmission electron microscopy (LTEM) images on thin films of Co-Zn-Mn alloys, FeGe, MnSi and PdFe/Ir bilayer, makes us believe that the mechanism is not merely a theoretical construct but exists in real materials. The DM interaction based theories present a diagonal spin spiral with ordering wavevector (Q, Q) as the parent of skyrmion states. These theories do not explain the two key experimental features mentioned above. Our results, on the other hand, show that the skyrmion states emerge either from filamentary domain walls or from collinear (0, Q)/(Q, 0) spirals. The isolated skyrmions also appear as excitations in the saturated ferromagnet ground state at finite T. The Bott index is shown to be finite in skyrmion states; hence we characterize these phases as disordered topological metals. Topological Hall conductivity is shown to correlate with the Bott index. Local density of states are shown to possess oscillations near the band edges – characteristic of quantum confinement effects. These features are completely beyond the scope of existing phenomenological theories and provide a clear test for the presence or absence of the proposed mechanism in real materials.

In **chapter 5** we study double exchange model modified by Dresselhaus SOC. The form of the Hamiltonian is similar to that obtained for the Rashba double exchange model. With the help of the effective spin model, we find that unlike Rashba system in which along x-direction, a spiral in xz plane and along y-direction a spiral in yz plane is preferred; here in Dresselhaus metals a spiral in yz plane is preferred along the x-direction and along y-direction a spiral in xz plane is preferred. As a result of that the antiskyrmion phases emerge as ground states in this model in the presence of Zeeman field. We map out the Zeeman field vs temperature phase diagram to understand thermal stability of the states. The reversal of sign of hopping parameter along x direction relative to the y direction results in stabilization of Bloch skyrmion states. We summarize the results in form of a table below which shows that the spin texture stabilized in the SOC modified double exchange models depends on the type of spin-orbit coupling (Rashba or Dresselhaus) and the sign of the hopping parameters.

Table: Spin Texture dependence on type of SOC and sign of hopping parameters			
SOC	hopping along x (t_x)	hopping along y (t_y)	spin texture
Rashba	$+ve$	$+ve$	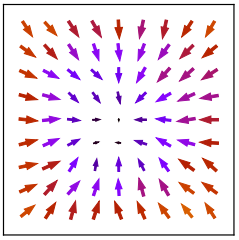
Rashba	$-ve$	$+ve$	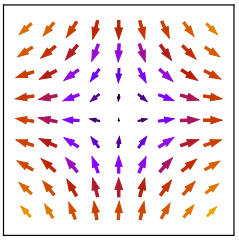
Dresselhaus	$+ve$	$+ve$	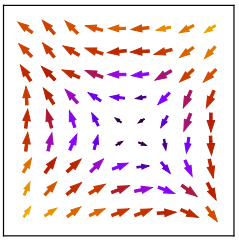
Dresselhaus	$-ve$	$+ve$